



Title	Control of Nanoparticle Self-Assembly in Water by Rational Surface Design
Author(s)	飯田, 良
Citation	北海道大学. 博士(理学) 甲第13230号
Issue Date	2018-03-22
DOI	10.14943/doctoral.k13230
Doc URL	http://hdl.handle.net/2115/69928
Type	theses (doctoral)
File Information	Ryo_lida.pdf



[Instructions for use](#)

**Control of Nanoparticle Self-Assembly in Water
by Rational Surface Design**

Ryo Iida

Doctor of Science

Graduate School of Chemical Sciences and Engineering,
Hokkaido University

2018

Contents

Chapter 1 General Introduction

1-1. Nanoparticles in nanotechnology	2
1-1-1. Functions of inorganic nanoparticles	2
1-1-2. Gold nanoparticles	4
1-2. Assembly of nanoparticles	7
1-2-1. Assembly in chemistry	7
1-2-2. Nanoparticle assembly and functions	7
1-3. Self-assembly in biomolecules	11
1-4. Objective	13
1-5. References	16

Chapter 2 Synthesis of Janus-like Gold Nanospheres with Hydrophilic/Hydrophobic Faces by Surface Ligand exchange and their Self-Assemblies in water

2-1. Introduction	29
2-2. Experimental section	32
2-2-1. General information	32
2-2-2. Thiolate ligand synthesis	33
2-2-3. One-step or two-step ligand exchange reactions	43
2-2-4. Preparation of Janus GNSs with hydrophilic/hydrophobic faces	44
2-2-5. MALDI-TOF MS analysis of ligand-displaying GNSs	45
2-2-6. PCXSS experimental setup and analysis	45
2-3. Results and Discussion	47
2-3-1. Phase segregation of two ligands with different alkyl chains	47
2-3-2. Synthesis of Janus GNSs with hydrophilic/hydrophobic faces	56
2-3-3. Differences in self-assembly behavior in water between Domain and Janus-like GNSs	59
2-4. Conclusion	63
2-5. References	64

Chapter 3 Thermoresponsive Gold Nanospheres Covered with Oligo(Ethylene Glycol) Derivatives with an Alkyl Head

3-1. Introduction	71
3-2. Experimental section	75
3-2-1. General information	75
3-2-2. Thiol ligand synthesis	75
3-2-3. Surface modification of GNSs	88
3-2-4. Synthesis of 3-nm GNSs coated with C2 ligand	89
3-2-5. Characterization	90
3-3. Results and Discussion	92
3-3-1. Clouding points of free ligand molecules	92
3-3-2. Thermoresponsive assembly of 5-nm GNSs	94
3-3-3. Effects of the Alkyl heads	100
3-3-4. Effects of GNS size	102
3-3-5. Effect of alkyl tail length	106
3-4. Conclusion	108
3-5. References	109

Chapter 4 Two-step Assembly of Thermoresponsive Gold Nanorods Coated with a Single Kind of Ligand

4-1. Introduction	117
4-2. Experimental section	120
4-2-1. Materials	120
4-2-2. The synthesis and characterization of GNRs coated with CTAB	120
4-2-3. Surface modification of GNRs	124
4-2-4. Characterization	126
4-3. Results and discussion	129
4-3-1. Preparation of the thermoresponsive GNRs coated with thiolate ligands ..	129
4-3-2. Two-step assembly upon heating	132
4-3-3. Reversibility of the two-step assembly on thermal cycling	137
4-3-4. Examination of assembly mechanism by time course experiments	139
4-3-5. Factors determining assembly temperature	142
4-4. Conclusion	149
4-5. References	150

Chapter 5 Conclusion	155
Acknowledgement	158

Chapter 1

General Introduction

1-1. Nanoparticles in nanotechnology

Nanotechnology refers to a technology that controls substances from a few nanometers to less than 100 nanometers.¹ The term "nanotechnology" was proposed by Norio Taniguchi in 1974. Since President Bill Clinton declared National Nanotechnology Initiative in 2001, the big budget was invested for nanotechnology. As the improvement of electronic device performances by miniaturization is required, nanotechnology have rapidly advanced. The representative example is the increase of the density of transistors integrated in an IC chip. Lithography techniques is widely used for the fabrication of precise nanopatterns on a substrate for electronic devices, leading the advance of fine processing technology. However, the attractiveness of nanoscale materials is not only small. Another reason for the rapid advance of nanotechnology is that the physical and chemical properties different from those of bulk are exhibited when the size of metals, semiconductors, and metal oxides becomes nanoscale.² While the precise nanostructures are fabricated on a 2D substrate using lithography techniques, nanoscale particles, nanoparticles, can be utilized as a solution or a powder. Therefore, nanoparticle is the important material in nanotechnology, and attention is paid in a wide field, such as chemical, material, physical, and biological science.

1-1-1. Functions of inorganic nanoparticles

Metal, semiconductor and metal oxide nanoparticles show the novel optical, catalytic, magnetic functions (Figure 1-1). For example, localized surface plasmon resonance (LSPR) is optical property of metal nanoparticles, such as gold, silver, copper and platinum.³ LSPR is a phenomenon that the free electrons of the metal nanoparticles undergo an oscillation in the presence of the oscillating electromagnetic field of the light,

enhancing the electromagnetic field at the nanoparticle surface.² Electromagnetic field enhanced by LSPR provides the enhancement of the Raman scattered light of molecules near the metal nanoparticle, called a surface-enhanced Raman scattering (SERS), and it is used for applications to high sensitive sensing.^{4,5} Nanoparticles of 1 to 10 nm composed of hundreds to thousands of semiconductor atoms are called quantum dots. The energy level at the quantum dot changes to a discrete state as the number of constituent atoms decreases. Therefore, the effective band gap energy increases with the band width of the conductor and the valence electron depending on the decrease of the number of constituent atoms. As the result, quantum dots emit strong fluorescence. Quantum dots are used for bioimaging because their robustness against photobleaching enable to long fluorescence observation.⁶ Additionally, gold nanoparticles show highly active catalysts for CO oxidation⁷ and NO reduction⁸ although gold is chemically inert in the bulk state. The nanoparticles of ferromagnetic metal or metal oxide (Fe, Co, Fe₃O₄ and so on) show superparamagnetism,⁹ which are used as magnetic recording materials such as hard disks of personal computers and magnetic tapes. The inorganic nanoparticles play important roles in our lives and academic researches.



Figure 1-1. Variety of nanoparticles. (a) gold nanoparticles, (b) quantum dots,¹⁰ and (c) iron oxide nanoparticles.¹¹

1-1-2. Gold nanoparticles

- History

Gold nanoparticles are one of the most ancient nanomaterials of investigation. Historically, colloidal golds were made around the 5th or 4th century B.C. in Egypt and China, which were used to make ruby glass, such as Lycurgus cup because of their ruby color.¹² In the Middle ages, colloidal gold was used as coloring materials for stained glass. In 17th century, Cassius made colloidal gold using HAuCl_4 and $\text{Sn}(\text{OH})_2$, which were called “purple of Cassius”, but at that time it was thought to be a compound of gold and tin. It was Michael Faraday (1791-1867) who initially claimed that gold exists as a colloid in the ruby solution. Faraday prepared gold colloids through reduction of Au ion by phosphorus, declaring that gold was present in the liquid as “finely divided” state by using Faraday-Tyndall phenomenon.¹³ It is noted that the term "colloid" was proposed by Graham in 1861.¹⁴ In 1908, Mie showed that the ruby color arose from the absorption and scattering of light by gold nanosphere.^{15,16} In the 20th century, an electron microscope and a scanning probe microscope are invented, and research on nanoparticles including gold has accelerated. Today, GNPs have been widely used for fundamental researches and practical applications as they can easily control their shape and surface property.

- Size and shape control of gold nanoparticles

The shape and size are directly influence to the optical and physical properties. Basically, spherical GNPs (GNSs) were synthesized by the reduction of Au ion (HAuCl_4) in the presence of capping reagent. As the plasmon absorption is strongly dependent on the size of a GNS, the precise and convenient size control method is necessary.¹² The GNS size is determined by the reduction rate and the type of capping reagents. The

versatile synthetic method of GNSs using citrate as reduction agent of HAuCl_4 in water was reported by Turkevich (referred to as Turkevich method) at 1951, which produces almost spherical particles over a tunable range of sizes.¹⁷ This method has been improved by many groups,^{18–20} including Frens.²¹ The representative synthesis in organic solvent was reported by Brust and Schiffrin, which referred to as Brust-Schiffrin method.²² Using two-phase (water-toluene) reduction of AuCl_4^- by NaBH_4 in the presence of an alkanethiol, dispersions of 1-3 nm GNSs coated with thiol have been prepared.

The wavelength of light absorbed by LSPR of a GNP is dependent not only size but also its shape. The morphology of GNPs is easily controlled *via* a seed growth method,^{23,24} and anisotropic GNPs with various shapes (nanorod,²⁵ nanocube,²⁶ triangular nanoplate,^{27–29} and so on) were synthesized. The seed growth method includes the two steps; the seed-synthesis step and growth step. In the first step, the small “seed” GNPs were synthesized by strong reagent, such as NaBH_4 . In the second step, the seeds are added to a “growth” solution containing HAuCl_4 , the stabilizing and reducing agents, then the newly reduced Au^0 grows on the seed surface to form large-size GNPs. The shape of the gold nanoparticles depends on the growth rate and selective surface passivation in growth step.³⁰ Among the various anisotropic-shaped GNPs, gold nanorods (GNRs) have attracted much attention due to two modes of LSPR corresponding to a transverse and longitudinal LSPR.³¹ GNRs are also synthesized via the seed growth method,^{32,33} and the peak of longitudinal LSPR mode of GNRs can be tuned in the visible-near infrared region by controlling the aspect ratio.³⁴ Therefore, controllability of size and shape of gold nanoparticles is high

- Surface modification

To control the function of a GNP, the surface modification also plays an important role. The dispersibility in solvent is determined by chemical property of ligand molecules on a GNP surface. The interparticle interaction is also controlled by surface modification. For modification of GNPs, molecular assembly technique is used. Molecules with functional groups strongly binding with gold form the monolayer on the GNP surface, which is called self-assembled monolayers (SAMs).³⁵ Formation of SAM is also used for surface modification of metal nanoparticles other than GNPs. The most used functional group for GNP modification is a thiol group (-SH). SAMs of thiolate molecules on GNP surface are formed via a ligand exchange reaction; i.e. existing ligands are displaced by different incoming ligands.³⁶ Ligands bound to a GNP surface with weaker interaction, such as citrate, is easily displaced by thiolate molecules bound with stronger Au-S bond. While the binding energy of Au-O_{COOH} is ~2 kcal/mol,³⁷ the Au-S bond is robust and its binding energy is ~40 kJ/mol.³⁸ By modification using ω -functionalized thiols, cationic,^{39,40} hydrophobic,²² hydrophilic,⁴¹ and fluorinated⁴² GNPs were synthesized. Additionally, since the drugs also can be loaded via gold-sulfate bond or electrostatic interaction on the surface, GNPs were used for drug carrier.⁴³⁻⁴⁵ Therefore, the design of ligand molecules is important to control the GNP property as well as their shape and size.

1-2. Assembly of nanoparticles

1-2-1. Assembly in chemistry

Assembly of disordered components into ordered structures, specific shape and/or patterns provides functions. Assemblies are occurred by physical, chemical, and social interactions, which leads to “emergence”. The most ingenious chemical assembly is achieved by life. The countless assemblies of individual molecules (lipids, amino acids, nucleic acids, sugars and so on) emerge the complex and dynamic functions of life. According to one theory, one of the first assembly events in the origin of life four billion years ago was the formation of a primitive vesicle composed by amphiphilic molecules. While biomaterials were constructed based on organic materials, artificially-programmed assembly which can also utilize the inorganic materials and semiconductors enables to create novel functional materials, such as metamaterials. Therefore, the control of assembly of chemical components is crucial to create new materials which have functions beyond natural ones to build a sustainable society.⁴⁶

1-2-2. Nanoparticle assembly and functions

As nanoparticles display properties that differ from those of the bulk state, assemblies of inorganic nanoparticles can emerge collective functions that are different to those displayed by individual nanoparticles and bulk states. Attractively, assemblies of nanoparticles can emerge collective functions that are different to those displayed by individual nanoparticles and the bulk state. Assembly process in which components automatically organize into patterns or structures without human intervention is called “self-assembly”.⁴⁷ Self-assembly, as a typical bottom-up system, is a powerful technique for the fabrication of 1D, 2D , and 3D nanostructures (Figure 1-2). While a top-down

approach including photolithography and electron-beam lithography is widely used for the fabrication of precise nanopatterns on substrate for electronic devices, self-assembly is suitable for construct the 3D nanostructures, especially in solution. Self-assembly of nanoparticles into large structures has attracted much attention due to their strong and specific interactions with light and magnetic fields,⁴⁸ opening the possibility for a wide range of applications in the field from material science and biology. For example, plasmon oscillations on adjacent metal nanoparticles can couple via their near-field interaction in assembly of nanoparticles.⁴⁹ The function of a nanoparticle assembly is determined by the assembled structure. For past several decades, it has been investigated the assembly of nanoparticles, and assembled structures such as linear,^{50–52} vesicles,^{53–59} and superlattice structures^{60–65} were reported, and they are applied for drug delivery carriers,^{66,67} electrodes,⁶⁸ sensors.^{69–73}

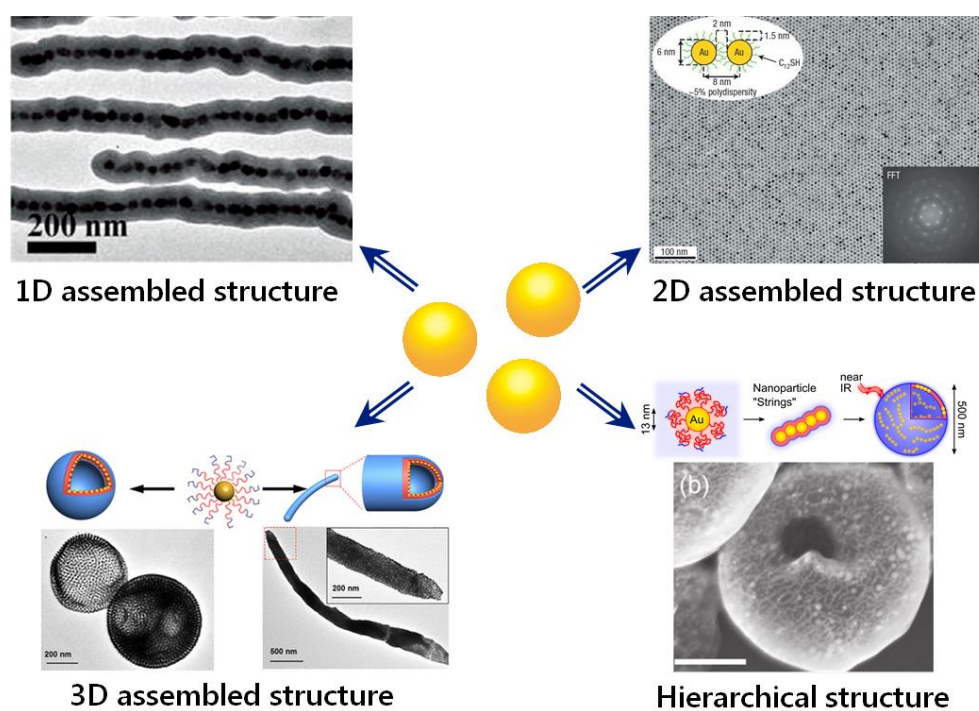


Figure 1-2. Self-assembly of nanoparticles into 1D,⁵² 2D,⁷⁴ 3D⁵³ and hierarchical structures⁷⁵

To control the assembled structures, assembly of nanoparticles require anisotropic interactions, which are provided to nanoparticles by surface modification or morphologic control. For instance, nanoparticles on which surface has two distinct chemical properties (Janus nanoparticles⁷⁶) have shown micelle-like assembly.⁷⁷ Non-spherical nanoparticles (nanorods, nanocubes, nanoplates, and so on) are assembled by direction-dependent interactions, such as a depletion force or van der Waals force, and form the specific assembled structure.⁷⁸ For example, Mirkin *et al.* have reported the columnar superlattices of gold nanoprisms by a depletion force under excess amounts of free surfactant.⁷⁹ Furthermore, anisotropic-shaped nanoparticles with site-specific modification have been developed.⁸⁰⁻⁸² Kumacheva *et al.* synthesized GNRs coated with CTAB along their long face and with polystyrene at the edge, forming rings, chains, and capsule structures as assemblies depending on the solvent.^{83,84} Therefore, for the construction of the desired structure of nanoparticle assemblies, the control of interparticle interactions is indispensable.

Additionally, control of assembled and dispersed state in response to environmental changes induces the dynamic changes of the optical and magnetic properties. To induce stimuli-responsive assembly/disassembly, nanoparticles are modified with stimuli-responsive ligands. For example, Klajn *et al.* reported the photo-responsive GNPs coated with azobenzene derivatives. Similar strategy are apply other nanoparticles in the response to various stimuli, such as temperature,⁸⁵⁻⁹⁰ pH,⁹¹⁻⁹³ and light.^{94,95} Stimulus responsive assemblies advance with applications spanning nanomedicine, renewable energy, biology, and even information technology.

Recently, the fabrication of hierarchical structures has been one of the hottest subjects in material sciences due to their potential functionalities.⁹⁶⁻¹⁰⁰ To date, however,

only a few hierarchical structures fabricated in solution have been reported.^{75,101} These hierarchical assemblies were made by varying the polarity of the solvent. However, the reversibility of the multi-step assembly process has not been exploited sufficiently. For the fabrication of sophisticated assemblies with dynamic structural changes, hierarchical structures composed of nanoparticles require controllable reversibility of assembly/disassembly in response to changes in the environment.

1-3. Self-assembly in biomolecules

The assemblies in natural products have been sophisticated over a long time. The representative biomaterial with elaborate structure and complex functions is protein. Proteins are composed of sequential amino acids as a fundamental unit (a primary structure), and construct hierarchical structures through multi-step folding processes. The primary structure determines the higher order structure of the protein. Secondary and tertiary structures are automatically formed *via* folding of a polypeptide through intramolecular interactions. Tertiary structures have heterogeneous surface and anisotropic shape, and some of these subsequently form quaternary structures and higher order hierarchical structures *via* intermolecular assemblies. Additionally, the assembly and disassembly of the tertiary structures to form the quaternary structure occur reversibly in response to environmental changes that induce dynamic functions. For example, actin, which is abundant protein expressed in eukaryotic cells, forms actin filament by polymerization (Figure 1-3). The interactions for protein folding include hydrogen bond, electrostatic interaction, and hydrophobic interaction. Here, when focusing on the hydrophobicity of amino acids, the tertiary structure has a heterogeneous surface pattern and disk-like shape. Actin filaments form cytoskeleton, and they play important roles in cellular adhesion, division, and motility. Actin regulates the movement of cells through binding and dissociation of the tertiary structures, caused by reversible change of in ATP and ADP actin state.¹⁰² The control of assembly/disassembly in response to the environment emerges the dynamic system.

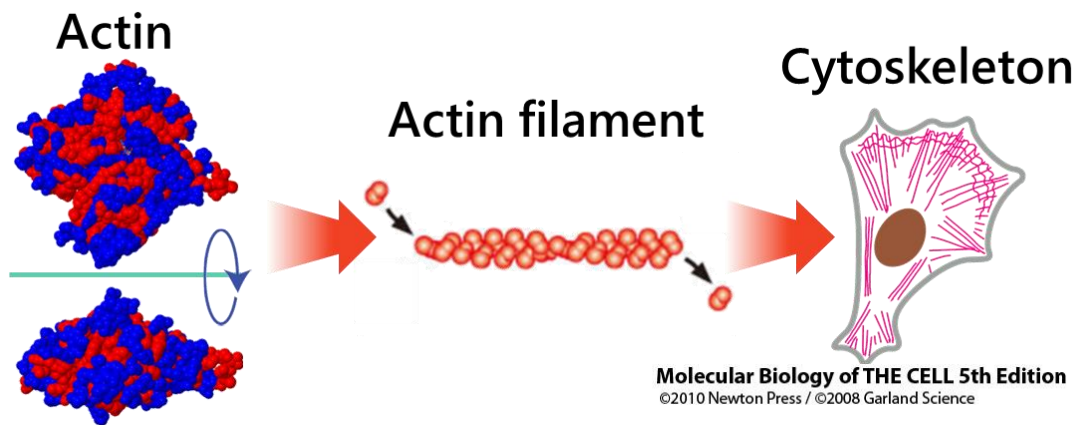


Figure 1-3. The tertiary structure of actin, actin filament, and cytoskeleton. The red and blue balls in the tertiary structure are hydrophobic and hydrophilic amino acids, respectively.

1-4. Objective

Metal nanoparticles have optical, magnetic and chemical functions different from the bulk state. In addition, the assemblies of metal nanoparticles display functions different from both the bulk state and the individual particles. As the function of the metal nanoparticle assembly strongly depends on its structure, structural control is important. Recently, attention has been drawn to the fabrication of hierarchical structures. However, there are few report examples of hierarchical structure, and its dynamic structure control has not been adequately studied. As control of dynamic and spatially controlled interparticle interactions is required for the self-assembly into desired structures in the response to environment, surface design by modification using ligand molecules is important. Furthermore, the control of the assembled and dispersed state in the response to environmental change provides dynamic function. On the other hand, proteins construct hierarchical structures with dynamic functions through multi-step folding processes. Their structures are determined from the heterogeneous surface patterns and shape. Thus, in this study, I focused on gold nanoparticles as core metal nanoparticles for building blocks since they are easy to control their shape, including the size, and the surface property. I aimed to control the assembled structures, leading the hierarchical structures, and induce the dynamic self-assembly via surface design (Figure 1-4).

In Chapter 2, I aimed to control the distribution of the two kinds of ligands. The control of ligand distribution is important to induce the anisotropic interactions. To control the distribution of the two kinds of ligands, I focused on the phase segregation of two kinds of ligand driven by hydrophobic interaction. I synthesized a series of thiolate ligands with alkyl chains of different lengths and investigated the effects on phase segregation on the GNPs. Especially, Janus nanoparticles with two different surface

properties on a single sphere, providing hydrophilic and hydrophobic characteristics, have been demonstrated to provide various types of 3D nanoparticle assemblies inspired by amphiphilic biomolecules, including lipids and some proteins. I investigated the difference of the assembly behavior of Janus nanoparticles and domain-formed nanoparticles in which the two ligands formed partial domains on the surface.

In Chapter 3, I show the reversible thermoresponsive assembly of the GNSs. The temperature is one of the simplest stimuli, which can be changed easily, gradually, and reversibly. Previously, the thermoresponsive nanoparticles were fabricated by the modification of polymer, such as pNIPAM. However, as polymers (>1000 g/mol) grafted on nanoparticles form the thick ligand shell, the nanoparticle shape effects to the assembled structures and assembly behavior is small. Therefore, inspired from nonionic surfactants showing a cloud point, I synthesized new series of ligands with low molecular weight (~ 500 g/mol) ($\text{HS}-(\text{CH}_2)_x-(\text{OCH}_2\text{CH}_2)_6-\text{OR}$, $x = 11$ and 3 , **R**; alkyl group). I investigate the assembly behavior and the factors influencing the assembly temperature of GNSs.

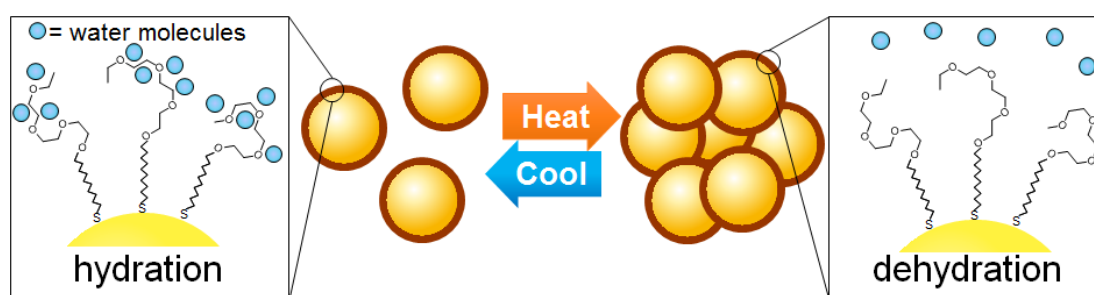
In Chapter 4, to induce the multi-step assembly into hierarchical structures, I focused on the difference of curvature of anisotropic nanoparticles. I found that the temperature at which assembly occurred are depend on the curvature (Chapter 3). Thus, I expected that dehydration from ligand molecules on the nanoparticles with anisotropic shape will occur at different temperatures depending on the position, even using the single kind of ligand. I show the thermoresponsive two-step assembly process of gold nanorods coated with a single kind of ligand for the fabrication of hierarchical structures.

In Chapter 5, I summarize the thesis and afford the significance and prospects.

Chapter 2 *Synthesis of Janus-like Gold Nanoparticles with Hydrophilic/Hydrophobic Faces by Surface Ligand Exchange and their Self-Assemblies in Water*



Chapter 3 *Thermoresponsive assembly of Gold Nanospheres covered with oligo(ethylene glycol) derivatives with an Alkyl head*



Chapter 4 *Two-step Assembly of Thermoresponsive Gold Nanorods Coated with a Single Kind of Ligand*

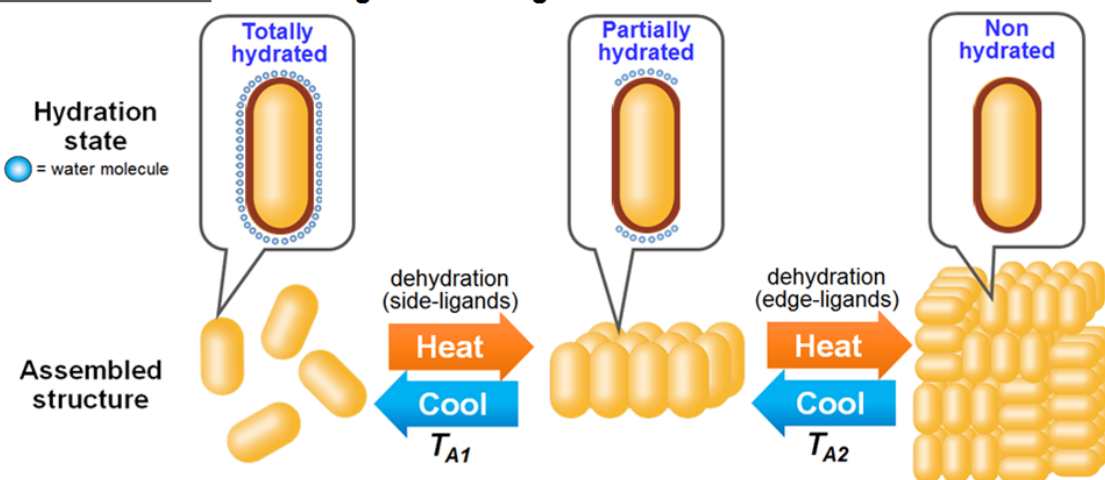


Figure 1-4. Schematic illustration of my doctoral thesis.

1-5. References

- (1) Whitesides, G. M. Nanoscience, Nanotechnology, and Chemistry. *Small* **2005**, *1*, 172–179.
- (2) Mody, V.; Siwale, R.; Singh, A.; Mody, H. Introduction to Metallic Nanoparticles. *J. Pharm. Bioallied Sci.* **2010**, *2*, 282.
- (3) Willets, K. A.; Van Duyne, R. P. Localized Surface Plasmon Resonance Spectroscopy and Sensing. *Annu. Rev. Phys. Chem.* **2007**, *58*, 267–297.
- (4) Herne, T. M.; Ahern, A.; Garrell, R. L. Surface-Enhanced Raman Spectroscopy of Peptides: Preferential N-Terminal Adsorption on Colloidal Silver. *J. Am. Chem. Soc.* **1991**, *113*, 846–854.
- (5) Joseph, V.; Engelbrekt, C.; Zhang, J.; Gernert, U.; Ulstrup, J.; Kneipp, J. Characterizing the Kinetics of Nanoparticle-Catalyzed Reactions by Surface-Enhanced Raman Scattering. *Angew. Chem. Int. Ed.* **2012**, *51*, 7592–7596.
- (6) Yao, H.; Zhang, Y.; Xiao, F.; Xia, Z.; Rao, J. Quantum Dot/bioluminescence Resonance Energy Transfer Based Highly Sensitive Detection of Proteases. *Angew. Chem. Int. Ed.* **2007**, *46*, 4346–4349.
- (7) Haruta, M.; Kobayashi, T.; Sano, H.; Yamada, N. Novel Gold Catalysts for the Oxidation of Carbon Monoxide at a Temperature Far Below 0 °C. *Chem. Lett.* **1987**, *16*, 405–408.
- (8) Ueda, A.; Haruta, M. Reduction of Nitrogen Monoxide with Propene over Au/Al₂O₃ Mixed Mechanically with Mn₂O₃. *Appl. Catal. B Environ.* **1998**, *18*, 115–121.
- (9) Du, K.; Zhu, Y.; Xu, H.; Yang, X. Multifunctional Magnetic Nanoparticles: Synthesis Modification and Biomedical Applications. *Prog. Chem.* **2011**, *23*, 2287–2298.
- (10) Kairdolf, B. A.; Smith, A. M.; Nie, S. One-Pot Synthesis, Encapsulation, and Solubilization of Size-Tuned Quantum Dots with Amphiphilic Multidentate Ligands. *J. Am. Chem. Soc.* **2008**, *130*, 12866–12867.
- (11) Qin, C.; Shen, J.; Hu, Y.; Ye, M. Facile Attachment of Magnetic Nanoparticles to Carbon Nanotubes via Robust Linkages and Its Fabrication of Magnetic Nanocomposites. *Compos. Sci. Technol.* **2009**, *69*, 427–431.

- (12) Freestone, I.; Meeks, N.; Sax, M.; Higgitt, C. The Lycurgus Cup — A Roman Nanotechnology. *Gold Bull.* **2007**, *40*, 270–277.
- (13) Faraday, M. The Bakerian Lecture: Experimental Relations of Gold (and Other Metals) to Light. *Philos. Trans. R. Soc. London* **1857**, *147*, 145–181.
- (14) Graham, T. Liquid Diffusion Applied to Analysis. *Philos. Trans. R. Soc. London* **1861**, *151*, 183–224.
- (15) Dreaden, E. C.; Alkilany, A. M.; Huang, X.; Murphy, C. J.; El-Sayed, M. A. The Golden Age: Gold Nanoparticles for Biomedicine. *Chem. Soc. Rev.* **2012**, *41*, 2740–2779.
- (16) Mie, G. Beiträge Zur Optik Trüber Medien, Speziell Kolloidaler Metallösungen. *Ann. Phys.* **1908**, *330*, 377–445.
- (17) J. Turkevich; Stevenson, P. C.; Hillier, J. A Study of the Nucleation and Growth Processes in the Synthesis of Colloidal Gold. *Discuss. Faraday Soc.* **1951**, *11*, 55.
- (18) Tsutsui, G.; Huang, S.; Sakaue, H.; Sshingubara, S.; Takahagi, T. Well-Size-Controlled Colloidal Gold Nanoparticles Dispersed in Organic Solvents. *Jpn. J. Appl. Phys.* **2001**, *40*, 346–349.
- (19) Wuithschick, M.; Birnbaum, A.; Witte, S.; Sztucki, M.; Vainio, U.; Pinna, N.; Rademann, K.; Emmerling, F.; Kraehnert, R.; Polte, J. Turkevich in New Robes: Key Questions Answered for the Most Common Gold Nanoparticle Synthesis. *ACS Nano* **2015**, *9*, 7052–7071.
- (20) Xia, H.; Xiahou, Y.; Zhang, P.; Ding, W.; Wang, D. Revitalizing the Frens Method to Synthesize Uniform, Quasi-Spherical Gold Nanoparticles with Deliberately Regulated Sizes from 2 to 330 Nm. *Langmuir* **2016**, *32*, 5870–5880.
- (21) Frens, G. Controlled Nucleation for the Regulation of the Particle Size in Monodisperse Gold Suspensions. *Nat. Phys. Sci.* **1973**, *241*, 20–22.
- (22) Brust, M.; Walker, M.; Bethell, D.; Schiffrin, D. J.; Whyman, R. Synthesis of Thiol-Derivatized Gold Nanoparticles in a Two-Phase Liquid-Liquid System. *Chem. Commun.* **1994**, 801–802.
- (23) Personick, M. L.; Mirkin, C. A. Making Sense of the Mayhem behind Shape Control in the Synthesis of Gold Nanoparticles. *J. Am. Chem. Soc.* **2013**, *135*,

18238–18247.

- (24) Grzelczak, M.; Pérez-Juste, J.; Mulvaney, P.; Liz-Marzán, L. M. Shape Control in Gold Nanoparticle Synthesis. *Chem. Soc. Rev.* **2008**, *37*, 1783–1791.
- (25) Vigderman, L.; Khanal, B. P.; Zubarev, E. R. Functional Gold Nanorods: Synthesis, Self-Assembly, and Sensing Applications. *Adv. Mater.* **2012**, *24*, 4811–4841.
- (26) Sau, T. K.; Murphy, C. J. Room Temperature , High-Yield Synthesis of Multiple Shapes of Gold Nanoparticles in Aqueous Solution. *J. Am. Chem. Soc.* **2004**, *126*, 8648–8649.
- (27) Zhai, Y.; DuChene, J. S.; Wang, Y. C.; Qiu, J.; Johnston-Peck, A. C.; You, B.; Guo, W.; Diciaccio, B.; Qian, K.; Zhao, E. W.; Ooi, F.; Hu, D.; Su, D.; Stach, E. A.; Zhu, Z.; Wei, W. D. Polyvinylpyrrolidone-Induced Anisotropic Growth of Gold Nanoprisms in Plasmon-Driven Synthesis. *Nat. Mater.* **2016**, *15*, 889–895.
- (28) Chen, L.; Ji, F.; Xu, Y.; He, L.; Mi, Y.; Bao, F.; Sun, B.; Zhang, X.; Zhang, Q. High-Yield Seedless Synthesis of Triangular Gold Nanoplates through Oxidative Etching. *Nano Lett.* **2014**, *14*, 7201–7206.
- (29) Scarabelli, L.; Coronado-Puchau, M.; Giner-Casares, J. J.; Langer, J.; Liz-Marzán, L. M. Monodisperse Gold Nanotriangles: Size Control, Large-Scale Self-Assembly, and Performance in Surface-Enhanced Raman Scattering. *ACS Nano* **2014**, *8*, 5833–5842.
- (30) Sauvage, J.-P. Transition Metal-Containing Rotaxanes and Catenanes in Motion: Toward Molecular Machines and Motors. *Acc. Chem. Res.* **1998**, *31*, 611–619.
- (31) Chen, H.; Shao, L.; Li, Q.; Wang, J. Gold Nanorods and Their Plasmonic Properties. *Chem. Soc. Rev.* **2013**, *42*, 2679–2724.
- (32) Sau, T. K.; Murphy, C. J.; Commun, M. L. H. C.; Commun, A. C. Seeded High Yield Synthesis of Short Au Nanorods in Aqueous Solution. *Langmuir* **2004**, *11*, 6414–6420.
- (33) Ye, X.; Jin, L.; Caglayan, H.; Chen, J.; Xing, G.; Zheng, C.; Doan-Nguyen, V.; Kang, Y.; Engheta, N.; Kagan, C. R.; Murray, C. B. Improved Size-Tunable Synthesis of Monodisperse Gold Nanorods through the Use of Aromatic Additives. *ACS Nano* **2012**, *6*, 2804–2817.

- (34) Murphy, C. J.; Lohse, S. E. The Quest for Shape Control: A History of Gold Nanorod Synthesis. *Chem. Mater.* **2013**, *25*, 1250–1261.
- (35) Badia, A.; Singh, S.; Demers, L.; Cuccia, L.; Brown, G. R.; Lennox, R. B. Self-Assembled Monolayers on Gold Nanoparticles. *Chem. Eur. J.* **1996**, *2*, 359–363.
- (36) Dahl, J. A.; Maddux, B. L. S.; Hutchison, J. E. Toward Greener Nanosynthesis. *Chem. Rev.* **2007**, *107*, 2228–2269.
- (37) Chen, F.; Li, X.; Hihath, J.; Huang, Z.; Tao, N. Effect of Anchoring Groups on Single-Molecule Conductance: Comparative Study of Thiol-, Amine-, and Carboxylic-Acid-Terminated Molecules. *J. Am. Chem. Soc.* **2006**, *128*, 15874–15881.
- (38) Nuzzo, R. G.; Zegarski, B. R.; Dubois, L. H. Fundamental Studies of the Chemisorption of Organosulfur Compounds on Au(111). Implications for Molecular Self-Assembly on Gold Surfaces. *J. Am. Chem. Soc.* **1987**, *109*, 733–740.
- (39) Vigderman, L.; Manna, P.; Zubarev, E. R. Quantitative Replacement of Cetyl Trimethylammonium Bromide by Cationic Thiol Ligands on the Surface of Gold Nanorods and Their Extremely Large Uptake by Cancer Cells. *Angew. Chem. Int. Ed.* **2012**, *51*, 636–641.
- (40) Zhu, Z. J.; Posati, T.; Moyano, D. F.; Tang, R.; Yan, B.; Vachet, R. W.; Rotello, V. M. The Interplay of Monolayer Structure and Serum Protein Interactions on the Cellular Uptake of Gold Nanoparticles. *Small* **2012**, *8*, 2659–2663.
- (41) Kanaras, A. G.; Kamounah, F. S.; Schaumburg, K.; Kiely, C. J.; Brust, M. Thioalkylated Tetraethylene Glycol: A New Ligand for Water Soluble Monolayer Protected Gold Clusters. *Chem. Commun.* **2002**, No. 20, 2294–2295.
- (42) Pengo, P.; Pasquato, L. Gold Nanoparticles Protected by Fluorinated Ligands: Syntheses, Properties and Applications. *J. Fluor. Chem.* **2015**, *177*, 2–10.
- (43) Zhao, L.; Seth, A.; Wibowo, N.; Zhao, C. X.; Mitter, N.; Yu, C.; Middelberg, A. P. J. Nanoparticle Vaccines. *Vaccine* **2014**, *32*, 327–337.
- (44) Ghosh, P.; Han, G.; De, M.; Kim, C. K.; Rotello, V. M. Gold Nanoparticles in Delivery Applications. *Adv. Drug Deliv. Rev.* **2008**, *60*, 1307–1315.
- (45) Rana, S.; Bajaj, A.; Mout, R.; Rotello, V. M. Monolayer Coated Gold

- Nanoparticles for Delivery Applications. *Adv. Drug Deliv. Rev.* **2012**, *64*, 200–216.
- (46) Lehn, J. M. Perspectives in Chemistry - Steps towards Complex Matter. *Angew. Chem. Int. Ed.* **2013**, *52*, 2836–2850.
- (47) Whitesides, G. M.; Grzybowski, B. Self-Assembly at All Scales. *Science* **2002**, *295*, 2418–2421.
- (48) Nie, Z.; Petukhova, A.; Kumacheva, E. Properties and Emerging Applications of Self-Assembled Structures Made from Inorganic Nanoparticles. *Nat. Nanotechnol.* **2010**, *5*, 15–25.
- (49) Jain, P. K.; El-Sayed, M. A. Plasmonic Coupling in Noble Metal Nanostructures. *Chem. Phys. Lett.* **2010**, *487*, 153–164.
- (50) Han, X.; Goebel, J.; Lu, Z.; Yin, Y. Role of Salt in the Spontaneous Assembly of Charged Gold Nanoparticles in Ethanol. *Langmuir* **2011**, *27*, 5282–5289.
- (51) Lin, S.; Li, M.; Dujardin, E.; Girard, C.; Mann, S. One-Dimensional Plasmon Coupling by Facile Self-Assembly of Gold Nanoparticles into Branched Chain Networks. *Adv. Mater.* **2005**, *17*, 2553–2559.
- (52) Chong, W. H.; Chin, L. K.; Tan, R. L. S.; Wang, H.; Liu, A. Q.; Chen, H. Stirring in Suspension: Nanometer-Sized Magnetic Stir Bars. *Angew. Chem. Int. Ed.* **2013**, *52*, 8570–8573.
- (53) He, J.; Liu, Y.; Babu, T.; Wei, Z.; Nie, Z. Self-Assembly of Inorganic Nanoparticle Vesicles and Tubules Driven by Tethered Linear Block Copolymers. *J. Am. Chem. Soc.* **2012**, *134*, 11342–11345.
- (54) Niikura, K.; Iyo, N.; Higuchi, T.; Nishio, T.; Jinnai, H.; Fujitani, N.; Ijiri, K. Gold Nanoparticles Coated with Semi-Fluorinated Oligo(ethylene Glycol) Produce Sub-100 Nm Nanoparticle Vesicles without Templates. *J. Am. Chem. Soc.* **2012**, *134*, 7632–7635.
- (55) Song, J.; Zhou, J.; Duan, H. Self-Assembled Plasmonic Vesicles of SERS-Encoded Amphiphilic Gold Nanoparticles for Cancer Cell Targeting and Traceable Intracellular Drug Delivery. *J. Am. Chem. Soc.* **2012**, *134*, 13458–13469.
- (56) Song, J.; Yang, X.; Jacobson, O.; Huang, P.; Sun, X.; Lin, L.; Yan, X.; Niu, G.;

- Ma, Q.; Chen, X. Ultrasmall Gold Nanorod Vesicles with Enhanced Tumor Accumulation and Fast Excretion from the Body for Cancer Therapy. *Adv. Mater.* **2015**, *27*, 4910–4917.
- (57) He, J.; Zhang, P.; Babu, T.; Liu, Y.; Gong, J.; Nie, Z. Near-Infrared Light-Responsive Vesicles of Au Nanoflowers. *Chem. Commun.* **2013**, *49*, 576–578.
- (58) Song, J.; Pu, L.; Zhou, J.; Duan, B.; Duan, H. Biodegradable Theranostic Plasmonic Vesicles of Amphiphilic Gold Nanorods. *ACS Nano* **2013**, *7*, 9947–9960.
- (59) Kotov, N. A. Inorganic Nanoparticles as Protein Mimics. *Science* **2010**, *330*, 188–189.
- (60) Shevchenko, E. V.; Talapin, D. V.; Kotov, N. A.; O'Brien, S.; Murray, C. B. Structural Diversity in Binary Nanoparticle Superlattices. *Nature* **2006**, *439*, 55–59.
- (61) Macfarlane, R. J.; Lee, B.; Jones, M. R.; Harris, N.; Schatz, G. C.; Mirkin, C. A. Nanoparticle Superlattice Engineering with DNA. *Science* **2011**, *334*, 204–208.
- (62) Levchenko, T. I.; Kübel, C.; Najafabadi, B. K.; Boyle, P. D.; Cadogan, C.; Goncharova, L. V.; Garreau, A.; Lagugné-Labarthe, F.; Huang, Y.; Corrigan, J. F. Luminescent CdSe Superstructures: A Nanocluster Superlattice and a Nanoporous Crystal. *J. Am. Chem. Soc.* **2017**, *139*, 1129–1144.
- (63) Prasad, B. L. V.; Sorensen, C. M.; Klabunde, K. J. Gold Nanoparticle Superlattices. *Chem. Soc. Rev.* **2008**, *37*, 1871.
- (64) Guerrero-Martínez, A.; Pérez-Juste, J.; Carbó-Argibay, E.; Tardajos, G.; Liz-Marzán, L. M. Gemini-Surfactant-Directed Self-Assembly of Monodisperse Gold Nanorods into Standing Superlattices. *Angew. Chem. Int. Ed.* **2009**, *48*, 9484–9488.
- (65) Mazid, R. R.; Si, K. J.; Cheng, W. DNA Based Strategy to Nanoparticle Superlattices. *Methods* **2014**, *67*, 215–226.
- (66) Niikura, K.; Iyo, N.; Matsuo, Y.; Mitomo, H.; Ijiri, K. Sub-100 Nm Gold Nanoparticle Vesicles as a Drug Delivery Carrier Enabling Rapid Drug Release upon Light Irradiation. *ACS Appl. Mater. Interfaces* **2013**, *5*, 3900–3907.
- (67) Chou, L. Y. T.; Zagorovsky, K.; Chan, W. C. W. DNA Assembly of Nanoparticle

- Superstructures for Controlled Biological Delivery and Elimination. *Nat. Nanotechnol.* **2014**, *9*, 148–155.
- (68) Liu, N.; Lu, Z.; Zhao, J.; McDowell, M. T.; Lee, H.-W.; Zhao, W.; Cui, Y. A Pomegranate-Inspired Nanoscale Design for Large-Volume-Change Lithium Battery Anodes. *Nat. Nanotechnol.* **2014**, *9*, 187–192.
- (69) Cho, E. S.; Kim, J.; Tejerina, B.; Hermans, T. M.; Jiang, H.; Nakanishi, H.; Yu, M.; Patashinski, A. Z.; Glotzer, S. C.; Stellacci, F.; Grzybowski, B. A. Ultrasensitive Detection of Toxic Cations through Changes in the Tunnelling Current across Films of Striped Nanoparticles. *Nat. Mater.* **2012**, *11*, 978–985.
- (70) Edel, J. B.; Kornyshev, A. A.; Urbakh, M. Self-Assembly of Nanoparticle Arrays for Use as Mirrors, Sensors, and Antennas. *ACS Nano* **2013**, *7*, 9526–9532.
- (71) Taylor, J.; Huefner, A.; Li, L.; Wingfield, J.; Mahajan, S. Nanoparticles and Intracellular Applications of Surface-Enhanced Raman Spectroscopy. *Analyst* **2016**, *141*, 5037–5055.
- (72) Ko, H.; Singamaneni, S.; Tsukruk, V. V. Nanostructured Surfaces and Assemblies as SERS Media. *Small* **2008**, *4*, 1576–1599.
- (73) Chen, G.; Wang, Y.; Yang, M.; Xu, U.; Goh, S. J.; Pan, M.; Chen, H. Measuring Ensemble-Averaged Surface-Enhanced Raman Scattering in the Hotspots of Colloidal Nanoparticle Dimers and Trimers. *J. Am. Chem. Soc.* **2010**, *132*, 3644–3645.
- (74) Bigioni, T. P.; Lin, X.-M.; Nguyen, T. T.; Corwin, E. I.; Witten, T. a; Jaeger, H. M. Kinetically Driven Self Assembly of Highly Ordered Nanoparticle Monolayers. *Nat. Mater.* **2006**, *5*, 265–270.
- (75) Liu, Y.; He, J.; Yang, K.; Yi, C.; Liu, Y.; Nie, L.; Khashab, N. M.; Chen, X.; Nie, Z. Folding Up of Gold Nanoparticle Strings into Plasmonic Vesicles for Enhanced Photoacoustic Imaging. *Angew. Chem. Int. Ed.* **2015**, *54*, 15809–15812.
- (76) Walther, A.; Mu, A. H. E. Janus Particles : Synthesis, Self-Assembly, Physical Properties, and Applications. *Chem. Rev.* **2013**, *113*, 5194–5261.
- (77) Pradhan, S.; Xu, L. P.; Chen, S. Janus Nanoparticles by Interfacial Engineering. *Adv. Funct. Mater.* **2007**, *17*, 2385–2392.

- (78) Bishop, K. J. M.; Wilmer, C. E.; Soh, S.; Grzybowski, B. A. Nanoscale Forces and Their Uses in Self-Assembly. *Small* **2009**, *5*, 1600–1630.
- (79) Young, K. L.; Jones, M. R.; Zhang, J.; Macfarlane, R. J.; Esquivel-Sirvent, R.; Nap, R. J.; Wu, J.; Schatz, G. C.; Lee, B.; Mirkin, C. A. Assembly of Reconfigurable One-Dimensional Colloidal Superlattices due to a Synergy of Fundamental Nanoscale Forces. *Proc. Natl. Acad. Sci.* **2012**, *109*, 2240–2245.
- (80) Caswell, K. K.; Wilson, J. N.; Bunz, U. H. F.; Murphy, C. J. Preferential End-to-End Assembly of Gold Nanorods by Biotin-Streptavidin Connectors. *J. Am. Chem. Soc.* **2003**, *125*, 13914–13915.
- (81) Mochizuki, C.; Shinmori, H. Light-Triggered Assembly of Gold Nanorods Based on Photoisomerization of Spiropyrans. *Chem. Lett.* **2017**, *46*, 469–472.
- (82) Indrasekara, A. S. D. S.; Wadams, R. C.; Fabris, L. Ligand Exchange on Gold Nanorods: Going back to the Future. *Part. Part. Syst. Charact.* **2014**, *31*, 819–838.
- (83) Nie, Z.; Fava, D.; Kumacheva, E.; Zou, S.; Walker, G. C.; Rubinstein, M. Self-Assembly of Metal-Polymer Analogues of Amphiphilic Triblock Copolymers. *Nat. Mater.* **2007**, *6*, 609–614.
- (84) Nie, Z.; Fava, D.; Rubinstein, M.; Kumacheva, E. “Supramolecular” Assembly of Gold Nanorods End-Terminated with Polymer “Pom-Poms”: Effect of Pom-Pom Structure on the Association Modes. *J. Am. Chem. Soc.* **2008**, *130*, 3683–3689.
- (85) Zhu, M. Q.; Wang, L. Q.; Exarhos, G. J.; Li, A. D. Q. Thermosensitive Gold Nanoparticles. *J. Am. Chem. Soc.* **2004**, *126*, 2656–2657.
- (86) Liu, F.; Agarwal, S. Thermoresponsive Gold Nanoparticles with Positive UCST-Type Thermoresponsivity. *Macromol. Chem. Phys.* **2015**, *216*, 460–465.
- (87) Lin, Y.; Xia, X.; Wang, M.; Wang, Q.; An, B.; Tao, H.; Xu, Q.; Omenetto, F.; Kaplan, D. L. Genetically Programmable Thermoresponsive Plasmonic Gold/silk-Elastin Protein Core/shell Nanoparticles. *Langmuir* **2014**, *30*, 4406–4414.
- (88) Jones, S. T.; Walsh-Korb, Z.; Barrow, S. J.; Henderson, S. L.; Del Barrio, J.; Scherman, O. A. The Importance of Excess Poly(N-Isopropylacrylamide) for the Aggregation of Poly(N-Isopropylacrylamide)-Coated Gold Nanoparticles. *ACS*

- Nano* **2016**, *10*, 3158–3165.
- (89) Liu, Y.; Han, X.; He, L.; Yin, Y. Thermoresponsive Assembly of Charged Gold Nanoparticles and Their Reversible Tuning of Plasmon Coupling. *Angew. Chem. Int. Ed.* **2012**, *51*, 6373–6377.
- (90) Kurzhals, S.; Zirbs, R.; Reimhult, E. Synthesis and Magneto-Thermal Actuation of Iron Oxide Core–PNIPAM Shell Nanoparticles. *ACS Appl. Mater. Interfaces* **2015**, *7*, 19342–19352.
- (91) Torii, Y.; Sugimura, N.; Mitomo, H.; Niikura, K.; Ijio, K. pH-Responsive Coassembly of Oligo(ethylene Glycol)-Coated Gold Nanoparticles with External Anionic Polymers via Hydrogen Bonding. *Langmuir* **2017**, *33*, 5537–5544.
- (92) Orendorff, C. J.; Hankins, P. L.; Murphy, C. J. pH-Triggered Assembly of Gold Nanorods. *Langmuir* **2005**, *21*, 2022–2026.
- (93) Tian, Z.; Yang, C.; Wang, W.; Yuan, Z. Shieldable Tumor Targeting Based on pH Responsive Self-Assembly / Disassembly of Gold Nanoparticles. *ACS Appl. Mater. Interfaces* **2014**, *6*, 17865–17876.
- (94) Klajn, R.; Bishop, K. J. M.; Grzybowski, B. A. Light-Controlled Self-Assembly of Reversible and Irreversible Nanoparticle Suprastructures. *Proc. Natl. Acad. Sci. U. S. A.* **2007**, *104*, 10305–10309.
- (95) Kundu, P. K.; Samanta, D.; Leizrowice, R.; Margulis, B.; Zhao, H.; Börner, M.; Udayabhaskararao, T.; Manna, D.; Klajn, R. Light-Controlled Self-Assembly of Non-Photoresponsive Nanoparticles. *Nat. Chem.* **2015**, *7*, 646–652.
- (96) Qiu, H.; Hudson, Z. M.; Winnik, M. A.; Manners, I. Multidimensional Hierarchical Self-Assembly of Amphiphilic Cylindrical Block Comicelles. *Science* **2015**, *347*, 1329–1332.
- (97) Yeom, B.; Sain, T.; Lacevic, N.; Bukharina, D.; Cha, S.-H.; Waas, A. M.; Arruda, E. M.; Kotov, N. A. Abiotic Tooth Enamel. *Nature* **2017**, *543*, 95–98.
- (98) Tsang, B.; Yu, C.; Granick, S. Polymers Zippered-up by Electric Charge Reveal Themselves. *ACS Nano* **2014**, *8*, 11030–11034.
- (99) Studart, A. R. Towards High-Performance Bioinspired Composites. *Adv. Mater.* **2012**, *24*, 5024–5044.

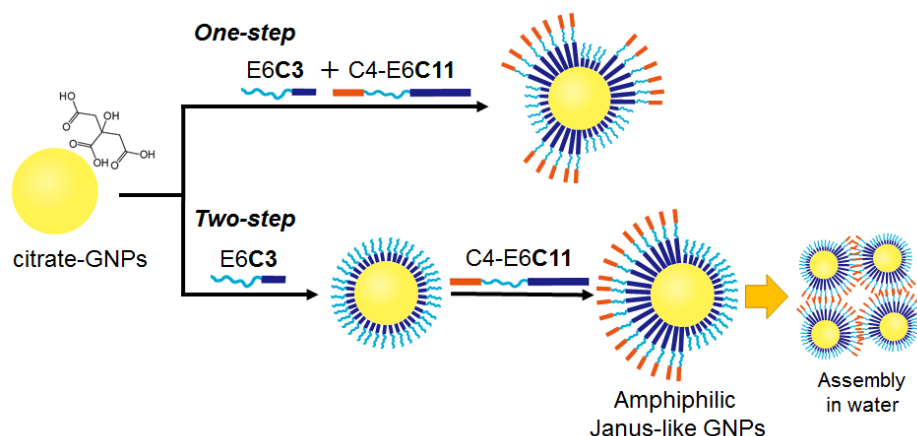
- (100) Zhou, Y.; Marson, R. L.; Van Anders, G.; Zhu, J.; Ma, G.; Ercius, P.; Sun, K.; Yeom, B.; Glotzer, S. C.; Kotov, N. A. Biomimetic Hierarchical Assembly of Helical Supraparticles from Chiral Nanoparticles. *ACS Nano* **2016**, *10*, 3248–3256.
- (101) Miszta, K.; de Graaf, J.; Bertoni, G.; Dorfs, D.; Brescia, R.; Marras, S.; Ceseracciu, L.; Cingolani, R.; van Roij, R.; Dijkstra, M.; Manna, L. Hierarchical Self-Assembly of Suspended Branched Colloidal Nanocrystals into Superlattice Structures. *Nat. Mater.* **2011**, *10*, 872–876.
- (102) Kudryashov, D. S.; Reisler, E. ATP and ADP Actin States. *Biopolymers* **2013**, *99*, 245–256.

Chapter 2

*Synthesis of Janus-like Gold Nanospheres with
Hydrophilic/Hydrophobic Faces by Surface Ligand Exchange
and their Self-Assemblies in Water*

Abstract:

This study aims at the synthesis of Janus gold nanospheres (Janus GNSs) with hydrophilic/hydrophobic faces by a simple ligand exchange reaction in an homogeneous system and at the elucidation of the self-assembled structures of the Janus GNSs in water. As hydrophilic surface ligands, I synthesized hexaethylene glycol (E6)-terminated thiolate ligands with C3, C7, or C11 alkyl chains, referred to as **E6C3**, **E6C7**, and **E6C11**, respectively. As a hydrophobic ligand, a butyl-headed thiolate ligand **C4-E6C11**, in which a C4 alkyl was introduced on the **E6C11** terminus, was synthesized. The degree of segregation between the two ligands on the GNSs (5 nm in diameter) was examined by matrix-assisted laser desorption/ionization time-of flight mass spectrometry (MALDI-TOF MS) analysis. I found that the choice of immobilization methods, one-step or two-step addition of the two ligands to the GNS solution, crucially affects the degree of segregation. The two-step addition of a hydrophilic ligand (**E6C3**) followed by a hydrophobic ligand (**C4-E6C11**) produced a large degree of segregation on the GNSs, providing Janus-like GNSs. When dispersed in water, these Janus-like GNSs formed assemblies of ~ 160 nm in diameter, whereas Domain GNSs, in which the two ligands formed partial domains on the surface, were precipitated even when the molar ratio of the hydrophilic ligand and the hydrophobic ligand on the surface of the GNSs was almost 1:1. The assembled structure of the Janus-like GNSs in water was directly observed by pulsed coherent X-ray solution scattering using an X-ray free-electron laser, revealing irregular spherical structures with uneven surfaces.



2-1. Introduction

For the controlled assembly of nano- or micro-particles, anisotropic surface modification has been proposed and applied to the synthesis of smart building blocks.¹⁻⁵ In particular, Janus nanoparticles with two different surface properties on a single sphere, providing hydrophilic and hydrophobic characteristics, have been demonstrated to provide various types of 3D nanoparticle assemblies^{2,6,7} inspired by amphiphilic biomolecules, including lipids and some proteins, which spontaneously assemble into various structures in water. The biomimetic assembly of amphiphilic nanoparticles is expected to afford complex, hierarchical and controlled systems made up of functional nanoparticles.

Several simulation studies have demonstrated that Janus particles self-assemble into micelle- or worm-like string structures.⁸⁻¹⁰ Granick *et al.* reported that amphiphilic Janus microparticles (1 μm in diameter) could assemble into specific clusters and strings as predicted by simulation studies.⁸ In particular, as the size and shape of gold nanoparticles (GNPs) assemblies can be easily controlled,^{11,12} GNPs can be good building blocks for the investigation of the self-assembly behaviors of nanoparticles into large 3D structures. Furthermore, GNP assemblies offer an intriguing candidate for the construction of building blocks due to their optical and electronic properties, making them suitable for applications to optical and medical therapeutic devices.¹³

Surface modification of spherical GNPs (GNSs) to produce Janus particles has been achieved at the air-liquid, air-solid, and liquid-liquid interfaces.¹⁴⁻¹⁷ For example, Bishop *et al.* reported the synthesis of amphiphilic GNSs at the toluene-water interface.¹⁴ They also proposed nanoparticles with an adaptive surface, where hydrophobic and hydrophilic surface ligands toothless on GNSs, were able to be rearranged to promote the assembly

of nanoparticles.¹⁷ Li *et al.* demonstrated a synthetic route to amphiphilic Janus GNSs displaying both hydrophilic and hydrophobic polymers *via* a combination of “grafting-to” and “grafting-from” methods on a solid surface.¹⁵

The synthesis of such amphiphilic Janus GNSs in homogeneous systems offers the advantages of simplicity with applicability to large-scale production. Stellacci *et al.* reported that two immiscible ligands form Janus GNSs when the core size is smaller than 3 nm.¹⁸ Cliffler *et al.* reported the synthesis of Janus GNSs (2~3 nm in a diameter) using phase segregation of two ligands on a surface and the analytical method of the phase segregation using matrix-assisted laser desorption/ionization ion mobility-mass spectrometry (MALDI-IM MS).¹⁹ However, for the application of nanoparticle assemblies to optical devices, the large nanoparticles are often required due to their strong coupling with light.

In this chapter, I present the synthesis of Janus-like GNSs with hydrophilic/hydrophobic faces with a diameter of 5 nm. This study has two objectives: (1) quantitative analysis of the phase segregation of the two ligands with different alkyl chain lengths toward the formation of Janus GNSs with hydrophilic/hydrophobic faces and (2) the observation of self-assembled GNS structures with a Janus-type surface in water. Two thiolated ligands with different alkyl chains have been shown to segregate into patched monolayers on a flat gold surface.^{20,21} With the aim of inducing phase segregation of the GNSs to give Janus-type separation, I synthesized various hexaethylene glycol ligands with different alkyl chains (C3, C7 and C11, see scheme 1-1). The degree of segregation of the two ligands was analyzed by matrix-assisted laser desorption/ionization time-of flight mass spectrometry (MALDI-TOF MS) according to Cliffler’s method.¹⁹

Furthermore, I revealed the self-assembled structure of Janus GNSs with hydrophilic/hydrophobic faces in water. As GNSs with a Janus-type surface are the simplest anisotropic nanoparticles, the self-assembly of these NPs has been discussed as a model of amphiphilic molecules. Several studies have reported the self-assembled structures of amphiphilic Janus GNSs using atomic force microscopy (AFM) or transmission electron microscopy (TEM).^{9,10} However, as AFM or TEM observations were performed on a solid substrate, the observed structures might have been influenced by the drying process of the samples or their association with the substrates. X-ray laser diffraction has been proven to be a powerful method for the high-resolution imaging of samples without causing radiation damage.²²⁻²⁵ Pulsed coherent X-ray solution scattering (PCXSS), in particular, has been successfully applied to capture snapshots of living cells in solution.^{25,26} Here, I took direct images of the assemblies of Janus-like GNSs dispersed in water using the PCXSS method to investigate the self-assembled structures.

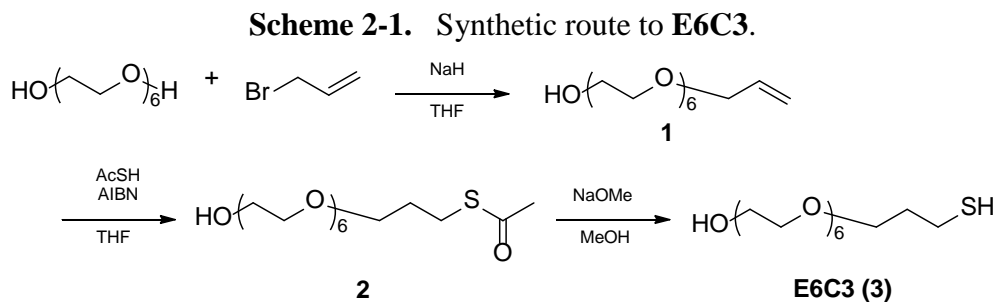
2-2. Experimental section

2-2-1. General information

All commercially available reagents were used without further purification. All solvents were purchased from Wako Pure Chemical Industries Ltd. (Japan) and used without further purification. Thin-layer chromatography (TLC) was performed on glass-backed pre-coated silica gel plates (60F254, Merck & Co., Inc., USA). Products were isolated by column chromatography on silica-gel (Kanto Chemical, neutral 60N, 40-50 μm). NMR spectra were recorded on a 400 MHz JEOL spectrometer. MALDI-TOF mass spectra were measured with a Voyager-DE STR-H mass spectrometer (Applied Biosystems) with 2,5-dihydroxybenzoic acid as a matrix. Citrate-protected GNSs in aqueous solution (5 nm in a diameter) were purchased from British Biocell International, Ltd. (Britain). GNSs were concentrated with a CF-16RX centrifuge (Hitachi-Koki, Ltd., Japan). Dynamic light scattering (DLS) analysis was performed using a Delsa Nano HC system (Beckman Coulter, Inc., Japan). Scanning transmission electron microscope (STEM) images were obtained using a STEM HD-2000 system (Hitachi High-Tech Manufacturing & Service Co., Ltd., Japan) with an accelerating voltage of 200 kV.

2-2-2. Thiolate ligand synthesis

• Synthesis of E6C3

*3,6,9,12,15,18-hexaoxahenicos-20-en-1-ol, 1*

Hexa(ethylene)glycol (30 g, 0.11 mol) was dissolved in THF (110 ml). The solution was cooled on ice and added the 60% NaH in oil (3.2 g, 80 mmol) and 3-bromoprop-1-ene (5.2 ml, 61 mmol). The reaction was allowed to warm to room temperature and stirred overnight. The solvent was removed, the residue was dissolved in CHCl_3 and washed twice with sat. NaCl solution. The organic layer was dried over anhydrous Na_2SO_4 . The crude product was concentrated in vacuo and purified by flash chromatography on silica gel (CHCl_3 to 9:1 EtOAc/MeOH) to yield **1** (13.2 g, 67 %) as a clear syrup.

^1H NMR (400 MHz, CDCl_3): δ /ppm = 3.38-3.88 (m, 26H, $-\text{O}-\text{CH}_2-$), 4.03 (br-d, 2H, $J = 5.8$ Hz, $-\text{O}-\text{CH}_2-$), 5.17-5.30 (m, 2H, $-\text{CH}=\text{CH}_2$), 5.87-5.97 (m, 1H, $-\text{CH}=\text{CH}_2$).

MALDI-TOF-MS (m/z): $[\text{M}+\text{Na}]^+$ calcd for $\text{C}_{15}\text{H}_{30}\text{O}_7\text{Na}$, 345.19; found, 345.17.

23-methyl-3,6,9,12,15,18-hexaoxa-22-thiatetracos-23-en-1-ol, 2

Compound **1** (1.5 g, 4.7 mmol), AcSH (1.77 g, 23 mmol), and 2,2'-azobisobutyronitrile (0.76 g, 4.7 mmol) were dissolved in stabilizer free dry THF (30 mL). The mixture was stirred for 3 h at 80°C . The crude product was concentrated in vacuo and purified by flash

chromatography on silica gel (4:1 CHCl₃/EtOAc to 9:1 EtOAc/MeOH) to yield **2** (1.5 g, 81 %) as a clear syrup.

¹H NMR (400 MHz, CDCl₃): δ/ppm = 1.86 (quin, 2H, *J* = 6.8 Hz, -CH₂-CH₂-CH₂-), 2.33(br-s, 3H, CH₃CO), 2.95 (t, 2H, *J* = 7.1 Hz, -CH₂-S-), 3.51 (br-t, *J* = 6.2 Hz, HO-CH₂-), 3.56-3.80 (m, 22H, -O-CH₂-).

MALDI-TOF-MS (m/z): [M+Na]⁺ calcd for C₁₇H₃₄O₈SNa, 421.19; found, 421.21.

21-mercapto-3,6,9,12,15,18-hexaoxahenicosan-1-ol, 3

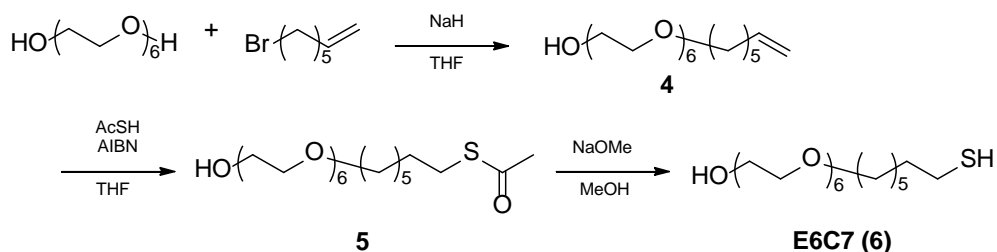
Compound **2** (0.45 g, 1.1 mmol) and NaOMe (28 % MeOH solution, 15 μl, 0.077 mmol) were dissolved in 20 mL MeOH, and the mixture was stirred over 8 h at room temperature. The mixture was neutralized with Dowex (50WX8-200). After filtration through the filter paper, the solvent was removed under vacuum. The residue was dissolved in CHCl₃ and washed twice with sat. NaCl solution. The organic layer was dried over anhydrous Na₂SO₄. The crude product was concentrated *in vacuo* and purified by flash chromatography on silica gel (CHCl₃ to 4:1 EtOAc/MeOH) to yield **3** (0.16 g, 41 %) as a clear syrup.

¹H NMR (400 MHz, CDCl₃): δ/ppm = 1.39 (t, 1H, *J* = 7.8 Hz, -SH) 1.88 (quin, 2H, *J* = 6.6 Hz, -CH₂-CH₂-CH₂-), 2.63 (q, 2H, *J* = 7.5 Hz, -CH₂-SH), 2.79 (s, 1H, -OH), 3.54-3.73 (m, 26H, -O-CH₂-).

MALDI-TOF-MS (m/z): [M+Na]⁺ calcd for C₁₅H₃₂O₇SNa, 379.18; found, 379.21. HR-MS (ESI): calcd for C₁₅H₃₂O₇SNa [M+Na]⁺ 379.17610, found 379.17657.

- **Synthesis of E6C7**

Scheme 2-2. Synthetic route to **E6C7**.



3,6,9,12,15,18-hexaoxapentacos-24-en-1-ol, **4**

Hexa(ethylene)glycol (15 g, 53 mmol) was dissolved in THF (55 ml). The solution was cooled on ice and added the 60% NaH in oil (1.6 g, 40 mmol) and 7-bromo-1-heptene (5.2 ml, 31 mmol). The reaction was allowed to warm to room temperature and stirred overnight. The solvent was removed, the residue was dissolved in CHCl_3 and washed twice with sat. NaCl solution. The organic layer was dried over anhydrous Na_2SO_4 . The crude product was concentrated *in vacuo* and purified by flash chromatography on silica gel (4:1 $\text{CHCl}_3/\text{EtOAc}$ to 9:1 EtOAc/MeOH) to yield **4** (8.7 g, 66 %) as a clear syrup.

^1H NMR (400 MHz, CDCl_3): δ /ppm = 1.29-1.45 (m, 4H, alkyl chain), 1.59 (quin, 2H, $J = 7.3$ Hz, alkyl chain), 2.01-2.09 (m, 2H, $=\text{CH}-\text{CH}_2$), 3.45 (t, 2H, $J = 6.8$ Hz, $-\text{O}-\text{CH}_2-$), 3.56-3.75 (m, 24H, $-\text{O}-\text{CH}_2-$), 4.90-5.04 (m, 2H, $-\text{CH}=\text{CH}_2$), 5.74-5.87 (m, 1H, $-\text{CH}=\text{CH}_2$).

MALDI-TOF-MS (m/z): $[\text{M}+\text{Na}]^+$ calcd for $\text{C}_{19}\text{H}_{38}\text{O}_7\text{Na}$, 401.49; found, 401.38.

S-(1-hydroxy-3,6,9,12,15,18-hexaoxapentacosan-25-yl) ethanethioate, **5**

Compound **4** (1.5 g, 4.0 mmol), AcSH (1.5 g, 2.0 mmol), and 2,2'-azobisobutyronitrile (0.65 g, 4.0 mmol) were dissolved in stabilizer free dry THF (30 mL). The mixture was

stirred for 3 h at 80°C. The mixture was evaporated under vacuum. The residue was dissolved in CHCl₃ washed twice with sat. NaCl solution. The organic layer was dried over Na₂SO₄. The crude product was concentrated *in vacuo* and purified by flash chromatography on silica gel (4:1 CHCl₃/EtOAc to 9:1 EtOAc/MeOH) to yield **5** (1.5 g, 81 %) as a clear syrup.

¹H NMR (400MHz, CDCl₃): δ/ppm = 1.22-1.41 (m, 6H, alkyl chain), 1.50-1.62(m, 4H, alkyl chain), 2.32 (s, 3H, CH₃-CO-), 2.86 (t, 2H, *J* = 7.3 Hz, -CH₂-S-), 3.44 (t, 2H, *J* = 6.9 Hz, HO-CH₂-), 3.55-3.76 (m, 22H, -O-CH₂-).

MALDI-TOF-MS (m/z): [M+Na]⁺ calcd for C₂₁H₄₂O₈SNa, 477.61; found, 477.16.

25-mercapto-3,6,9,12,15,18-hexaoxapentacosan-1-ol, **6**

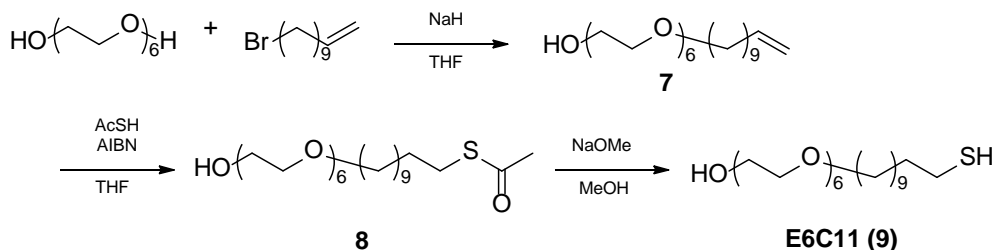
Compound **5** (0.32 g, 0.70 mmol) and NaOMe (28 % MeOH solution, 20 μl, 0.10 mmol) were dissolved in 20 mL MeOH, and the mixture was stirred over night at 30°C. The mixture was neutralized with Dowex (50WX8-200). After filtration through the filter paper, the solvent was removed under vacuum. The residue was dissolved in CHCl₃ and washed twice with sat. NaCl solution. The organic layer was dried over anhydrous Na₂SO₄. The crude product was concentrated *in vacuo* and purified by flash chromatography on silica gel (9:1 EtOAc/MeOH) to yield **6** (0.07 g, 23 %) as a clear syrup.

¹H NMR (400 MHz, CDCl₃): δ/ppm = 1.23-1.44 (m, 6H, alkyl chain), 1.52-1.70 (m, 4H, alkyl chain), 2.52 (q, 2H, *J* = 6.9 Hz, -CH₂-SH), 3.43 (t, 2H, *J* = 6.8 Hz, -O-CH₂-), 3.55-3.79 (m, 24H, -O-CH₂-)

MALDI-TOF-MS (m/z): [M+Na]⁺ calcd for C₁₅H₃₂O₇SNa, 435.57; found, 435.34. HR-MS (ESI): calcd for C₁₉H₄₀O₇SNa [M+Na]⁺ 435.23870, found 435.23922.

- **Synthesis of E6C11**

Scheme 2-3. Synthetic route to **E6C11**.



3,6,9,12,15,18-hexaoxapentacos-24-en-1-ol, 7

Hexa(ethylene)glycol (15 g, 53 mmol) was dissolved in THF (55 ml). The solution was cooled on ice and added the 60% NaH in oil (1.6 g, 40 mmol) and 11-bromo-1-undecene (4.2 ml, 28 mmol). The reaction was allowed to warm to room temperature and stirred overnight. The solvent was removed, the residue was dissolved in CHCl_3 and washed twice with sat. NaCl solution. The organic layer was dried over anhydrous Na_2SO_4 . The crude product was concentrated *in vacuo* and purified by flash chromatography on silica gel (4:1 $\text{CHCl}_3/\text{EtOAc}$ to 9:1 EtOAc/MeOH) to yield **7** (8.7 g, 66 %) as a clear syrup.

^1H NMR (400 MHz, CDCl_3): δ /ppm = 1.21-1.42 (m, 14H, alkyl chain), 1.59 (quin, 2H, $J=7.32$ Hz, alkyl chain), 2.01-2.09 (m, 2H, $=\text{CH}-\text{CH}_2$), 3.45 (t, 2H, $J=6.8$ Hz, $-\text{O}-\text{CH}_2-$), 3.56-3.75 (m, 22H, $-\text{O}-\text{CH}_2-$), 4.90-5.04 (m, 2H, $-\text{CH}=\text{CH}_2$), 5.74-5.87 (m, 1H, $-\text{CH}=\text{CH}_2$). MALDI-TOF-MS (m/z): $[\text{M}+\text{Na}]^+$ calcd for $\text{C}_{19}\text{H}_{38}\text{O}_7\text{Na}$, 457.60; found, 457.38.

S-(1-hydroxy-3,6,9,12,15,18-hexaoxapentacosan-25-yl) ethanethioate, 8

Compound **7** (1.5 g, 3.4 mmol), AcSH (1.3 g, 1.7 mmol), and 2,2'-azobisobutyronitrile (0.56 g, 3.4 mmol) were dissolved in stabilizer free dry THF (30 mL). The mixture was

stirred for 3 h at 80°C. The mixture was evaporated under vacuum. The residue was dissolved in CHCl₃ washed twice with sat. NaCl solution. The organic layer was dried over anhydrous Na₂SO₄. The crude product was concentrated *in vacuo* and purified by flash chromatography on silica gel (CHCl₃ to 98:2 EtOAc/MeOH) to yield **8** (0.85 g, 49 %) as a clear syrup.

¹H NMR (400 MHz, CDCl₃): δ/ppm = 1.20-1.41 (m, 14H, alkyl chain), 1.51-1.61 (m, 4H, alkyl chain), 2.32 (s, 3H, CH₃-CO-), 2.86 (t, 2H, *J* = 7.8 Hz, -CH₂-S-), 3.44 (t, 2H, *J* = 6.9 Hz, HO-CH₂-), 3.56-3.77 (m, 22H, -O-CH₂-). MALDI-TOF-MS (m/z): [M+Na]⁺ calcd for C₂₁H₄₂O₈SNa, 533.71; found, 533.32.

25-mercapto-3,6,9,12,15,18-hexaoxapentacosan-1-ol, 9

Compound **8** (0.40 g, 0.78 mmol) and NaOMe (28 % MeOH solution, 20 μl, 0.10 mmol) were dissolved in 20 mL MeOH, and the mixture was stirred over night at 30°C. The mixture was neutralized with Dowex (50WX8-200). After filtration through the filter paper, the solvent was removed under vacuum. The residue was dissolved in CHCl₃ and washed twice with sat. NaCl solution. The organic layer was dried over anhydrous Na₂SO₄. The crude product was concentrated *in vacuo* and purified by flash chromatography on silica gel (99:1 CHCl₃/MeOH) to yield **9** (0.16 g, 41 %) as a clear syrup.

¹H NMR (400 MHz, CDCl₃): δ/ppm = 1.28-1.45 (m, 14H, alkyl chain), 1.49-1.74 (m, 4H, alkyl chain), 2.44-2.74 (m, 2H, CH₂-SH), 3.44 (t, 2H, *J* = 6.9 Hz, -O-CH₂-CH₂), 3.51-3.87 (m, 24H, -O-CH₂-). MALDI-TOF-MS (m/z): [M+Na]⁺ calcd for C₁₅H₃₂O₇SNa, 491.30; found, 491.35. HR-MS (ESI): calcd for C₂₃H₄₈O₇SNa [M+Na]⁺ 491.30130, found 491.30215.

5,8,11,14,17,20,23-heptaoxatetatriacont-33-ene, 11

1-Butanol (10 mL) was dissolved in dry THF (10 mL). The solution was cooled on ice and added the 60% NaH in oil (0.15 g, 3.8 mmol). After N₂ gas generation, compound **10** in THF (10 mL) was added dropwise. The reaction was allowed to warm to 40°C and stirred 4h. The solvent was removed, and the residue was dissolved in CHCl₃ and washed twice with sat. NaCl solution. The organic layer was dried over anhydrous Na₂SO₄. The crude product was concentrated *in vacuo* and purified by flash chromatography on silica gel (CHCl₃) to yield **11** (0.16 g, 49 %) as a clear syrup.

¹H NMR (400 MHz, CDCl₃): δ /ppm = 0.91 (t, 3H, *J* = 7.54 Hz, CH₃ methyl), 1.21-1.41 (m, 14H, alkyl chain), 1.52-1.69 (m, 4H, alkyl chain), 2.04 (q, 2H, *J* = 7.4 Hz, =CH-CH₂), 3.45 (q, 4H, *J* = 5.5 Hz, -O-CH₂-), 3.56-3.60 (m, 4H, -O-CH₂-), 3.26-3.70 (m, 20H, -O-CH₂-), 4.89-5.03 (m, 2H, -CH=CH₂), 5.75-5.88 (m, 1H, -CH=CH₂).

MALDI-TOF-MS (m/z): [M+Na]⁺ calcd for C₂₇H₅₄O₇Na, 513.70; found, 513.35.

S-5,8,11,14,17,20,23-heptaoxatetatriacontan-34-yl ethanethioate, 12

Compound **11** (0.16 g, 0.33 mmol), AcSH (125 mg, 1.65 mmol), and 2,2'-azobisisobutyronitrile (54 mg, 0.33 mmol) were dissolved in stabilizer free dry THF (20 mL). The mixture was refluxed for 5 h. The solvent was removed, the residue was dissolved in CHCl₃ and washed twice with NaCl sat. solution. The organic layer was dried over anhydrous Na₂SO₄. The crude product was concentrated *in vacuo* and purified by flash chromatography on silica gel (CHCl₃) to yield **12** (0.19 g, 74 %) as a clear syrup.

¹H NMR (400 MHz, CDCl₃): δ /ppm = 0.91 (t, 3H, *J* = 7.3 Hz, CH₃ methyl), 1.21-1.42 (m, 14H, alkyl chain), 1.50-1.65 (m, 4H, alkyl chain), 2.32 (s, 3H, *J* = 7.4 Hz, -CH₂-SH), 3.45 (q, 4H, *J* = 5.5 Hz, -O-CH₂-), 3.55-3.77 (m, 24H, -O-CH₂-).

MALDI-TOF-MS (m/z): $[M+Na]^+$ calcd for $C_{19}H_{38}O_7Na$, 589.82; found, 589.31, $[M+K]^+$ calcd for $C_{15}H_{30}O_7K$, 605.93; found, 605.30.

5,8,11,14,17,20,23-heptaooxatetracontane-34-thiol, **13**

Compound **4** (0.14 g, 0.26 mmol) and 28% NaOMe in MeOH (15 μ L, 0.077 mmol) were dissolved in MeOH (10 mL), and the mixture was stirred over 4 h at 50°C. The neutralization was carried out by the addition of Dowex (50WX8-200). After the filtration through the filter paper, the solvent was removed under vacuum. The residue was dissolved in $CHCl_3$ and washed twice with NaCl sat. solution. The organic layer was dried over anhydrous Na_2SO_4 . The crude product was concentrated *in vacuo* and purified by flash chromatography on silica gel (9:1 $CHCl_3$ /Hexane) to yield **13** (32.7 mg, 25 %) as a clear syrup.

1H NMR (400 MHz, $CDCl_3$): δ /ppm = 0.91 (t, 3H, $J = 7.3$ Hz, CH_3 methyl), 1.23-1.43 (m, 14H, alkyl chain), 1.52-1.65 (m, 4H, alkyl chain), 2.52 (q, 2H, $J = 7.3$ Hz, CH_3 -CO-), 3.45 (q, 4H, $J = 6.4$ Hz, -O- CH_2 -), 3.56-3.70 (m, 24H, -O- CH_2 -).

MALDI-TOF-MS (m/z): $[M+Na]^+$ calcd for $C_{27}H_{56}O_7Na$, 547.78; found, 547.44. HR-MS (ESI): calcd for $C_{27}H_{56}O_7SNa$ $[M+Na]^+$ 547.36390, found 547.36465.

- $^1\text{H-NMR}$ spectra of ligands

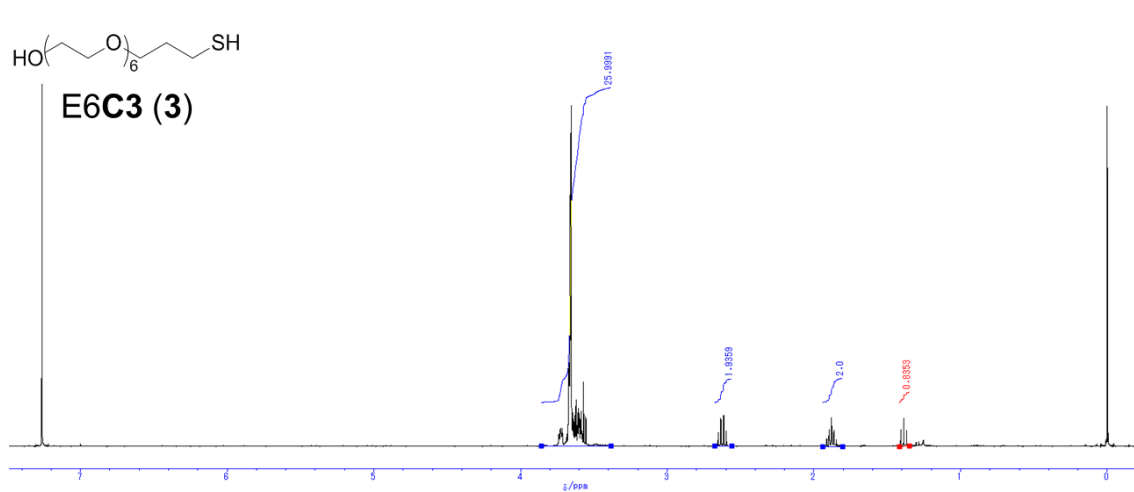


Figure 2-1. $^1\text{H NMR}$ spectrum of **E6C3**.

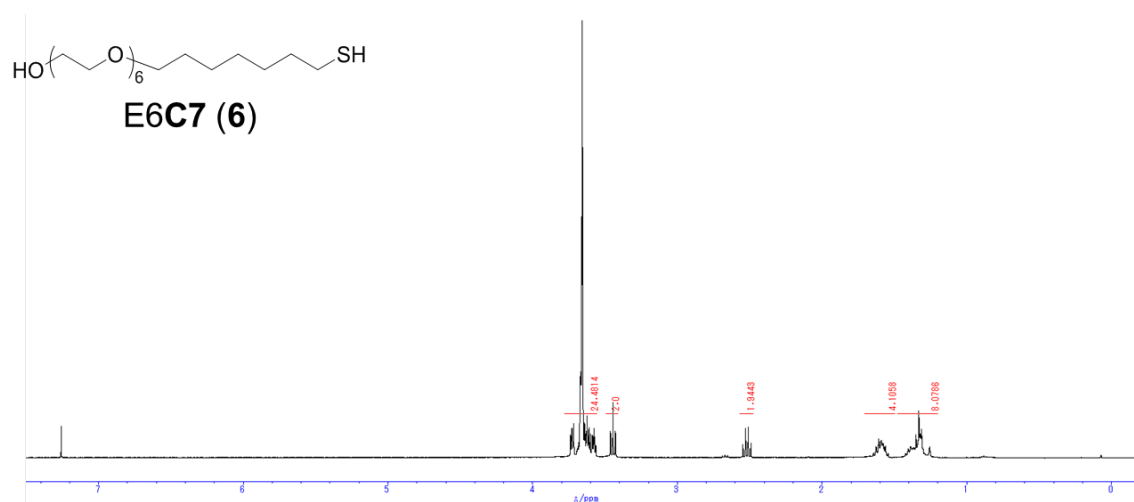


Figure 2-2. $^1\text{H NMR}$ spectrum of **E6C7**. Residual water signal was suppressed.

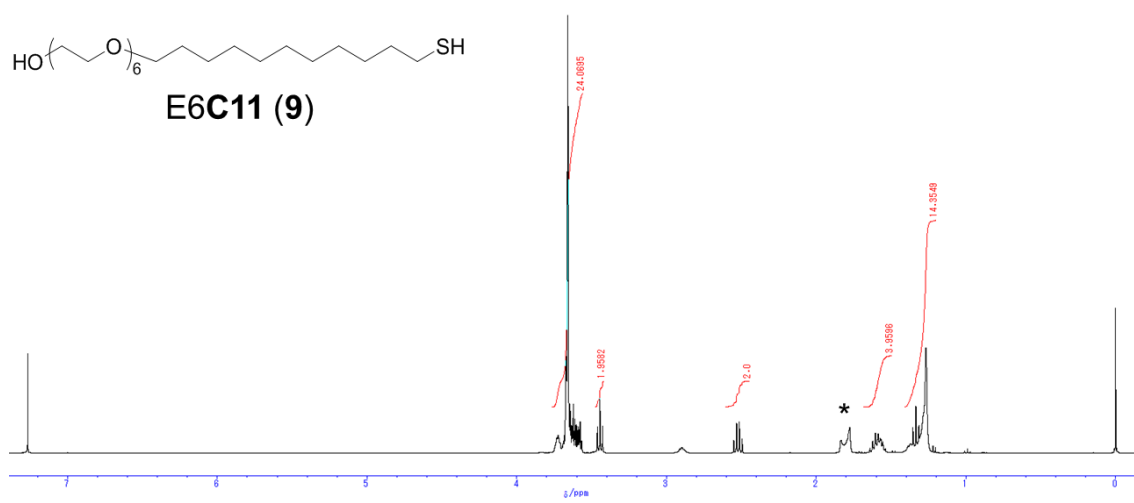


Figure 2-3. ¹H NMR spectrum of **E6C11**. * represents a signal derived from water.

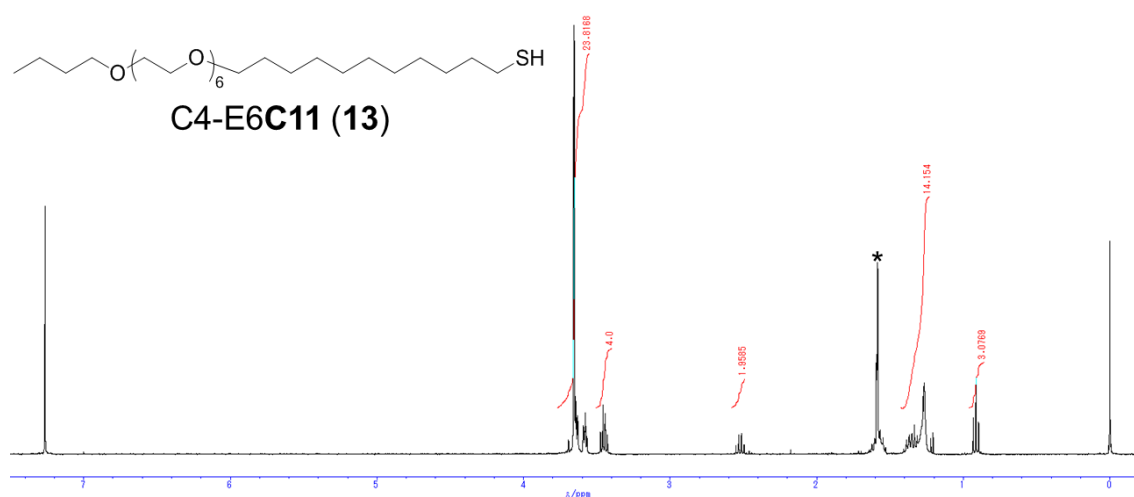


Figure 2-4. ¹H NMR spectrum of **C4-E6C11**. * represents a signal derived from water.

2-2-3. One-step or two-step ligand exchange reactions

Citrate-protected GNSs (1 mL, 60 nM) with a diameter of 5 nm were concentrated by centrifugation (x2, 10,000 g for 10 min) using an Amicon Ultra 100K filter (Merck MilliPore) to 3 μM (total 20 μL). For the one-step ligand exchange, the

concentrated GNSs were added to an aqueous solution of a mixture of the two ligands at desired ratios (total concentration of two ligands: 400 μM). In this exchange reaction, the total ligand concentration was adjusted to one equivalent each for Au atoms on the nanoparticle surface, assuming 642 Au atoms. After 24-hours incubation, the GNSs were purified by centrifugation (twice, 10,000 g for 10 min) and used for MALDI-TOF MS analysis. For the **E6C3/C4-E6C11** system, methanol was used as a solvent. In this case, the GNSs were purified by centrifugation (twice, 14,100 g for 60 min).

For the two-step ligand exchange reaction, citrate-protected GNSs were first added to an aqueous solution of **E6C3** ligand (400 μM , 100 μL). After 24-hours incubation, the GNSs were purified by centrifugation using an Amicon Ultra 100K filter (twice, 10,000 g for 10 min), and then redispersed in an aqueous solution of **E6C11** ligands (final concentration: 400 μM). After incubation for the desired numbers of hours (hourly up to six hours), the GNSs were purified by centrifugation (twice, 14,100 g for 5 min). In the case of the **E6C3/C4-E6C11** combination, methanol was used as a solvent and purified as above.

2-2-4. Preparation of Janus GNSs with hydrophilic/hydrophobic faces

The concentrated 5-nm citrate-protected GNSs (20 μL , 3 μM) were added to a methanol solution of **E6C3** (200 μM , 100 μL). After 24-hours incubation, the GNSs were purified by centrifugation (x2, 14,100 g for 60 min), and then redispersed in a methanoic solution of **C4-E6C11** (2 mM, 100 μL). After 5 hours, GNSs were purified by centrifugation (twice, 14,100 g for 60 min).

2-2-5. MALDI-TOF MS analysis of ligand-displaying GNSs

The concentrated thiol-modified GNSs were analyzed by MALDI-TOF MS in reflector mode. A solution of the GNSs (2 μL) was deposited on a stainless steel plate, then a matrix solution of 2,5-dihydroxybenzoic acid (10 mg/mL) was deposited on the spot of the GNSs and dried.

2-2-6. PCXSS experimental setup and analysis

For PCXSS measurement of the Janus GNS assemblies, the suspension placed in a microtube was sonicated for 5 min, and then let stand for about 1.5 hours. The suspension was then enclosed in a micro-liquid enclosure array (MLEA) chip to keep Janus GNS assembly in solution. I performed PCXSS experiments using the SPring-8 Angstrom Compact Free-Electron Laser (SACLA).²⁷ The X-ray free-electron laser (XFEL) pulses from the SACLA, with a photon energy of 4.0 keV and a pulse duration of ~ 10 fs, were coherently focused to a spot size of $1.5 \mu\text{m} \times 1.6 \mu\text{m}$.²⁸ The focused XFEL beam illuminated the sample in the MLEA that was contained in a Multiple Application X-ray Imaging Chamber.²⁹ Single-shot coherent X-ray diffraction (CXD) patterns were recorded with two multi-port charge-coupled device (MPCCD) detectors in a tandem arrangement:³⁰ an octal sensor (2048 x 2048 pixels) and a dual sensor (1024 x 1024 pixels) located 1.321 m and 2.862 m downstream from the sample, respectively. The octal sensor has an adjustable size aperture in the center, and the diffracted X-rays passing through the central aperture were captured by the dual sensor. Each pixel of the MPCCD detectors has a size of $50 \mu\text{m} \times 50 \mu\text{m}$.

Image reconstruction was performed for CXD patterns after centrosymmetrization and 6x6 pixel binning. The relaxed averaged alternating reflections

algorithm³¹ with shrink-wrap support³² (6,000 steps) and subsequently the noise-tolerant hybrid input-output algorithm³³ with fixed support (1,000 steps) were used. The feedback parameter β was set to 0.85 in the both algorithms. In the shrink-wrap method, the support was updated every 100 iterations, and the kernel was initially set to 5 pixels and was gradually reduced down to 3 pixels. Using results with 100 different initial random seeds, I calculated correlation coefficients²⁵ between all pairs of the results. Finally, 10 images with the highest similarity were selected and averaged.

2-3. Results and Discussion

2-3-1. Phase segregation of two ligands with different alkyl chains.

Three kinds of the hydrophilic ligands (**E6C3**, **E6C7**, **E6C11**) and one kind of the hydrophobic ligand (**C4-E6C11**) were synthesized according to the previous paper with some modifications (See chemical structures in Figure 2-5).³⁴ Here, the abbreviation, **E6**, represents the hexaethylene glycol moiety.

The ratio and degree of segregation of the surface ligands on the GNSs were analyzed by MALDI-TOF MS according to Cliffel's method (Figure 2-6).¹⁹ Au_4L_4 ion species as gold-thiolate complexes (L represents a thiolate ligand) are desorbed from a GNS surface coated with thiolate ligands by MALDI process. When the GNSs are coated with two kinds of ligand (L and L'), five kinds of gold-thiolate complexes [$\text{Au}_4\text{L}_x\text{L}'_{4-x}$ ($x=0-4$)] desorbed from the surface. The immobilization ratio of the two ligands on GNSs can be determined by the relative intensities of these five peaks. In addition to information on immobilization ratio, the distribution of the two ligands can be obtained from the intensity pattern of the five peaks in the MALDI-TOF mass spectrum. The degree of phase segregation can be estimated from the value of the residual sum of squares (r), which is calculated from the measurement of deviation from the binomial mode. When two ligands are segregated into a Janus-type pattern on GNSs, the residual value, r , is reported to be above 0.1.³⁸ In this paper, the qualitative assessment of the r value for Janus segregation is set at 0.1 and I hereafter refer to GNSs with an r value of 0.1 or greater as "Janus-like GNSs". Further, considering the synthetic method by which homogeneous ligand exchange occurred, it is possible that not all GNSs are "Janus-like GNS", although GNSs having more than two hydrophobic domains would be included. On the other hand, the r value less than 0.01 is thought to a minimal degree of phase segregation, and the r

value between 0.1 and 0.01 were thought to form some small domains, but not a completely random distribution.

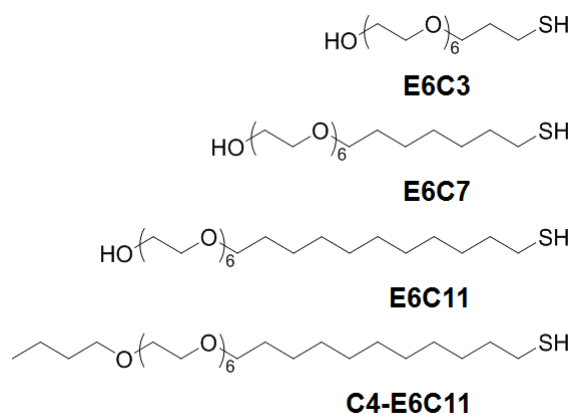


Figure 2-5. Chemical structures of the thiolate ligands with different alkyl chain lengths used in this work.

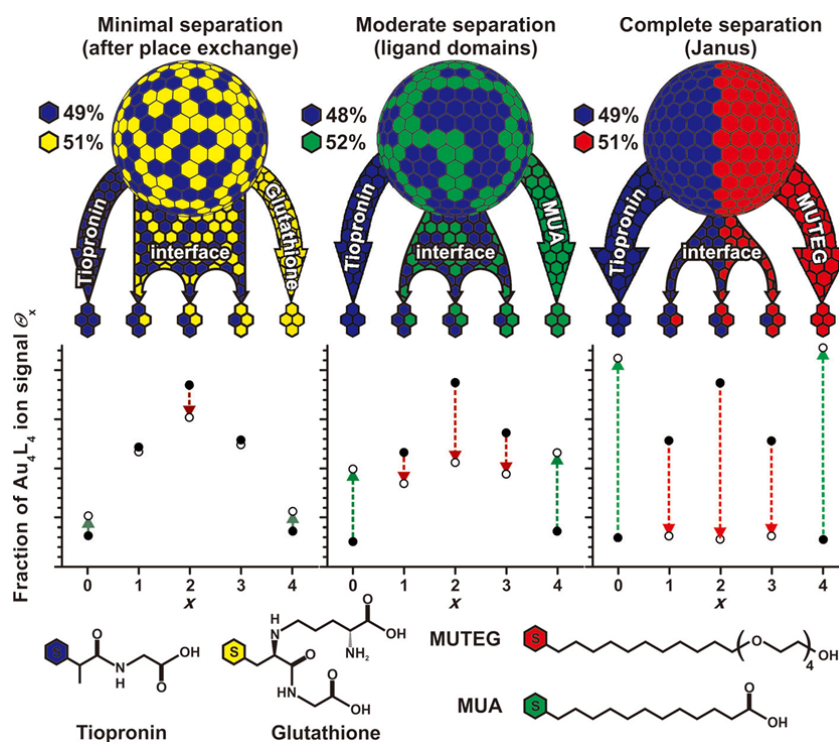


Figure 2-6. Schematic illustration of analysis of the ratio and degree of segregation of the surface ligands on the GNSs by MALDI-TOF MS from ref 19. ● shows deviation from the theoretical model, and ○ shows experimental distributions for $\text{Au}_4\text{L}_x\text{L}'_{4-x}$ ($x=0-4$).

- **Immobilized ratio and phase segregation of E6C3/E6C11 on 5-nm GNSs**

E6C3 and **E6C11** ligands were simultaneously added to an aqueous solution of 5-nm GNSs and left to stand for 24 hours in water, hereafter referred to as the one-step approach (Figure 2-7a, b, and e). Figure 2-7a shows two sets of 5 peaks for the gold-ligand tetramers as sodium or potassium adducted ions ($[\text{Au}_4\text{-L}_4\text{+Na}]^+$ and $[\text{Au}_4\text{-L}_4\text{+K}]^+$). In Figure 2-7b, the immobilization ratio on GNSs was plotted as a function of the mixture ratio in solution. The ratio of **E6C11** immobilized on GNSs was found to be greater than the mixture ratio in solution. This indicates that **E6C11** ligands preferably associate with the GNS surface due to strong interactions between the long alkyl chains. The immobilization ratio could be controlled by changing the ratio of the mixture of the two ligands applied in the one-step approach as plotted in Figure 2-7b. The r values for GNSs displaying two ligands at a ratio of almost 1:1 ratio via one-step addition was 0.04 (\pm 0.029), indicating some small domains. In the previous study on the self-assembly of thiolate alkyl compounds with different alkyl chain lengths on a flat surface, it was found that the thiolate alkyl with a long alkyl chain formed domains in the monolayer of ligands with the shorter alkyl chain.^{20,21}

Next, I examined the two-step addition of **E6C3** and **E6C11** to the GNS solution (Figure 2-7c, d, and e). First, GNSs were incubated with **E6C3** (1 equiv. for Au number on the GNS surface) in water and purified by centrifugation to produce **E6C3**-GNSs. Then, **E6C11** ligands were added to the **E6C3**-GNSs aqueous solution, incubated for 5 hours and subjected to MALDI-TOF MS analysis. This two-step approach yielded a peak pattern that differs from that observed for the one-step approach (Figure 2-7c). The two peaks of $\text{Au}_4(\text{E6C3})_4$ and $\text{Au}_4(\text{E6C11})_4$ were relatively higher than those of the other peaks. In the two-step approach, the immobilization ratio could be controlled by adjusting

the incubation time of **E6C11** (Figure 2-7d). The incubation of the **E6C3**-GNSs in an aqueous solution with **E6C11** for 4 hours produced an **E6C11** immobilization ratio of almost 50%. The r values for GNSs displaying two ligands at a ratio of almost 1:1 ratio via two-step addition was 0.13 ± 0.066 , indicating that Janus-like GNSs formed. When I changed the order of the ligand addition to GNSs from **E6C11**-GNSs to **E6C3**, very little ligand exchange was observed. This indicates that the ligand with a long alkyl chain provides a stable monolayer on the GNSs, suppressing ligand exchange to the ligand with a short (C3) alkyl chain. Similarly, it has been reported that it was difficult to exchange ligands from a surface ligand with a long alkyl chain to a short-chained ligand.³⁵

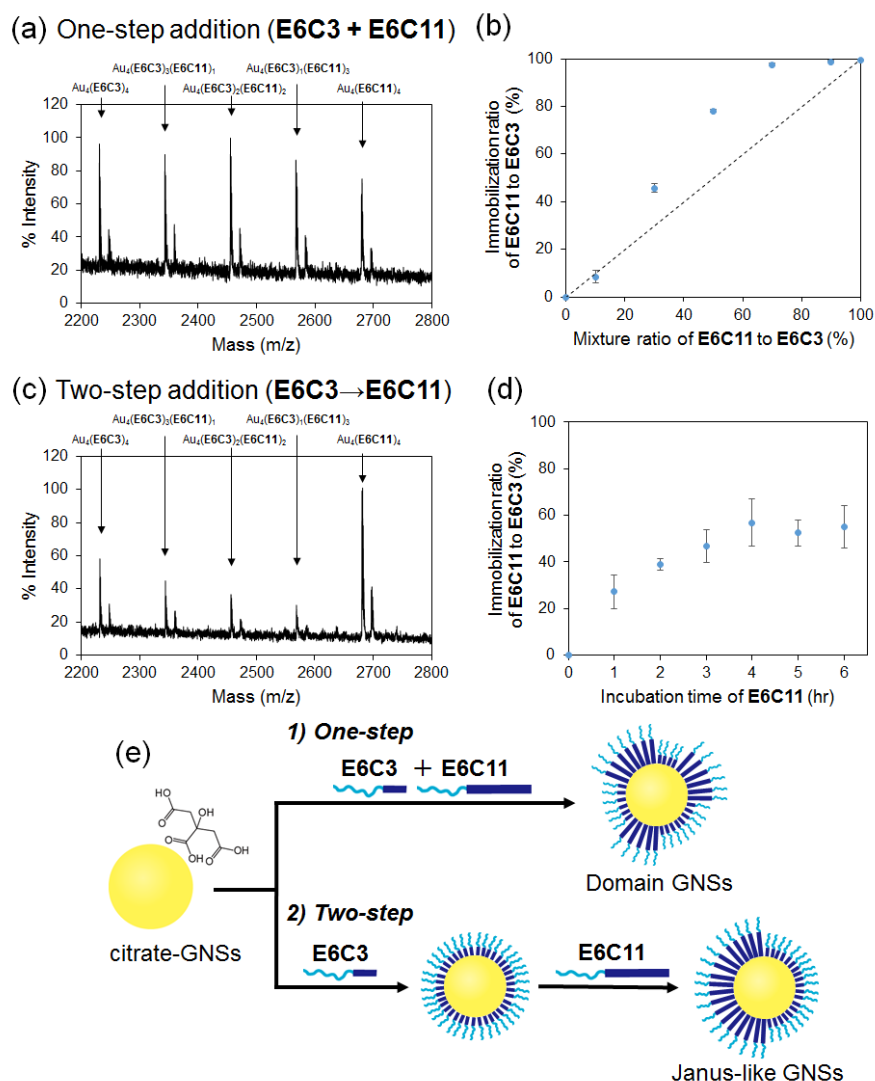


Figure 2-7. (a, b) Ratio of two ligands on GNSs obtained by ligand exchange reaction using the one-step addition of **E6C3** and **E6C11** in water. (a) Typical MALDI-TOF mass spectrum of Au-ligand complexes, (b) the ratio of **E6C11** on GNSs as a function of the ratio in a solution before the reaction. The result shows that the immobilization ratio can be controlled by adjusting the mixture ratio of the two ligands. (c, d) Ligand distributions on GNSs in the two-step ligand exchange reaction with **E6C3** and **E6C11** in water. (a) Typical MALDI-TOF mass spectrum of Au-ligand complexes of **E6C3/E6C11** GNPs formed by adding **E6C11** (10 equiv for Au number on the GNP surface) to **E6C3**-GNPs (**E6C3:E6C11**=43:57). (b) Dependency of the immobilization ratio of **E6C11** on the incubation time of **E6C11**. The result shows that the immobilization ratio can be controlled by adjusting the incubation time. Error bar represents SD ($n = 3$). (e) The schematic illustration of the degree of the phase segregation via one-step and two-step addition.

The r values for GNSs displaying two ligands at a ratio of almost 1:1 ratio are summarized in Table 2-1. A large r value means a greater degree of phase segregation of surface ligands on the GNSs. The r values obtained from the two-step approach were larger than those obtained from the one-step addition, showing that the two-step approach is more effective in inducing **E6C11** segregation. The r values were almost constant at 0.1 for the immobilization ratios of **E6C11** between 25% and 60% in the two-step approach. This result indicates that the two-step addition is advantageous in the formation of Janus-like GNSs with a controlled surface area consisting of the two ligands. For one-step approach, based on the r value of 4.9×10^{-2} , the ligands were thought to form some small domains, but not forming completely random distribution. Thereby, hereafter, I describe the GNSs with r value between 0.1 and 0.01 as Domain GNSs.

As alkyl-packing between C11 chains is much stronger than that between C3 and C11 chains, the growth of the C11 domain at the second step was preferred to the random distribution of C11 in the C3 layer. Weinstock *et al.* reported that nucleation and subsequent island growth process are involved in the domain formation process upon ligand exchange reaction.³⁶ Similarly, the data suggests the **E6C11** phase is grown in the **E6C3** monolayer on the GNSs to generate Janus-like **E6C3/E6C11** GNSs under an appropriate concentration of **E6C11**. When two-step ligand exchange from **E6C3** to **E6C11** was carried out in methanol, the r value (1.1×10^{-2}) was significantly decreased compared to that in water ($r = 13 \times 10^{-2}$, Table 2-1). This indicates that the island growth process of **E6C11** was inhibited in methanol as the hydrophobic interaction between **E6C11** molecules are weakened in an organic solvent. Thermodynamic stability of the ligand segregation was then tested using Domain **E6C3/E6C11** GNSs. The MALDI-TOF signal pattern from **E6C3/E6C11** GNSs were unchanged after incubation in water at 50°C

for 24 hours (Figure 2-8). This indicates that little ligand transfer on the GNS surface occurs. Cliffler *et al.* reported a similar observation of no transfer of ligand molecules on GNSs.¹⁹

Table 2-1. Effects of ligand combination as well as solvent and mixing procedure on phase segregation (*r* value). GNSs coated with two ligands were categorized into three types. GNSs with *r*-values of more than 0.1, between 0.1 and 0.01, less than 0.01 were referred to as Janus, Domain and Random GNSs, respectively.

combination	solvent	procedure	Immobilization ratio (%) (*RC11)	<i>r</i> value ($/10^{-2}$)	degree of phase segregation
E6C3+E6C11	water	one-step	46 ± 1.9	4.0 ± 2.9	Domain
		two-step	52 ± 5.5	13 ± 6.6	Janus
	MeOH	one-step	55	0.83	Random
		two-step	53	1.1	Domain
E6C7+E6C11	water	one-step	51 ± 0.61	0.96 ± 0.51	Domain or Random
		two-step	48 ± 0.4	3.2 ± 0.47	Domain
E6C3+C4-E6C11	MeOH	one-step	45 ± 3.3	4.0 ± 1.3	Domain
		two-step	55 ± 4.8	22 ± 11	Janus

*R = E6 or C4-E6

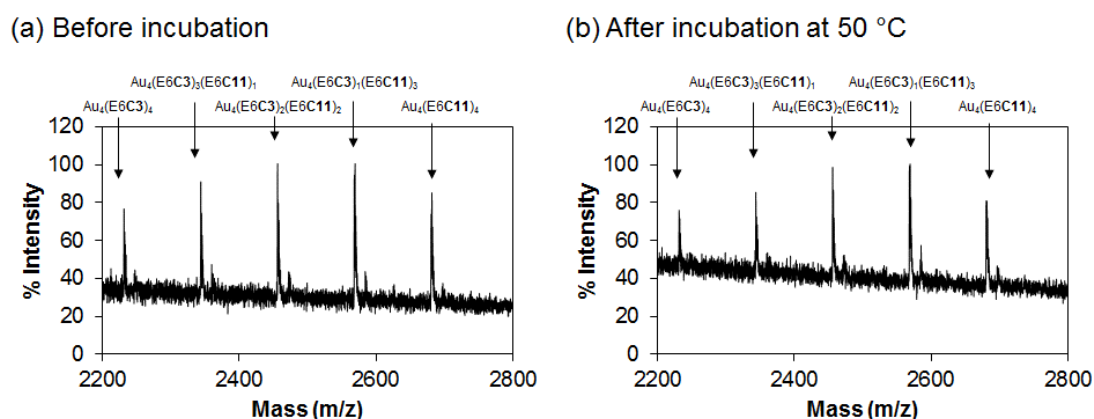


Figure 2-8. A comparison of the MALDI-TOF mass spectra of Au-ligand complexes of **E6C3/E6C11** GNPs (a) before and (b) after incubation in water at 50°C for 1 day. From these patterns, the immobilization ratios of **E6C3:E6C11** are (a) 47:53 and (b) 45:55, respectively. The *r* values are (a) 0.046 and (b) 0.037, respectively. This means that the degree of segregation degree formed by the two ligands on the GNPs remained for 1 day.

- **Phase segregation of E6C7 and E6C11 on 5-nm GNSs**

The above trend for the two-step approach was also observed for the combination of **E6C7** and **E6C11**, suggesting the general induction of a greater degree of segregation by the two-step approach (Table 2-1). However, the r values for **E6C7/E6C11** were smaller than those for **E6C3/E6C11**, indicating that **E6C11** ligands were relatively less segregated in the **E6C7** layer due to the similarity in alkyl chain length between C7 and C11. The combination of **E6C7** and **E6C11** yielded an r value of 3.2×10^{-2} , indicating the formation of partial domains but not Janus-like segregation. These data reveal that for Janus-like nanoparticles, a large difference in alkyl length, as shown in the combination of C3 and C11, is necessary *via* the two-step approach.

- **Size effect on phase segregation (E6C3/E6C11)**

I next investigated the effect of GNS size on the degree of phase separation. The r value of GNSs with diameters of 10 and 15 nm modified with the **E6C3/E6C11** system using the two-step method were 3.5×10^{-2} and 3.4×10^{-2} , respectively (Figure 2-9). These values are much smaller than that observed for 5-nm GNSs, indicating that increases in the size of the GNSs lead to decreases in the degree of phase segregation, and 5 nm being the maximum limit for Janus-like GNSs, even when using the two-step method. Glotzer *et al.* reported that the domain morphology made by two surface ligands of different molecular lengths depends on the particle size. Smaller particles tend to produce Janus-type phase separation.^{18,37} The data support the notion that smaller particles favor the Janus-type phase separation of two surface ligands even for the two-step approach.

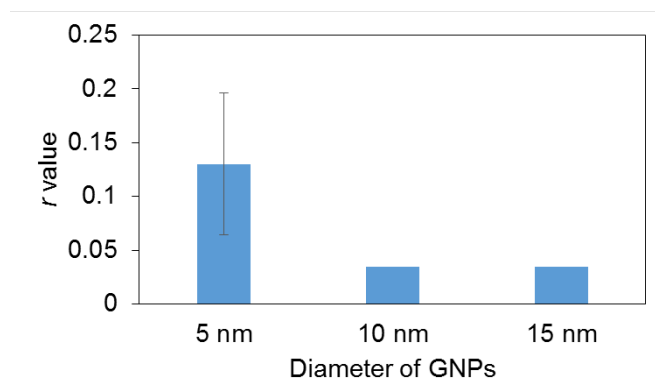


Figure 2-9. Effect of GNS diameter on the **E6C3/E6C11** phase segregation (r values) using the two-step approach. The 5-nm GNSs provided the larger phase segregation compared to 10- and 15-nm GNSs. Error bar for 5-nm GNSs represents SD ($n = 3$).

2-3-2. Synthesis of Janus GNSs with hydrophilic/hydrophobic faces

The two-step approach using **E6C3** and **E6C11** afforded a large degree of segregation on the GNSs; however, the nanoparticle surface remains hydrophilic due to both ligands having the same E6 terminus. In order to make Janus nanoparticles with hydrophilic/hydrophobic faces, I prepared a butyl-headed ligand, **C4-E6C11** (Scheme 2-1), in which the E6 segment was capped with a C4 alkyl chain. When coating GNSs with **E6C3** and **C4-E6C11** in both the one-step and two-step processes, methanol was used as a solvent because of the low solubility of **C4-E6C11** in water. Figure 2-10 shows the MALDI-TOF mass spectra of GNSs made using the one-step and two-step approach with **E6C3** and **C4-E6C11**. For the one-step addition, a ratio of **E6C3** to **C4-E6C11** of 53:47 (nearly 50:50) was obtained on the GNS surface by using a mixture ratio of 30:70 in solution before reaction. The one-step addition of **E6C3/C4-E6C11** to GNSs resulted in formation of some domains of the two ligands with r value of 4.0×10^{-2} (Figure 2-10a). For the two-step addition, the ratio of two ligands on the surface was significantly dependent on the concentration of the subsequently added **C4-E6C11**. Therefore, I adjusted the ligand ratio to 44:56, which is nearly 50%, by adding 5 equivalent of **C4-E6C11** (2 mM) to the surface Au atoms for the two-step addition. For the two-step approach, two strong signals for $\text{Au}_4(\text{E6C3})_4$ and $\text{Au}_4(\text{C4-E6C11})_4$ were observed (Figure 2-10b), and the r value was 22×10^{-2} . This indicates that the two-step approach afforded Janus-like GNSs in which the **C4-E6C11** and **E6C3** regions were largely segregated. Figure 2-11 shows the r values for the combinations of **E6C3/E6C11** in methanol and water, and **E6C3/C4-E6C11** in methanol (see also Table 2-1). As discussed in the previous section, the two-step approach “in water” using the **E6C3/E6C11** produced Janus-like GNSs. However, “in methanol”, even the two-step approach failed

to produce Janus-like GNSs, but nearly Random GNSs. Interestingly, for the **E6C3/C4-E6C11** combination, the two-step approach in methanol clearly provided a larger r value (22×10^{-2}) than that produced in the one-step approach. This large difference in r values observed between **E6C3/E6C11** and **E6C3/C4-E6C11** in the two-step approach indicates that a short C4 alkyl head is effective in promoting island growth of **C4-E6C11** even in methanol due to their hydrophobic interaction.

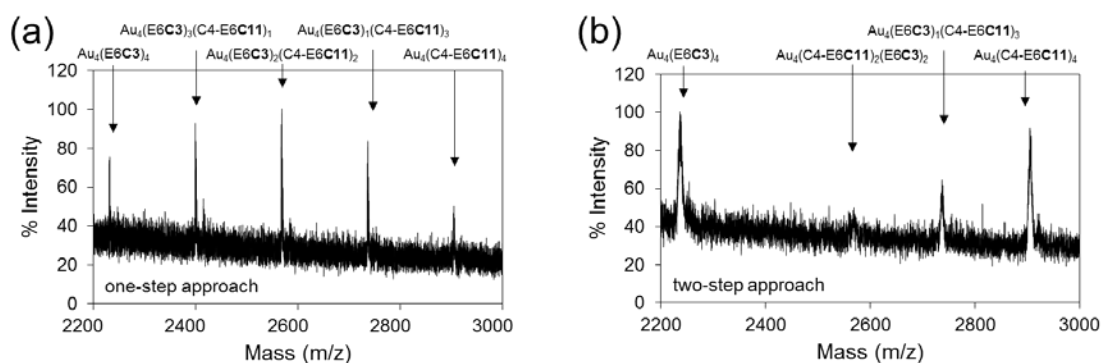


Figure 2-10. A comparison of MALDI-TOF mass spectra of Au-ligand complexes for the (a) one-step and (b) two-step ligand exchange of **E6C3** and **C4-E6C11**. The immobilized ratios of **E6C3**:**C4-E6C11** on the GNSs are 53:47 and 44:56, respectively. The two strong signals for $\text{Au}_4(\text{E6C3})_4$ and $\text{Au}_4(\text{C4-E6C11})_4$ observed in the two-step approach indicate the formation of Janus-like GNSs.

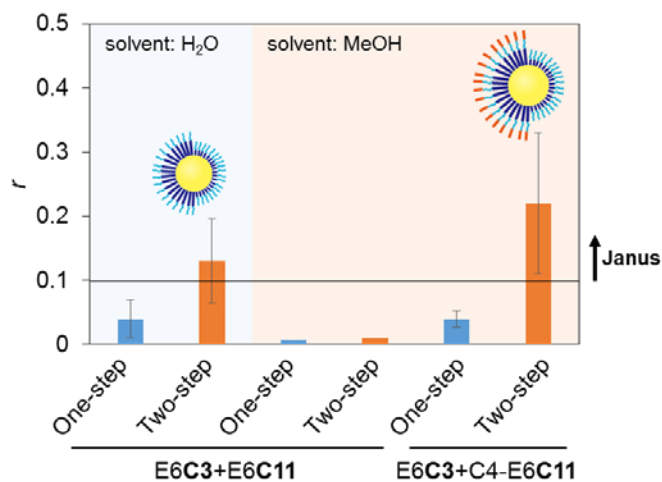


Figure 2-11. A Comparison of r values for the combinations of **E6C3/E6C11** and **E6C3/C4-E6C11**. Detailed r values and immobilization ratios of the two ligands are shown in Table 1. For **E6C3**+**C4-E6C11**, short C4 alkyl head assisted the successful formation of Janus-like GNSs even in methanol. Error bar represents SD ($n = 3$).

2-3-3. Differences in self-assembly behavior in water between Domain and Janus-like GNSs

The dispersity of **E6C3/C4-E6C11** (ratio was adjusted to nearly 50:50)-coated Janus-like and Domain GNSs in water was next compared. The solvent was removed from the methanoic solutions of GNSs by centrifugation and the GNSs were resuspended in water. Domain GNSs, synthesized by one-step approach, were well-dispersed in methanol; however, they were precipitated in water after 12 hours (Figure 2-12a). Janus-like GNSs, synthesized by two-step approach, remained dispersed in water for 12 hours although some precipitation was observed, and formed an assembled structure in water with an average size of 160 ± 50 nm after 2 hours (Figure 2-12b). Dynamic light scattering (DLS) measurement revealed that the Domain and Janus-like GNSs were monodispersed in methanol (Figure 2-12c, d). Bianchi *et al.* reported the gas-liquid phase separation using the spot-like patch model and the decreasing the patch number on a surface leads to the suppression of gas-liquid phase separation.³⁸ Based on this model, the observation that Domain GNSs were more easily precipitated compared to Janus-like GNSs (Figure 2-12a) appears reasonable, as Domain GNSs have a larger patch number than do Janus-like GNSs.

STEM observations indicate that Janus-like GNSs formed spherical aggregation (Figure 2-13). The diameter of the assemblies was around 200-800 nm, and this size was larger than that obtained from DLS analysis, probably due to a decrease in the height of the assemblies in the drying process. To observe the structure of the nanoparticle assemblies in water, the PCXSS method using X-ray laser diffraction was applied, which is expected to provide high-resolution imaging of samples in solution without causing radiation damage. The CXD patterns of the assemblies was obtained and images were

reconstructed according to the reported procedure (Figure 2-14). The CXD signal from the Janus-like GNS in Figure 2-14a extends up to a spatial frequency of $1/(15 \text{ nm})$ as determined with a signal threshold of 2.3 photons per 6x6 detector pixels, which is 3 times as large as the standard deviation of background noise. The full-period spatial resolution of Figure 2-14b is estimated to be 23 nm from the phase retrieval transfer function.³⁹

The average diameter of the assemblies was found to be around 150 nm, which agrees with the DLS data. Typical image shown in Figure 9b reveals that Janus-like GNSs are self-assembled into spherical structures with uneven surfaces. The self-assembly of amphiphilic Janus-like particles into a worm-like string has been predicted by simulation studies and, in fact, string assemblies have been experimentally demonstrated for Janus particles.^{8,40}

For Janus-like GNSs consisting of **E6C3/C4-E6C11** ligands, neither TEM nor PCXSS images support the specific formation of such string- or worm-like structures. Instead, images indicated the spherical aggregation of GNSs, suggesting that the Janus-like GNSs can be dispersed in water by exposure of the hydrophilic face. However, micelle- or vesicle-like structures were not observed, and the interior of the assembly was packed. This suggests that a part of Janus-like GNSs behave as patchy particles, which have several attractive sites on the surface rather than the assembly of perfect Janus particles.

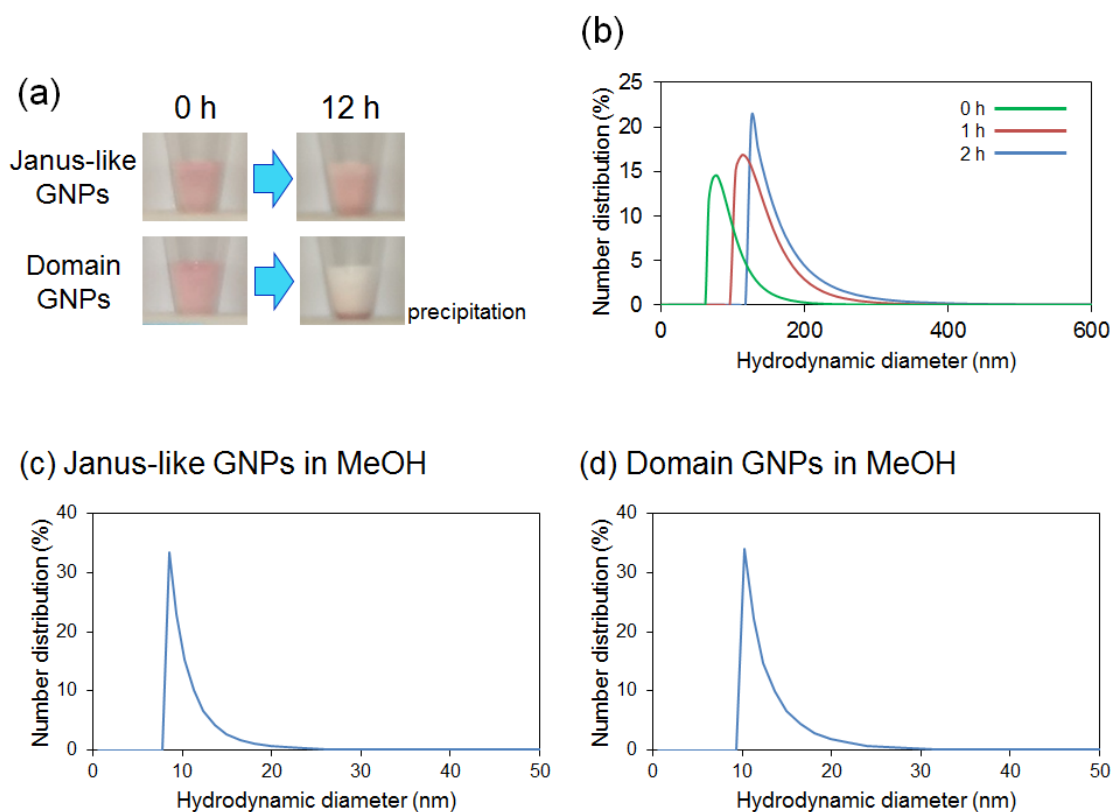


Figure 2-12. (a) Pictures of solutions of Janus-like GNSs and Domain GNSs in water. (b) Dynamic light scattering analysis of Janus-like GNSs in water. Domain GNSs were precipitated faster than Janus-like GNSs. (c, d) Dynamic light scattering analysis of (c) Janus-like GNPs and (d) Domain GNPs in methanol. GNPs display both **E6C3** and **C4-E6C11**

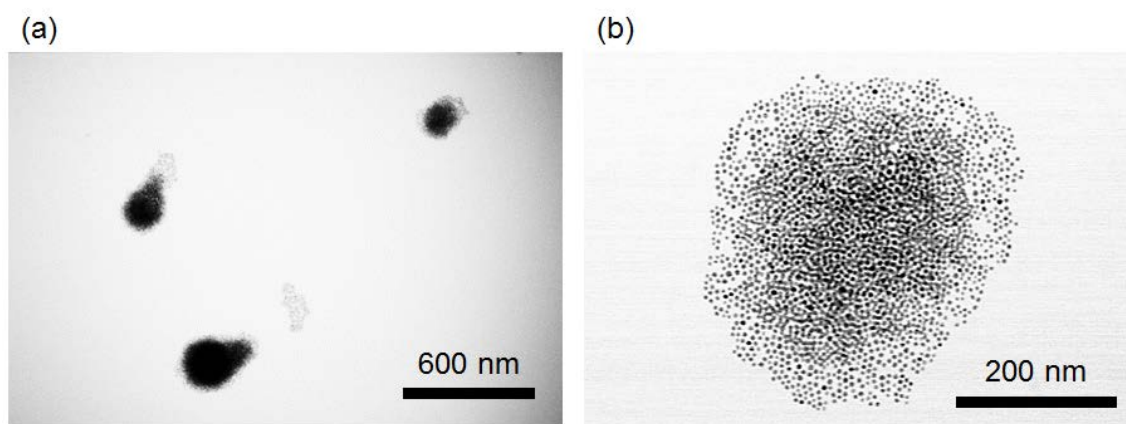


Figure 2-13. STEM images of a Janus-like GNS assembly.

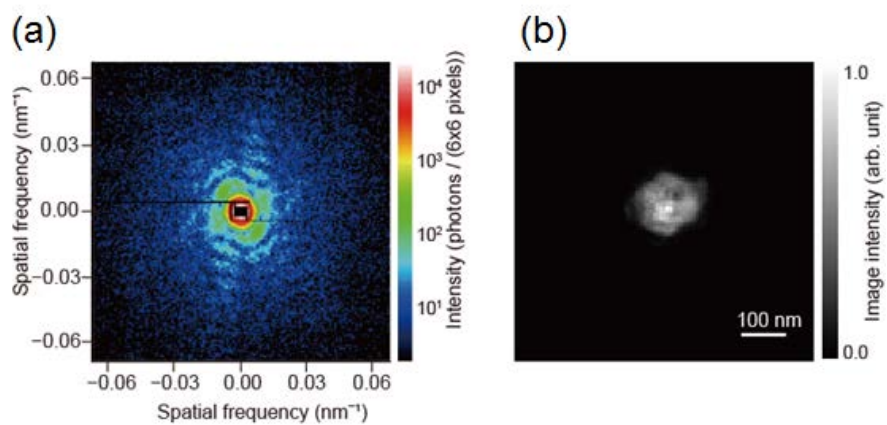


Figure 2-14. Experimental CXD pattern of (a) a Janus-like GNS assembly in water, and (b) the reconstructed image.

2-4. Conclusion

Janus-like GNSs with hydrophobic and hydrophilic faces were successfully synthesized by a two-step approach using two ligands with alkyl chains of different lengths. The segregation degree of the two ligands on the GNSs was estimated using MALDI-TOF MS analysis based on Cliffler's method. In the case of the one-step approach, it was found that the segregation degree was much smaller than that formed by the two-step approach. By two-step approach, the large phase segregation was achieved for GNSs large as 5 nm. From the view point of ligand design, there are two factors necessary to yield a large degree of segregation; the first, and most important, is a large difference in the length of the thiolated alkyl chains of the two ligands. The other is the presence of an alkyl head (the C4 moiety) on a hydrophobic ligand (**C4-E6C11**) to assist in the formation of the domain through hydrophobic interactions between the ligand heads. Interestingly, I found that the assemblies of Janus-like GNSs with hydrophilic/hydrophobic faces were more stably dispersed in water than were Domain GNSs, which are easily precipitated. PCXSS using X-ray laser diffraction provided an image of each assembly and showed that Janus-like GNSs assembled into an irregular spherical structure with an uneven surface.

2-5. References

- (1) Zhang, Z.; Glotzer, S. C. Self-Assembly of Patchy Particles. *Nano Lett.* **2004**, *4*, 1407–1413.
- (2) Gröschel, A. H.; Walther, A.; Löbbling, T. I.; Schacher, F. H.; Schmalz, H.; Müller, A. H. E. Guided Hierarchical Co-Assembly of Soft Patchy Nanoparticles. *Nature* **2013**, *503*, 247–251.
- (3) Rycenga, M.; McLellan, J. M.; Xia, Y. Controlling the Assembly of Silver Nanocubes through Selective Functionalization of Their Faces. *Adv. Mater.* **2008**, *20*, 2416–2420.
- (4) Zubarev, E. R.; Xu, J.; Sayyad, A.; Gibson, J. D. Amphiphilicity-Driven Organization of Nanoparticles into Discrete Assemblies. *J. Am. Chem. Soc.* **2006**, *128*, 15098–15099.
- (5) Wang, Y.; Wang, Y.; Breed, D. R.; Manoharan, V. N.; Feng, L.; Hollingsworth, A. D.; Weck, M.; Pine, D. J. Colloids with Valence and Specific Directional Bonding. *Nature* **2012**, *490*, 51–55.
- (6) Romano, F.; Sciortino, F. Two Dimensional Assembly of Triblock Janus Particles into Crystal Phases in the Two Bond per Patch Limit. *Soft Matter* **2011**, *7*, 5799.
- (7) Jiang, S.; Chen, Q.; Tripathy, M.; Luijten, E.; Schweizer, K. S.; Granick, S. Janus Particle Synthesis and Assembly. *Adv. Funct. Mater.* **2010**, *22*, 1060–1071.
- (8) Hong, L.; Cacciuto, A.; Luijten, E.; Granick, S. Clusters of Amphiphilic Colloidal Spheres. *Langmuir* **2008**, *24*, 621–625.
- (9) Xu, Q.; Kang, X.; Bogomolni, R. A.; Chen, S. Controlled Assembly of Janus Nanoparticles. *Langmuir* **2010**, *26*, 14923–14928.
- (10) Wang, B.; Li, B.; Dong, B.; Zhao, B.; Li, C. Y. Homo- and Hetero-Particle Clusters Formed by Janus Nanoparticles with Bicompartiment Polymer Brushes. *Macromolecules* **2010**, *43*, 9234–9238.
- (11) Personick, M. L.; Mirkin, C. A. Making Sense of the Mayhem behind Shape Control in the Synthesis of Gold Nanoparticles. *J. Am. Chem. Soc.* **2013**, *135*,

- 18238–18247.
- (12) Sau, T. K.; Murphy, C. J. Room Temperature , High-Yield Synthesis of Multiple Shapes of Gold Nanoparticles in Aqueous Solution. *J. Am. Chem. Soc.* **2004**, *126*, 8648–8649.
 - (13) Daniel, M. C. M.; Astruc, D. Gold Nanoparticles: Assembly, Supramolecular Chemistry, Quantum-Size Related Properties and Applications toward Biology, Catalysis and Nanotechnology. *Chem. Rev.* **2004**, *104*, 293–346.
 - (14) Andala, D.; Shin, S.; Lee, H.; Bishop, K. Templated Synthesis of Amphiphilic Nanoparticles at the Liquid–Liquid Interface. *ACS Nano* **2012**, No. 2, 1044–1050.
 - (15) Wang, B.; Li, B.; Zhao, B.; Li, C. Y. Amphiphilic Janus Gold Nanoparticles via Combining “Solid-State Grafting-To” and “Grafting-From” Methods. *J. Am. Chem. Soc.* **2008**, *130*, 11594–11595.
 - (16) Pradhan, S.; Xu, L. P.; Chen, S. Janus Nanoparticles by Interfacial Engineering. *Adv. Funct. Mater.* **2007**, *17*, 2385–2392.
 - (17) Lee, H. Y.; Shin, S. H. R.; Abezgauz, L. L.; Lewis, S. A.; Chirsan, A. M.; Danino, D. D.; Bishop, K. J. M. Integration of Gold Nanoparticles into Bilayer Structures via Adaptive Surface Chemistry. *J. Am. Chem. Soc.* **2013**, *135*, 5950–5953.
 - (18) Kim, H.; Carney, R. P.; Reguera, J.; Ong, Q. K.; Liu, X.; Stellacci, F. Synthesis and Characterization of Janus Gold Nanoparticles. *Adv. Mater.* **2012**, *24*, 3857–3863.
 - (19) Harkness, K. M.; Balinski, A.; McLean, J. A.; Cliffler, D. E. Nanoscale Phase Segregation of Mixed Thiolates on Gold Nanoparticles. *Angew. Chem. Int. Ed.* **2011**, *50*, 10554–10559.
 - (20) Bain, C. D.; Whitesides, G. M. Formation of Monolayers by the Coadsorption of Thiols on Gold: Variation in the Head Group, Tail Group, and Solvent. *J. Am. Chem. Soc.* **1989**, *111*, 7155–7164.
 - (21) Tamada, K.; Hara, M.; Sasabe, H.; Knoll, W. Surface Phase Behavior of N-

- Alkanethiol Self-Assembled Monolayers Adsorbed on Au(111): An Atomic Force Microscope Study. *Langmuir* **1997**, *7463*, 1558–1566.
- (22) Chapman, H. N.; Barty, A.; Bogan, M. J.; Boutet, S.; Frank, M.; Hau-Riege, S. P.; Marchesini, S.; Woods, B. W.; Bajt, S.; Benner, W. H.; London, R. A.; Plonjes, E.; Kuhlmann, M.; Treusch, R.; Dusterer, S.; Tschentscher, T.; Schneider, J. R.; Spiller, E.; Moller, T.; Bostedt, C.; Hoener, M.; Shapiro, D. A.; Hodgson, K. O.; van der Spoel, D.; Burmeister, F.; Bergh, M.; Caleman, C.; Hultdt, G.; Seibert, M. M.; Maia, F. R. N. C.; Lee, R. W.; Szoke, A.; Timneanu, N.; Hajdu, J. Femtosecond Diffractive Imaging with a Soft-X-Ray Free-Electron Laser. *Nat. Phys.* **2006**, *2*, 839–843.
- (23) Neutze, R.; Wouts, R.; van der Spoel, D.; Weckert, E.; Hajdu, J. Potential for Biomolecular Imaging with Femtosecond X-Ray Pulses. *Nature* **2000**, *406*, 752–757.
- (24) Chapman, H. N.; Fromme, P.; Barty, A.; White, T. A.; Kirian, R. A.; Aquila, A.; Hunter, M. S.; Schulz, J.; DePonte, D. P.; Weierstall, U.; Doak, R. B.; Maia, F. R. N. C.; Spence, J. C. H. et al. Femtosecond X-Ray Protein Nanocrystallography. *Nature* **2011**, *470*, 73–77.
- (25) Kimura, T.; Joti, Y.; Shibuya, A.; Song, C.; Kim, S.; Tono, K.; Yabashi, M.; Tamakoshi, M.; Moriya, T.; Oshima, T.; Ishikawa, T.; Bessho, Y.; Nishino, Y. Imaging Live Cell in Micro-Liquid Enclosure by X-Ray Laser Diffraction. *Nat. Commun.* **2014**, *5*, 3052.
- (26) Pérez, J.; Nishino, Y. Advances in X-Ray Scattering: From Solution SAXS to Achievements with Coherent Beams. *Curr. Opin. Struct. Biol.* **2012**, *22*, 670–678.
- (27) Ishikawa, T.; Aoyagi, H.; Asaka, T.; Asano, Y.; Azumi, N.; Bizen, T.; Ego, H.; Fukami, K.; Fukui, T.; Furukawa, Y.; Goto, S.; Hanaki, H.; Kumagai, N. et al. A Compact X-Ray Free-Electron Laser Emitting in the Sub-Ångström Region. *Nat. Photonics* **2012**, *6*, 540–544.
- (28) Yumoto, H.; Mimura, H.; Koyama, T.; Matsuyama, S.; Tono, K.; Togashi, T.; Inubushi, Y.; Sato, T.; Tanaka, T.; Kimura, T.; Yokoyama, H.; Kim, J.; Sano, Y.; Hachisu, Y.; Yabashi, M.; Ohashi, H.; Ohmori, H.; Ishikawa, T.; Yamauchi, K.

- Focusing of X-Ray Free-Electron Laser Pulses with Reflective Optics. *Nat. Photonics* **2012**, *7*, 43–47.
- (29) Song, C.; Tono, K.; Park, J.; Ebisu, T.; Kim, S.; Shimada, H.; Kim, S.; Gallagher-Jones, M.; Nam, D.; Sato, T.; Togashi, T.; Ogawa, K.; Joti, Y.; Kameshima, T.; Ono, S.; Hatsui, T.; Iwata, S.; Yabashi, M.; Ishikawa, T. Multiple Application X-Ray Imaging Chamber for Single-Shot Diffraction Experiments with Femtosecond X-Ray Laser Pulses. *J. Appl. Crystallogr.* **2014**, *47*, 188–197.
- (30) Kameshima, T.; Ono, S.; Kudo, T.; Ozaki, K.; Kirihara, Y.; Kobayashi, K.; Inubushi, Y.; Yabashi, M.; Horigome, T.; Holland, A.; Holland, K.; Burt, D.; Murao, H.; Hatsui, T. Development of an X-Ray Pixel Detector with Multi-Port Charge-Coupled Device for X-Ray Free-Electron Laser Experiments. *Rev. Sci. Instrum.* **2014**, *85*, 33110.
- (31) Luke, D. R. Relaxed Averaged Alternating Reflections for Diffraction Imaging. *Inverse Probl.* **2005**, *21*, 37–50.
- (32) Marchesini, S.; He, H.; Chapman, H. N.; Hau-Riege, S. P.; Noy, A.; Howells, M. R.; Weierstall, U.; Spence, J. C. H. X-Ray Image Reconstruction from a Diffraction Pattern Alone. *Phys. Rev. B* **2003**, *68*, 140101.
- (33) Martin, A. V.; Wang, F.; Loh, N. D.; Ekeberg, T.; Maia, F. R. N. C.; Hantke, M.; van der Schot, G.; Hampton, C. Y.; Sierra, R. G.; Aquila, A.; Bajt, S.; Barthelmess, M.; Chapman, H. N. et al. Noise-Robust Coherent Diffractive Imaging with a Single Diffraction Pattern. *Opt. Express* **2012**, *20*, 16650–16661.
- (34) Sekiguchi, S.; Niikura, K.; Matsuo, Y.; Ijiro, K. Hydrophilic Gold Nanoparticles Adaptable for Hydrophobic Solvents. *Langmuir* **2012**, *28*, 5503–5507.
- (35) Larson, T. A.; Joshi, P. P.; Sokolov, K. Preventing Protein Adsorption and Macrophage Uptake of Gold Nanoparticles via a Hydrophobic Shield. *ACS Nano* **2012**, *6*, 9182–9190.
- (36) Wang, Y.; Zeiri, O.; Neyman, A.; Stellacci, F.; Weinstock, I. A. Nucleation and Island Growth of Alkanethiolate Ligand Domains on Gold Nanoparticles. *ACS Nano* **2012**, *6*, 629–640.

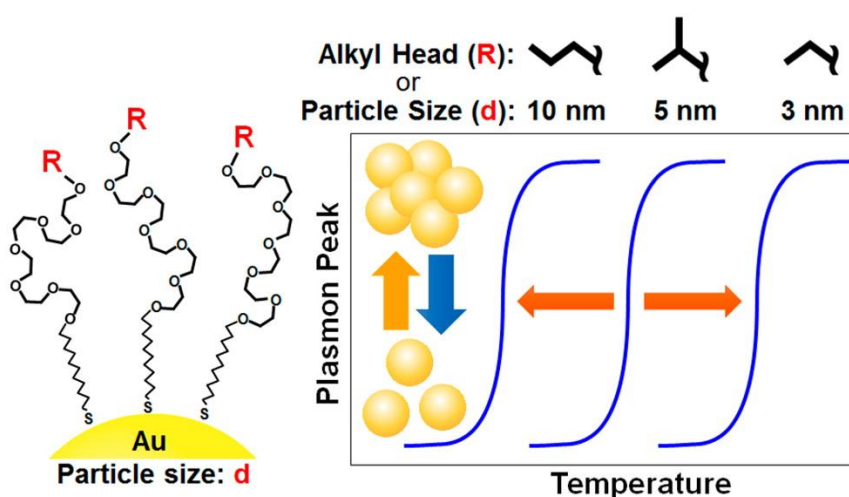
- (37) Singh, C.; Ghorai, P. K.; Horsch, M. A.; Jackson, A. M.; Larson, R. G.; Stellacci, F.; Glotzer, S. C. Entropy-Mediated Patterning of Surfactant-Coated Nanoparticles and Surfaces. *Phys. Rev. Lett.* **2007**, *99*, 226106.
- (38) Bianchi, E.; Blaak, R.; Likos, C. Patchy Colloids: State of the Art and Perspectives. *Phys. Chem. Chem. Phys.*, **2011**, *13*, 6397–6410.
- (39) Chapman, H. N.; Barty, A.; Marchesini, S.; Noy, A.; Hau-Riege, A. P.; Cui, C.; Howells, M.; Rosen, R.; He, H.; Spence, J. C. H.; Weistall, U.; Beetz, T.; Jacobsen, C.; Saphiro, D. High Resolution Ab Initio Three-Dimensional X-Ray Diffraction Microscopy. *J. Opt. Soc. Am. A* **2006**, *23*, 1179–1200.
- (40) Chen, Q.; Whitmer, J. K.; Jiang, S.; Bae, S. C.; Luijten, E.; Granick, S. Supracolloidal Reaction Kinetics of Janus Spheres. *Science* **2011**, *331*, 199–202.

Chapter 3

*Thermoresponsive Gold Nanospheres covered with
Oligo(Ethylene Glycol) Derivatives with an Alkyl Head*

Abstract:

This chapter presents the thermoresponsive assembly behaviors of gold nanospheres (GNSs; 3, 5, and 10 nm in diameter) that are coated with a self-assembled monolayer of oligo(ethylene glycol) (OEG) ligands terminated with alkyl heads. GNSs (5 nm in diameter) coated with OEG ligands without an alkyl head did not assemble within a temperature range from 20 to 70°C. However, GNSs coated with ethyl, iso-propyl, and propyl-headed OEG afforded assembly at temperatures of 56, 33, and 19°C, respectively, indicating that the assembly temperature can be tuned over a wide range by slight changes in the hydrophobicity of the alkyl head. Almost no hysteresis during the heating/cooling cycles was observed for the assembly/disassembly process. The diameter of the GNSs also affected the assembly temperature, with increases in the diameter of the GNS affording a lower assembly temperature. The ligand with the shorter alkyl tail length provided the lower assembly temperature of GNSs than the ligand with longer tail.



3-1. Introduction

The control of gold nanoparticle (GNP) assembly systems by external stimuli renders the on/off switching and tuning functions to plasmon-based materials.¹ Previously, the control of GNP assembly has been explored using external stimuli, such as temperature,^{2,3} pH,⁴⁻⁶ light,^{7,8} and metal ions.⁹⁻¹¹ The surface modification of nanoparticles with stimuli-responsive molecules is a promising and important approach to achieve the stimuli-responsive colloidal assembly.

Thermoresponsiveness by cooling or by heating is one of the simplest approaches to induce nanoparticle assembly. Nanoparticles assembled by cooling have been fabricated by grafting polymers with an upper critical solution temperature, such as poly(*N*-acryloylglycinamide)¹² or poly(*N,N'*-dimethyl(methacrylamido propyl) ammonium propanesulfonate).¹³ On the other hand, the nanoparticles assembled by heating have often been made by coating with a thermoresponsive polymer with a lower critical solution temperature (LCST), such as poly(*N*-isopropylacrylamide) (pNIPAm)¹⁴⁻¹⁷, poly(*N*-vinyl caprolactam)¹⁸, or oligo(ethylene glycol)-appending polymers including low-molecular weight (<2000 Da) PEG,¹⁹ copolymers of oligo(ethylene glycol) acrylates and di(ethylene glycol) acrylates,²⁰ and poly(ethylene oxide-*st*-propylene oxide).²¹ These nanoparticles can provide a wide range of applications related to various heat generation systems, such as photothermal conversion of plasmonic nanoparticles upon light irradiation^{22,23}. The temperature-dependent assembly/disassembly switching was utilized to prompt cellular internalization of nanoparticles²⁴. Hereafter, GNPs assembled by heating are referred as to “thermoresponsive GNPs”.

pNIPAm is a well-known polymer that undergoes phase transition at the LCST, around 31-32°C.²⁵ pNIPAm forms a coil conformation in water and collapses into an

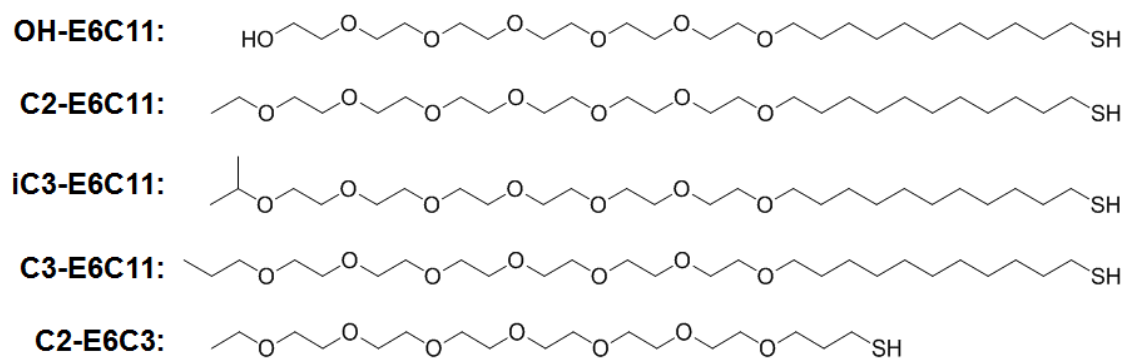
insoluble globular structure at the LCST, resulting in precipitation. The assembly of GNPs displaying a thermoresponsive polymer basically relies on the phase transition property of the polymer. Polyethylene glycol (PEG) also shows thermoresponsive behavior in water at high temperature or at a high ionic concentration.²⁶⁻²⁸ Therefore, it was reported that PEG-coated GNPs also show a thermal-response at a high ionic concentration.¹⁹ Additionally, ligand density is an important factor in determining the thermoresponsive property of nanoparticles. In general, the LCST of pPINAm remains almost constant as a function of the concentration of the polymer.²⁹ In fact, densely pNIPAm-coated GNPs prepared by a grafting-from approach showed a similar assembly temperature to free pNIPAm, while the assembly response was slower than that for free polymers.¹⁵

Beside polymers, it is known that nonionic surfactants with a hydrophilic oligo(ethylene glycol) (OEG) group show a clouding point due to micelle aggregation.³⁰ Direct force measurement between nonionic surfactant layers immobilized on a mica has been investigated using AFM, with the interaction shown to be increased with increases in water temperature due to dehydration from the OEG moieties.³¹ In principle, dehydration from OEG moieties at increased water temperature induces the attractive force between two nonionic surfactant layers by decreasing the steric repulsive force. I focus on the OEG modification of gold nanospheres (GNSs) using a self-assembled monolayer (SAM). The SAM formation using thiol ligands with a long alkyl chain is the simple and versatile approach to display functional groups on a gold substrate.^{32,33} Despite of the structural similarities between surfactant-based micelles and OEG-coated GNSs, there has been no study of the thermoresponsive behaviors of OEG-tethered self-assembled monolayer-coated GNSs to date.

Herein, I demonstrate that GNSs coated with a SAM of thiol-terminated

hexa(ethylene glycol) (HEG) derivatives (Scheme 3-1) show clear assembly/disassembly process. The alkyl-head capping of the terminal HEG was important to conferring the thermoresponsive function of GNSs in water. In this system, the phase transition of GNSs was determined by the surface properties originating from the SAM rather than the properties of the single molecule. In comparison with conventional polymer coating, the HEG is a small molecule without any molecular weight distribution, so that the HEG-GNSs show a thin homogeneous layer formed by the self-assembly of the alkyl thiol.

A slight difference in alkyl head structure has a large influence on the surface hydrophobicity of GNSs, so that the dehydration temperature would be affected by the alkyl head structure. In other words, I can easily tune the assembly temperature (T_A) by changing the alkyl head structure. Additionally, I investigated the effect of alkyl tail length on the thiol group side. This is the noticeable report on the thermoresponsive behaviors of GNSs coated with HEG-terminated SAMs. This simple approach based on a self-assembled monolayer with the surface ligand of low molecular weight will provide a new approach to the design of stimuli-responsive nanoparticles.

Scheme 3-1. Chemical structures of the HEG derivatives used in this chapter

3-2. Experimental section

3-2-1. General information.

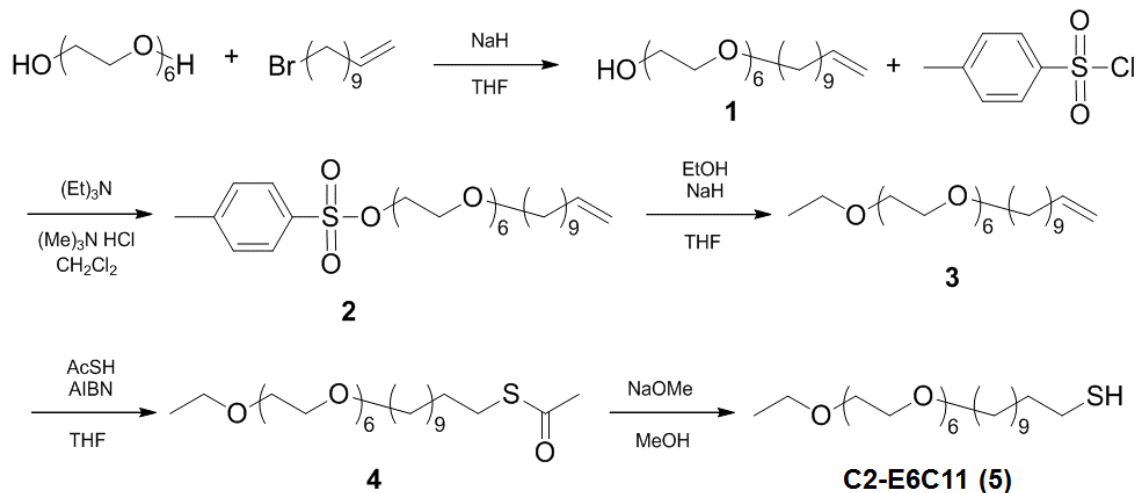
All commercially available reagents were used without further purification. All solvents were purchased from Wako Pure Chemical Industries Ltd. (Japan). Citrate-protected GNSs in aqueous solution (5 or 10 nm in diameter) were purchased from BBI Solutions (UK). According to the BBI Solutions website, GNSs with a diameter of 5 nm and 10 nm have maximum coefficients of variation of 15% and 10%, respectively⁴⁶. GNSs were concentrated using a CF-16RX centrifuge (Hitachi-Koki, Ltd., Japan).

3-2-2. Thiol ligand synthesis.

HEG derivatives with a hydroxyl, ethyl, iso-propyl, or propyl head and an alkyl-thiol tail, referred to as **OH-E6C11**, **C2-E6C11**, **iC3-E6C11**, and **C3-E6C11**, respectively, were synthesized (Scheme 1). I also synthesized a derivative with an ethyl head and a truncated alkyl-thiol tail (**C2-E6C3**).

• **Synthesis of C2-E6C11**

Scheme 3-2. Synthetic route to **C2-E6C11** ligand.



3,6,9,12,15,18-hexaoxapentacos-24-en-1-ol, **1**

Hexa(ethylene)glycol (15 g, 53 mmol) was dissolved in THF (55 ml). The solution was cooled on ice and added the 60% NaH in oil (1.6 g, 40 mmol) and 11-bromo-1-undecene (6.7 ml, 31 mmol). The reaction was allowed to warm to room temperature and stirred overnight. The solvent was removed, the residue was dissolved in CHCl_3 and washed twice with a saturated NaCl solution. The organic layer was dried over anhydrous Na_2SO_4 . The crude product was concentrated *in vacuo* and purified by flash chromatography on silica gel ($\text{CHCl}_3/\text{EtOAc} = 4:1$ (v/v) to $\text{EtOAc}/\text{MeOH} = 9:1$ (v/v)) to yield **1** (8.7 g, 66 %) as a clear syrup.

^1H NMR (400 MHz, CDCl_3): δ /ppm = 1.21-1.42 (m, 14H, alkyl chain), 1.59 (quin, 2H, $J = 6.9$ Hz, 6.9 Hz, alkyl chain), 2.01-2.09 (m, 2H, $=\text{CH}-\text{CH}_2$), 3.45 (t, 2H, $J = 6.8$ Hz, $-\text{O}-\text{CH}_2-$), 3.56-3.75 (m, 22H, $-\text{O}-\text{CH}_2-$), 4.90-5.04 (m, 2H, $-\text{CH}=\text{CH}_2$), 5.74-5.87 (m, 1H, $-\text{CH}=\text{CH}_2$). MALDI-TOF-MS (m/z): $[\text{M}+\text{Na}]^+$ calcd for $\text{C}_{23}\text{H}_{46}\text{O}_7\text{Na}$, 457.60; found, 457.38.

3,6,9,12,15,18-hexaoxonacos-28-en-1-yl 4-methylbenzenesulfonate, 2

Compound **1** (4.2 g, 9.7 mmol) was dissolved in dry CH₂Cl₂ (20 mL). The solution was cooled on ice and added the Et₃N (2.0 g, 19 mmol), trimethylamine hydrochloride (0.18 g, 1.9 mmol), p-tosylchloride (2.23 g, 12 mmol). The reaction was stirred on ice for 1.5 h. The solvent was removed, the residue was dissolved in CHCl₃ and wash three times with a saturated NaCl solution. The organic layer was dried over anhydrous Na₂SO₄. The crude product was concentrated *in vacuo* and purified by flash chromatography on silica gel (CHCl₃/MeOH =99:1 (v/v)) to yield **2** (6.1 g, 85 %) as a clear syrup.

¹H NMR (400 MHz, CDCl₃): δ /ppm = 1.28-1.36 (m, 14H, alkyl chain) 1.58 (s, 2H, alkyl chain) 2.03 (s, 2H, alkyl chain), 2.45 (s, 3H, CH₃ methyl) 3.44 (t, 4H, *J* = 5.5 Hz, -O-CH₂-), 3.55-3.68 (m, 24H, -O-CH₂-), 3.26-3.70 (m, 20H, -O-CH₂-), 4.92-5.00 (m, 2H, -CH=CH₂), 5.81 (m, 1H, -CH=CH₂), 7.35 (br-s, 2H, *phenyl*) , 7.80 (br-s, 2H, *phenyl*).
MALDI-TOF-MS (m/z): [M+Na]⁺ calcd for C₃₀H₅₂O₉SNa, 611.78; found, 611.68.

5,8,11,14,17,20,23-heptaoxatetatriacont-33-ene, 3

Ethanol (10 mL) was dissolved in dry THF (10 mL). The solution was cooled on ice and added the 60% NaH in oil (0.15 g, 3.8 mmol). After N₂ gas generation, compound **2** in THF (10 mL) was added dropwise. The reaction was allowed to warm to 40 °C and stirred 4h. The solvent was removed, and the residue was dissolved in CHCl₃ and washed twice with a saturated NaCl solution. The organic layer was dried over Na₂SO₄. The residue was evaporated under vacuum. The residue was chromatographed on a silica-gel column using CHCl₃ to yield **3** as a clear syrup (0.16 g, 49%).

¹H NMR (400 MHz, CDCl₃): δ /ppm = 0.91 (t, 3H, *J* = 7.54 Hz, CH₃ methyl), 1.21-1.41 (m, 14H, alkyl chain), 1.52-1.69 (m, 4H, alkyl chain), 2.04 (dt, 2H, *J* = 7.8 Hz, 7.3 Hz,

=CH-CH₂-CH₂), 3.44 (t, 2H, *J* = 6.8 Hz, -O-CH₂-), 3.49-3.70 (m, 24H, -O-CH₂-), 4.89-5.03 (m, 2H, -CH=CH₂), 5.75-5.88 (m, 1H, -CH=CH₂)

MALDI-TOF-MS (m/z) : [M+Na] calcd for C₂₅H₅₀O₇Na, 485.65; found, 484.90.

S-5,8,11,14,17,20,23-heptaoxatetatriacontan-34-yl ethanethioate, **4**

Compound **3** (0.16 g, 0.33 mmol), AcSH (125 mg, 1.65 mmol), and 2,2'-azobisisobutyronitrile (54 mg, 0.33 mmol) were dissolved in stabilizer free dry THF (20 mL). The mixture was refluxed for 5 h. The solvent was removed, the residue was dissolved in CHCl₃ and washed twice with a saturated NaCl solution. The organic layer was dried over Na₂SO₄ and evaporated under vacuum. The residue was chromatographed on silica-gel column using CHCl₃ to yield **4** as a clear syrup (0.19 g, 74%).

¹H NMR (400 MHz, CDCl₃): δ /ppm = 0.91 (t, 3H, *J* = 7.3 Hz, CH₃ methyl), 1.21-1.42 (m, 14H, alkyl chain), 1.50-1.65 (m, 4H, alkyl chain), 2.32 (s, 3H, *J* = 7.4 Hz, -CO-CH₃), 3.45 (t, 2H, *J* = 6.9 Hz, -O-CH₂-), 3.50-3.72 (m, 24H, -O-CH₂-)

MALDI-TOF-MS (m/z) : [M+Na] calcd for C₂₇H₅₄O₈Na, 561.77; found, 561.29.

5,8,11,14,17,20,23-heptaoxatetatriacontane-34-thiol, **5**

Compound **4** (0.14 g, 0.26 mmol) and 28% NaOMe in MeOH (15 μL, 0.077 mmol) were dissolved in MeOH (10 mL), and the mixture was stirred over 4 hrs at 50 °C. The neutralization was carried out by the addition of DOWEX50WX8-200. After the filtration through the filter paper, the solvent was removed under vacuum. The residue was dissolved in CHCl₃ and washed twice with a saturated NaCl solution. The organic layer was dried over Na₂SO₄ and evaporated under vacuum. The residue was purified by flash chromatography on silica gel (CHCl₃/Hexane = 9:1 (v/v)) to yield **5** as a clear syrup (32.7

mg, 25.1%).

^1H NMR (400 MHz, CDCl_3): δ /ppm = 1.21 (t, 3H, $J = 6.9$ Hz, CH_3 methyl), 1.24-1.41 (m, 14H, alkyl chain), 1.52-1.65 (m, 4H, alkyl chain), 2.52 (dt, 2H, $J = 7.2$ Hz, 7.4 Hz, $\text{CH}_2\text{-CH}_2\text{-SH}$), 3.44 (t, 2H, $J = 6.4$ Hz, $-\text{O-CH}_2-$), 3.50-3.68 (m, 24H, $-\text{O-CH}_2-$)

MALDI-TOF-MS (m/z): $[\text{M}+\text{Na}]$ calcd for $\text{C}_{27}\text{H}_{56}\text{O}_7\text{Na}$, 519.33; found, 518.73. HR-MS (ESI): calcd for $\text{C}_{27}\text{H}_{56}\text{O}_7\text{SNa}$ $[\text{M}+\text{Na}]^+$ 519.33260, found 519.3310.

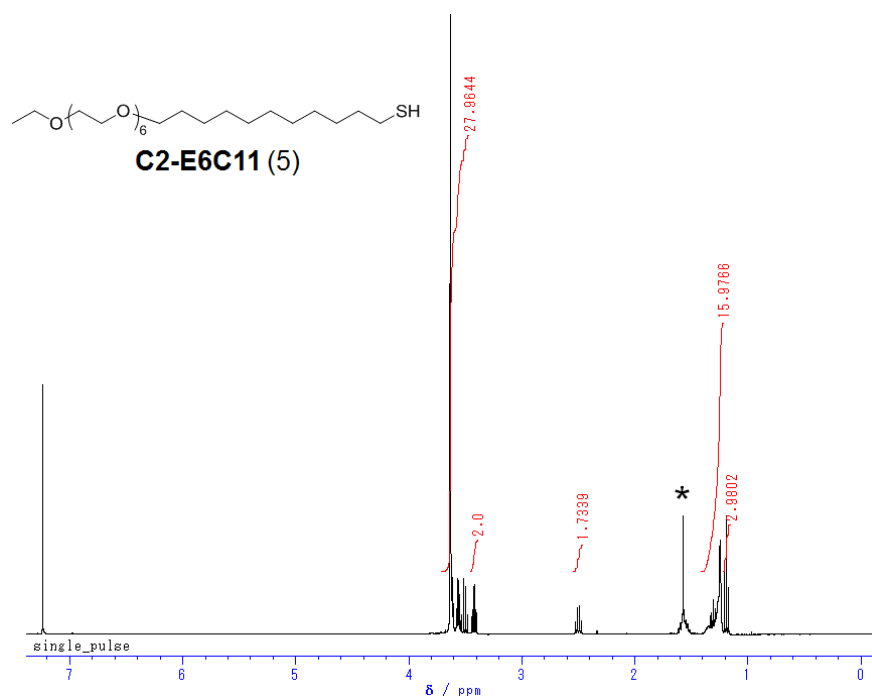
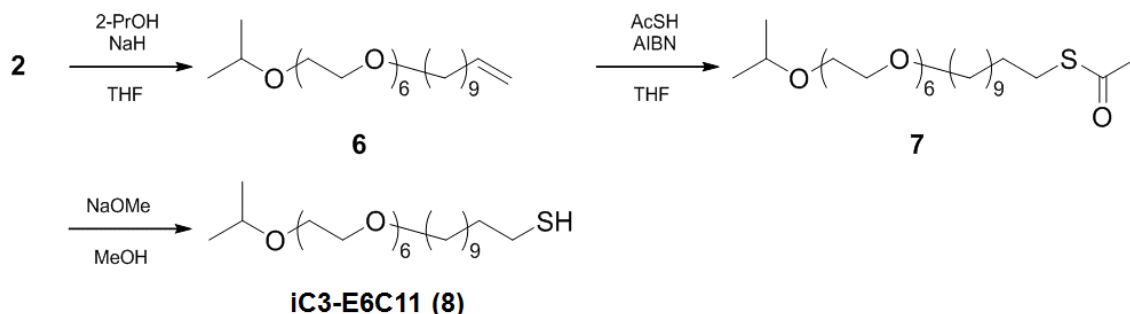


Figure 3-1. ^1H NMR spectrum of **C2-E6C11**. * represents a signal derived from water.

• **Synthesis of iC3-E6C11 ligand**

Scheme 3-3. Synthetic route to **iC3-E6C11** ligand.



2-methyl-3,6,9,12,15,18,21-heptaoxidotriacont-31-ene, 6

2-Propanol (10 mL) was cooled on ice and added the 60% NaH in oil (0.33 g, 6.4 mmol) under N₂ atmosphere. After H₂ gas generation, compound **2** (0.75 g) in THF (10 mL) was added dropwise. The reaction was allowed to room temperature and stirred 4 hrs. The solvent was removed, and the residue was dissolved in CHCl₃ and washed twice with a saturated NaCl solution. The organic layer was dried over anhydrous Na₂SO₄. The crude product was concentrated *in vacuo* and purified by flash chromatography on silica gel (CHCl₃/EtOAc = 9:1 (v/v) to CHCl₃/EtOAc = 8:2 (v/v)) to yield **6** (0.53 g, 87 %) as a clear syrup.

¹H NMR (400 MHz, CDCl₃): δ /ppm = 1.16 (d, 6H, *J* = 6.2 Hz, (CH₃)₂-CH-), 1.21-1.45 (m, 14H, alkyl chain), 1.57 (tt, 2H, *J* = 7.2 Hz, 7.2 Hz, alkyl chain), 2.04 (dt, 2H, *J* = 8.0 Hz, 7.3 Hz, =CH-CH₂-CH₂), 3.44 (t, 2H, *J* = 6.9 Hz, -O-CH₂-), 3.56-3.60 (m, 4H, -O-CH₂-), 3.54-3.71 (m, 20H, -O-CH₂-), 4.89-5.03 (m, 2H, -CH=CH₂), 5.75-5.88 (m, 1H, -CH=CH₂). MALDI-TOF-MS (*m/z*): [M+Na]⁺ calcd for C₂₆H₅₂O₇Na, 499.68; found, 499.10. [M+K]⁺ calcd for C₂₆H₅₂O₇, 515.79; found, 514.91.

S-(2-methyl-3,6,9,12,15,18,21-heptaoxidotriacontan-32-yl) ethanethioate, 7

Compound **6** (0.53 g, 1.11 mmol), AcSH (0.41 g, 5.55 mmol), and 2,2'-azobisisobutyronitrile (0.18 mg, 1.11 mmol) were dissolved in stabilizer free dry THF (20 mL). The mixture was refluxed for 4 hrs. The solvent was removed, the residue was dissolved in CHCl₃ and washed twice with a saturated NaCl solution. The organic layer was dried over anhydrous Na₂SO₄. The crude product was concentrated *in vacuo* and purified by flash chromatography on silica gel (CHCl₃/EtOAc = 9:1 (v/v) to CHCl₃/EtOAc = 7:3 (v/v)) to yield **7** (0.46 g, 75 %) as a clear syrup.

MALDI-TOF-MS (m/z): [M+Na]⁺ calcd for C₂₈H₅₆O₈Na, 575.79; found, 575.63.

2-methyl-3,6,9,12,15,18,21-heptaoxidotriacontane-32-thiol, **8**

Compound **7** (0.10 g, 0.18 mmol) and 28% NaOMe in MeOH (20 μL) were dissolved in MeOH (20 mL), and the mixture was stirred over 3 hrs at room temperature. The neutralization was carried out by the addition of Dowex (50WX8-200). After the filtration through the filter paper, the solvent was removed under vacuum. The residue was dissolved in CHCl₃ and washed twice with a saturated NaCl solution. The organic layer was dried over anhydrous Na₂SO₄. The crude product was concentrated *in vacuo* and purified by flash chromatography on silica gel (CHCl₃/EtOAc = 8:2 (v/v) to CHCl₃/EtOAc = 5:5 (v/v)) to yield **8** (10.2 mg, 11 %) as a clear syrup.

¹H NMR (400 MHz, CDCl₃): δ /ppm = 1.14 (d, 6H, *J* = 6.4 Hz, CH₃ methyl), 1.20-1.40 (m, 14H, alkyl chain), 1.50-1.64 (m, 4H, alkyl chain), 2.50 (dt, 2H, *J* = 7.4 Hz, 7.4 Hz, CH₂-CH₂-SH), 3.42 (t, 2H, *J* = 6.9 Hz, -O-CH₂-), 3.52-3.70 (m, 26H, -O-CH₂-). MALDI-TOF-MS (m/z): [M+Na]⁺ calcd for C₂₆H₅₄O₇Na, 533.76; found, 533.42.

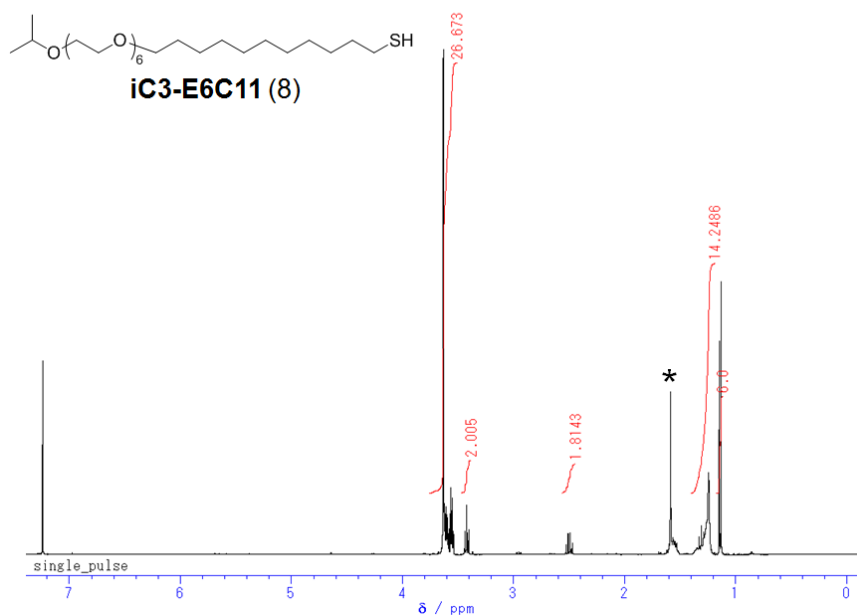
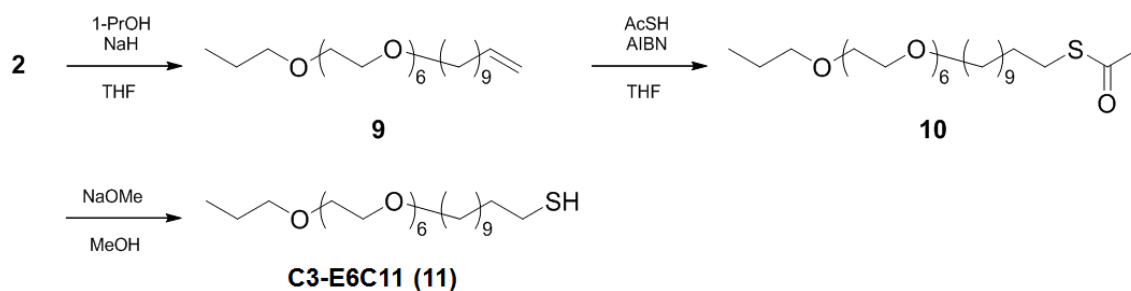


Figure 3-2. ^1H NMR spectrum of **iC3-E6C11**. * represents a signal derived from water.

- **Synthesis of C3-E6C11 ligand**

Scheme 3-4. Synthetic route to **C3-E6C11** ligand.



4,7,10,13,16,19,22-heptaoxatritriacont-32-ene, 9

1-Propanol (10 mL) was cooled on ice and added the 60% NaH in oil (0.33 g, 6.4 mmol) under N_2 atmosphere. After H_2 gas generation, compound **2** (0.75 g) in THF (10 mL) was

added dropwise. The reaction was allowed to room temperature and stirred for 4 hrs. The solvent was removed, and the residue was dissolved in CHCl_3 and washed twice with a saturated NaCl solution. The organic layer was dried over anhydrous Na_2SO_4 . The crude product was concentrated *in vacuo* and purified by flash chromatography on silica gel (CHCl_3 to $\text{CHCl}_3/\text{EtOAc} = 8:2$ (v/v)) to yield **9** (0.52 g, 85 %) as a clear syrup.

^1H NMR (400 MHz, CDCl_3): δ /ppm = 0.91 (t, 3H, $J = 7.4$ Hz, CH_3 methyl), 1.24-1.41 (m, 14H, alkyl chain), 1.53-1.65 (m, 4H, alkyl chain), 2.04 (dt, 2H, $J = 7.8$ Hz, 7.3 Hz, $=\text{CH}-\text{CH}_2-\text{CH}_2$), 3.42 (t, 2H, $J = 6.8$ Hz, $-\text{O}-\text{CH}_2-$), 3.44 (t, 2H, $J = 7.3$ Hz, $-\text{O}-\text{CH}_2-$), 3.56-3.60 (m, 4H, $-\text{O}-\text{CH}_2-$), 3.26-3.70 (m, 20H, $-\text{O}-\text{CH}_2-$), 4.89-5.03 (m, 2H, $-\text{CH}=\text{CH}_2$), 5.75-5.88 (m, 1H, $-\text{CH}=\text{CH}_2$). MALDI-TOF-MS (m/z): $[\text{M}+\text{Na}]^+$ calcd for $\text{C}_{26}\text{H}_{52}\text{O}_7\text{Na}$, 499.68; found, 499.09. $[\text{M}+\text{K}]^+$ calcd for $\text{C}_{26}\text{H}_{52}\text{O}_7\text{K}$, 499.68; found, 499.09.

S-4,7,10,13,16,19,22-heptaaxatritriacontan-33-yl ethanethioate, **10**

Compound **9** (0.52 g, 1.1 mmol), AcSH (0.41 g, 5.5 mmol), and 2,2'-azobisisobutyronitrile (0.18 mg, 1.1 mmol) were dissolved in stabilizer free dry THF (20 mL). The mixture was refluxed for 4 hrs. The solvent was removed, the residue was dissolved in CHCl_3 and washed twice with a saturated NaCl solution. The organic layer was dried over anhydrous Na_2SO_4 . The crude product was concentrated *in vacuo* and purified by flash chromatography on silica gel ($\text{CHCl}_3/\text{EtOAc} = 9:1$ (v/v) to $\text{CHCl}_3/\text{EtOAc} = 8:2$ (v/v)) to yield **10** (0.50 g, 83 %) as a clear syrup.

MALDI-TOF-MS (m/z): $[\text{M}+\text{Na}]^+$ calcd for $\text{C}_{28}\text{H}_{56}\text{O}_8\text{Na}$, 575.79; found, 575.69.

5,8,11,14,17,20,23-heptaooxatetatriacontane-34-thiol, 11

Compound **10** (0.10 g, 0.18 mmol) and 28% NaOMe in MeOH (20 μ L) were dissolved in MeOH (20 mL), and the mixture was stirred for 3 hrs at room temperature. The neutralization was carried out by the addition of Dowex (50WX8-200). After the filtration through the filter paper, the solvent was removed under vacuum. The residue was dissolved in CHCl_3 and washed twice with a saturated NaCl solution. The organic layer was dried over anhydrous Na_2SO_4 . The crude product was concentrated *in vacuo* and purified by flash chromatography on silica gel ($\text{CHCl}_3/\text{EtOAc} = 8:2$ (v/v) to $\text{CHCl}_3/\text{EtOAc} = 1:1$ (v/v)) to yield **11** (68.2 mg, 74 %) as a clear syrup.

^1H NMR (400 MHz, CDCl_3): δ /ppm = 0.89 (t, 3H, $J = 7.5$ Hz, CH_3 methyl), 1.20-1.41 (m, 14H, alkyl chain), 1.50-1.65 (m, 4H, alkyl chain), 2.52 (dt, 2H, $J = 7.3$ Hz, 7.3 Hz, $\text{CH}_2\text{-CH}_2\text{-SH}$), 3.44-3.76 (m, 4H, $-\text{O-CH}_2-$), 3.52-3.70 (m, 26H, $-\text{O-CH}_2-$). MALDI-TOF-MS (m/z): $[\text{M}+\text{Na}]^+$ calcd for $\text{C}_{26}\text{H}_{54}\text{O}_7\text{Na}$, 533.76; found, 532.86.

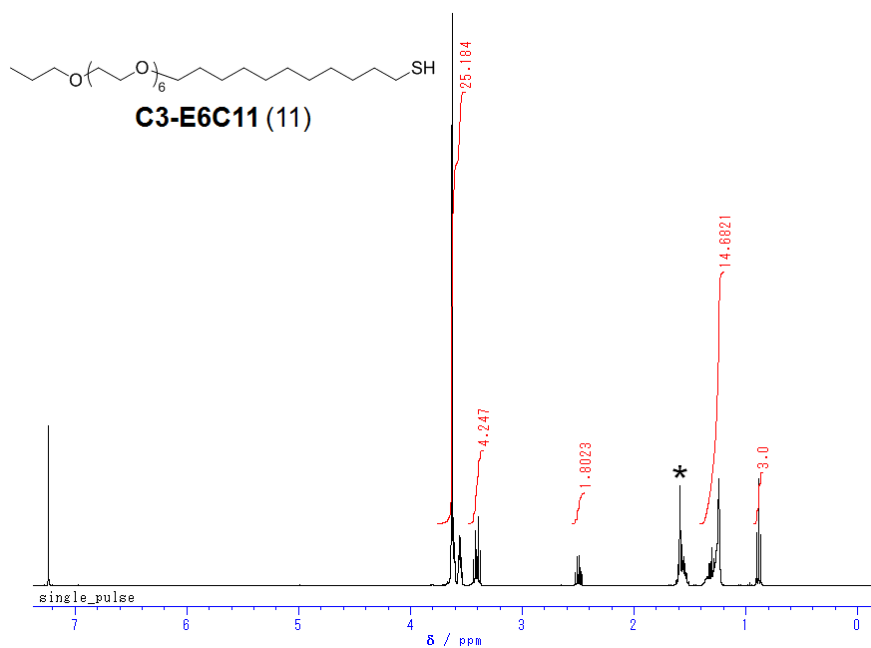
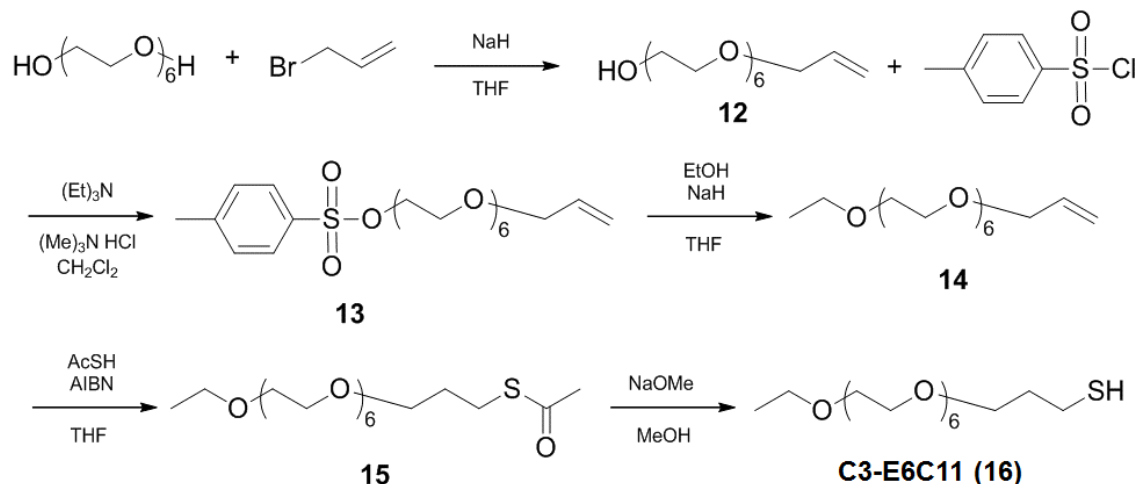


Figure 3-3. ^1H NMR spectrum of **C3-E6C11**. * represents a signal derived from water.

• **Synthesis of C2-E6C11 ligand**

Scheme 3-5. Synthetic route to **C2-E6C3** ligand.



3,6,9,12,15,18-hexaoxahenicos-20-en-1-ol, **12**

Hexa(ethylene)glycol (30 g, 0.11 mol) was dissolved in THF (110 ml). The solution was cooled on ice and the 60% NaH in oil (3.2 g, 80 mmol) and 3-bromoprop-1-ene (5.2 ml, 61 mmol). The reaction was allowed to warm to room temperature and stirred overnight. The solvent was removed, the residue was dissolved in CHCl_3 and washed twice with a saturated NaCl solution. The organic layer was dried over anhydrous Na_2SO_4 . The crude product was concentrated *in vacuo* and purified by flash chromatography on silica gel (CHCl_3 to EtOAc/MeOH = 9:1 (v/v)) to yield **12** (13.2 g, 67 %) as a clear syrup.

^1H NMR (400 MHz, CDCl_3): δ /ppm = 3.38-3.88 (m, 26H, -O- CH_2 -), 4.03 (br-d, 2H, J = 5.8 Hz, -O- CH_2 -), 5.17-5.30 (m, 2H, - $\text{CH}=\text{CH}_2$), 5.87-5.97 (m, 1H, - $\text{CH}=\text{CH}_2$). MALDI-TOF-MS (m/z): $[\text{M}+\text{Na}]^+$ calcd for $\text{C}_{15}\text{H}_{30}\text{O}_7\text{Na}$, 345.19; found, 345.17.

3,6,9,12,15,18-hexaoxonacos-28-en-1-yl 4-methylbenzenesulfonate, 13

Compound **12** (2.5 g, 7.9 mmol) was dissolved in dry CH₂Cl₂ (20 mL). The solution was cooled on ice and added the Et₃N (1.6 g, 16 mmol), trimethylamine hydrochloride (0.15 g, 1.6 mmol), p-tosylchloride (1.8 g, 9.5 mmol). The reaction was stirred on ice for 3 h. The solvent was removed, the residue was dissolved in CHCl₃ and wash three times with a saturated NaCl solution. The organic layer was dried over anhydrous Na₂SO₄. The crude product was concentrated *in vacuo* and purified by flash chromatography on silica gel (CHCl₃/EtOAc = 1:1 (v/v)) to yield **13** (3.1 g, 83 %) as a clear syrup.

¹H NMR (400 MHz, CDCl₃): δ /ppm = 2.42 (s, 3H, CH₃ methyl) 3.44 (t, 4H, *J* = 5.5 Hz, -O-CH₂-), 3.51-3.69 (m, 22H, -O-CH₂-), 3.97-4.02 (m, 2H, -O-CH₂-), 5.11-5.26 (m, 2H, -CH=CH₂) 5.83-5.95 (m, 1H, -CH=CH₂), 7.32 (d, 2H, *J* = 7.8 Hz, *phenyl*) , 7.78 (br-d, 2H, *J* = 8.3 Hz *phenyl*). MALDI-TOF-MS (m/z): [M+Na]⁺ calcd for C₂₂H₃₆O₉SNa, 499.57; found, 499.05.

3,6,9,12,15,18,21-heptaoxatetracos-23-ene, 14

Ethanol (20 mL) was dissolved in dry THF (10 mL). The solution was cooled on ice and added the 60% NaH in oil (0.63 g, 1.6 mmol). After N₂ gas generation, compound **13** (1.5 g, 3.2 mmol) in dry THF (10 mL) was added dropwise. The reaction was allowed to warm to 40 °C and stirred for 4 h. The solvent was removed, and the residue was dissolved in CHCl₃ and washed twice with a saturated NaCl solution. The organic layer was dried over Na₂SO₄. The residue was evaporated under vacuum and was purified by flash chromatography on silica gel (CHCl₃/EtOAc = 1:2 (v/v)) to yield **14** as a clear syrup (0.93 g, 81%).

¹H NMR (400 MHz, CDCl₃): δ /ppm = 1.12 (t, 3H, *J* = 7.2 Hz, CH₃ methyl), 3.42-3.84

(m, 26H, -O-CH₂-), 4.04 (m, 2H, -O-CH₂-CH=CH₂), 5.13-5.28 (m, 2H, -CH=CH₂), 5.85-5.93 (m, 1H, -CH=CH₂)

MALDI-TOF-MS (m/z): [M+Na] calcd for C₁₇H₃₄O₇Na, 373.44; found, 373.10.

S-3,6,9,12,15,18,21-heptaoxatetracosan-24-yl ethanethioate, 15

Compound **14** (0.50 g, 1.4 mmol), AcSH (0.54 mg, 7.1 mmol), and 2,2'-azobisisobutyronitrile (54 mg, 1.4 mmol) were dissolved in stabilizer free dry THF (20 mL). The mixture was refluxed for 5 h. The solvent was removed, the residue was dissolved in CHCl₃ and washed twice with a saturated NaCl solution. The organic layer was dried over Na₂SO₄ and evaporated under vacuum. The residue was purified by flash chromatography on silica gel (CHCl₃/EtOAc = 5:5 (v/v) to CHCl₃/EtOAc = 3:7 (v/v)) to yield **15** as a clear syrup (0.37 g, 61%).

¹H NMR (400 MHz, CDCl₃): δ /ppm = 0.96 (t, 3H, *J* = 7.3 Hz, CH₃ methyl), 1.82 (tt, 2H, *J* = 7.3 Hz, alkyl chain), 2.32 (s, 3H, CO-CH₃), 2.83 (t, 2H, *J* = 7.3 Hz, -CH₂-S), 3.40-3.72 (m, 28H, -O-CH₂-)

MALDI-TOF-MS (m/z): [M+Na] calcd for C₁₉H₃₈O₇Na, 449.56; found, 449.10.

3,6,9,12,15,18,21-heptaoxatetracosane-24-thiol, 16

Compound **15** (0.11 g, 0.23 mmol) was dissolved in MeOH (18 mL), and conc. HCl was added to the solution. Then, the mixture was refluxed for 4 hrs. The solvent was removed under vacuum. The residue was dissolved in CHCl₃ and washed twice with a saturated NaCl solution. The organic layer was dried over Na₂SO₄ and evaporated under vacuum to yield **16** as a clear syrup (99.2 mg, 95%).

¹H NMR (400 MHz, CDCl₃): δ /ppm = 1.19 (t, 3H, *J* = 6.9 Hz, CH₃ methyl), 1.36 (t, 1H,

$J = 7.8$ Hz, $-SH$), 1.85 (tt, 2H, $J = 7.3$ Hz, 7.3 Hz, $-CH_2-CH_2-CH_2-$), 2.52 (dt, 2H, $J = 7.8$ Hz, 7.8 Hz, CH_2-CH_2-SH), 3.44-3.68 (m, 28H, $-O-CH_2-$)

MALDI-TOF-MS (m/z): $[M+Na]$ calcd for $C_{17}H_{36}O_7SNa$, 407.52; found, 407.14.

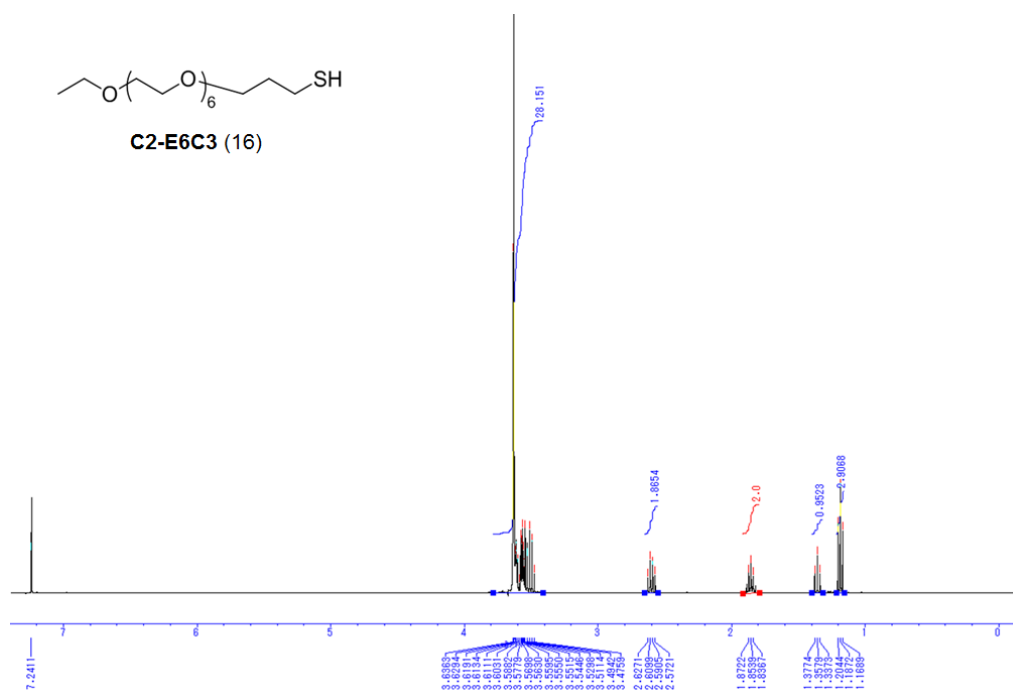


Figure 3-4. 1H NMR spectrum of **C2-E6C3**.

3-2-3. Surface modification of GNSs

GNSs (5 and 10 nm in diameter) coated with hexa(ethylene glycol) derivatives were prepared *via* a ligand exchange reaction. Briefly, citrate-protected GNSs (5 nm) were concentrated up to 3.1 μM by ultrafiltration using an Amicon Ultra 100 K filter (Merck MilliPore, Germany) with centrifugation (10,000 g for 10 min). 10-nm GNSs were concentrated up to 370 nM by centrifugation (10,000 g for 10 min). The concentrated citrate-protected GNSs (20 μL) were added to a methanol solution of the thiolate ligand molecules (100 μL). In this exchange reaction, the total ligand concentration was adjusted to 10 equiv. Au atoms on the surface of each nanoparticle. Based on the size distribution

of 5- and 10-nm GNSs, this equivalent corresponds to 7.6-14 equiv. and 8.3-12 equiv., respectively. In the case of 5-nm GNSs, the concentration of the ligand solution was set at 6.2 mM, and the number of surface Au atoms was calculated to be 998/particle according to the literature.³⁴ In the case of 10-nm GNSs, the number of surface Au atoms was 4192/particle and the concentration of the ligand solution was 3.1 mM. After incubation for 12 hours at 4°C, the ligand-exchanged GNSs were washed 3 times by the addition of methanol up to 500 μ L, centrifugation (5-nm GNSs: 14,000 g for 60 min; 10-nm GNSs: 10,000 g for 10 min), and the removal of the supernatant (about 480 μ L) to remove the free thiol ligands. After the removal of the residual methanol using a centrifugal evaporator, pure water was added to the dried GNSs down to OD₅₂₀ = 1.

3-2-4. Synthesis of 3-nm GNSs coated with C2 ligand

3-nm GNSs modified with **C2-E6C11** ligands were synthesized according to previous method reported by Brust and co-workers.³⁵ HAuCl₄·3H₂O (31.4 mg) and acetic acid (0.5 mL) were mixed to iso-propanol (50 mL). After the **C2-E6C11** ligand (12.6 mg) was dissolved into this solution, a freshly prepared methanol solution of NaBH₄ (5 mL, 0.5 M) was added under vigorous stirring at room temperature. The color of the solution was swiftly changed from yellow to brown. After stirring for 3 hours, the solvent was removed by evaporation *in vacuo* and resolved in a mixture of water and ethanol (1:1 (v/v)). The prepared 3-nm GNSs were washed with the water/ethanol (1:1 (v/v)) to remove the free **C2-E6C11** ligands and then twice with pure water to remove the ethanol by ultrafiltration using Amikon Ultra filter (10 K cut off) with centrifugation (12,000 g for 15 min). The size was 3.3±1.0 nm as confirmed from STEM images.

3-2-5. Characterization

- **UV-Vis Extinction Spectroscopy**

The UV-Vis spectra of the GNSs and transmittance of all ligand solutions were measured using a UV-Vis spectrophotometer UV-2600 (Shimadzu Corporation, Japan). For measurement of the thermoresponsive assembly of GNSs, the heating rate was 0.5°C/min. The concentrations of 3-, 5-, and 10-nm GNSs were 530 nM, 83 nM, and 9.5 nM, respectively. The extinction spectra were normalized at the wavelength with the highest absorbance in the range from 400 to 700 nm. The T_A was defined as the temperature at which the slope of the plot of plasmonic extinction peak shifts vs. temperature reached a maximum value by curve fitting. Transmittance at 500 nm of all ligand solutions was measured at a concentration of 10 mM and a heating rate of 1.0°C/min. The clouding point is defined as the temperature at which the transmittance of the ligand solution is located at 50% intensity.

- **Dynamic light scattering (DLS) and zeta-potential measurement**

The size of the GNSs or their assembly were measured using a Zeta-potential & Particle size Analyzer ELSZ-2000 (Otsuka Electronics Co., Ltd., Japan). The emission wavelength for the measurements was 633 nm. In prior to the measurement, the temperature was kept constant for 10 min. Cumulant analysis was applied to determine the hydrodynamic diameter. Zeta-potential of GNSs was measured by a Delsa Nano HC system (Beckman Coulter, Inc., USA).

- **STEM measurement**

Scanning transmission electron microscope (STEM) images were obtained using STEM HD-2000 (Hitachi High-Tech Manufacturing & Service Co., Ltd, Japan) with a 200 kV

accelerating voltage. STEM samples were prepared by adding a drop of the GNS solution onto the collodion membrane attachment mesh (Nisshin EM, Japan) and dried in a desiccator. For observations of the assembled structure at 60°C, water in the solvent was evaporated at 60°C in a thermostatic oven.

- **Inductively coupled plasma atomic emission spectroscopy (ICP-AES)**

The ligand densities on the GNSs were determined with an ICPE-9000 spectroscope (Shimadzu Corporation, Japan). After removal of the solvent by centrifugal evaporator, the ligand-exchanged GNSs were treated with aqua regia (1 mL) for 30 min. The resultant solutions were diluted with pure water (9 mL). The concentrations of gold and sulfur ions were determined by ICP-AES after obtaining a calibration curve for the gold and sulfur ions at various concentrations. Ligand densities were calculated from the ratio of S and Au.

3-3. Results and Discussion

3-3-1. Clouding points of free ligand molecules

HEG derivatives with a hydroxyl, ethyl, iso-propyl, or propyl head and an alkyl-thiol tail, referred to as **OH-E6C11**, **C2-E6C11**, **iC3-E6C11**, and **C3-E6C11**, respectively, were synthesized. In chapter 3, the headed functional group influences to the thermoresponsive behavior, so that **E6C11** in chapter 3 is referred to as **OH-E6C11** to emphasize the headed functional group. First, the thermoresponsiveness of free ligand molecules (**OH-E6C11**, **C2-E6C11**, and **iC3-E6C11** ligands, but not **C3-E6C11** ligand) in water were investigated by monitoring optical transmittance. The **OH-E6C11**, **C2-E6C11**, and **iC3-E6C11** ligands were soluble in water, whereas **C3-E6C11** was insoluble. Figure 3-5 shows the transmittance vs. temperature plots for the ligand solutions (10 mM). The clouding points of the **OH-E6C11**, **C2-E6C11**, and **iC3-E6C11** ligands were 49, 25, and 15°C, respectively (Table 3-1).

When the hydrophobicity of the head group was increased, the clouding point was significantly decreased. The insolubility of **C3-E6C11** ligand in water might result from its lower clouding point. The different hydrophobicity of the ligands can affect both the dehydration temperature and the hydrophobic attraction between the outermost surfaces of the ligand shell on two micelles.

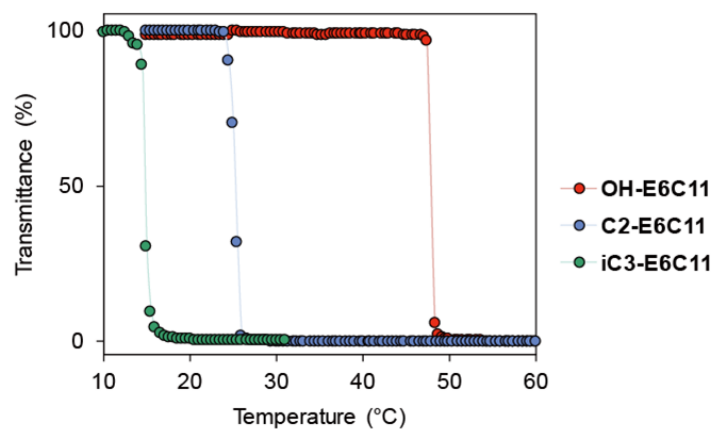


Figure 3-5. Transmittance vs. temperature for aqueous solutions of **OH-E6C11** (red), **C2-E6C11** (blue), and **iC3-E6C11** (green) ligands (10 mM).

Table 3-1. Summary of the clouding points of each ligand in water and assembly temperatures of HEG-derivative-modified GNSs (5 nm)

<i>Ligand</i>	<i>Clouding point of free molecules</i>	<i>T_A of 5-nm GNSs</i>
C3-E6C11	Insoluble ^a	19°C
iC3-E6C11	15°C	33°C
C2-E6C11	25°C	56°C
OH-E6C11	49°C	Not detected ^a

^atemperature range from 5 to 70°C

3-3-2. Thermoresponsive assembly of 5-nm GNSs

- **Assembly behavior upon heating**

The surface modification of 5-nm GNSs with HEG-derivatives was performed in water through ligand exchange reaction on citrate-protected GNSs and confirmed by zeta-potential measurements. The zeta-potential of the GNSs was changed from strongly negative (-49 mV) for the original citrate-protected GNSs to close to neutral (Table 3-2). This result supports the notion that the citrate on the GNSs was practically replaced with the HEG ligand by ligand exchange reaction under these conditions. The UV-Vis extinction spectra of the obtained GNSs showed a maximum wavelength \sim 520 nm, which is consistent with that of well-dispersed citrate-protected GNSs in aqueous solution (Figure 3-6a, c: blue line).

The thermoresponsive assembly of the GNSs was analyzed by UV-Vis spectrometry, DLS measurements, and STEM imaging. The extinction spectra of dispersed 5-nm GNSs modified with **OH-E6C11** (**OH-5-GNSs**) at between 25 and 70°C are shown in Figure 3-6a and b. No spectral changes were observed on the changes in temperature within this range. The absence of T_A for **OH-5-GNSs** in this range indicates that water molecules were not removed from the HEG portion, the terminals of which were immobilized on the GNS surface. **C2-5-GNSs**, on which the ethyl head is exposed on the outermost surface, was also dispersed in water at room temperature. However, the solution of **C2-5-GNSs** showed a red shift in the maximum wavelength at around 56°C due to plasmon coupling and broadening of the peak when the temperature was increased from 25°C to 70°C (Figure 3-6c, d). This peak shift indicated that **C2-5-GNSs** were assembled at temperatures over 50°C. The broadening of the peak means large scattering so that this also supports the notion of assembly formation. This spectral shift supports

that the alkyl head could more effectively induce the dehydration of the HEG portion than the hydroxyl head. Interestingly, the change in color of this solution with change in temperature was completed within 15 s.

Table. 3-2 Summary of zeta-potential of the GNSs

Sample	Zeta-potential
Citrate-5-GNSs	-49 mV
C2-5-GNSs	-1.5 mV
Citrate-10-GNSs	-48 mV
C2-10-GNSs	6.4 mV
C2-3-GNSs	-4.5 mV

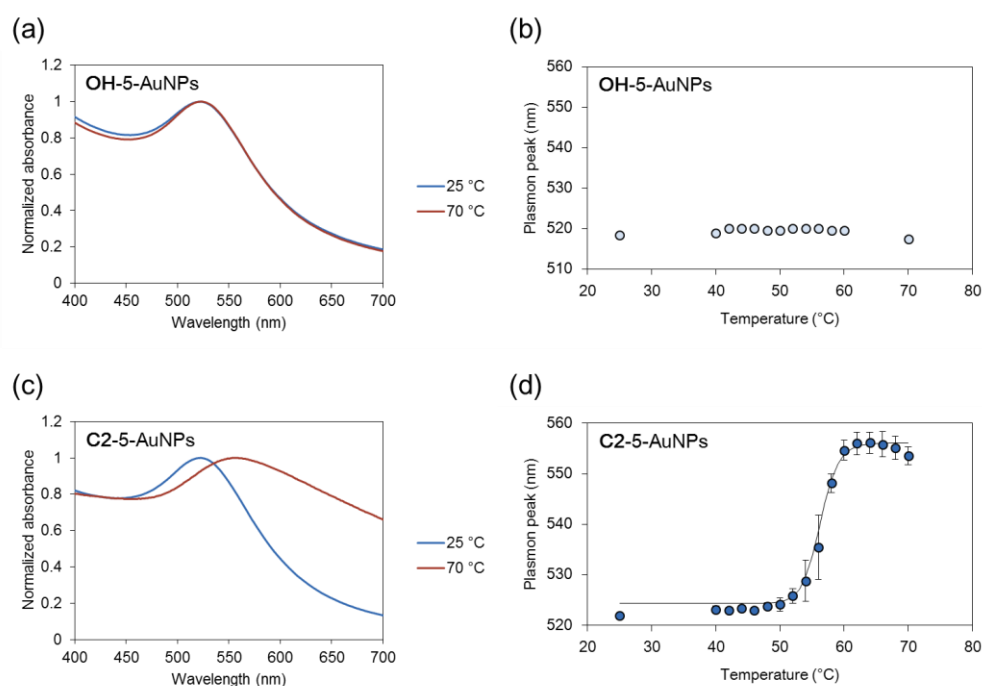


Figure 3-6. Normalized optical extinction spectra of (a) OH-5-GNSs and (c) C2-5-GNSs at 25 and 70 °C in water. Temperature-dependent changes in plasmon peak between 25 and 70 °C was plotted for (b) OH-5-GNSs and (d) C2-5-GNSs. Heating rate was 0.5 °C/min. The extinction spectra were normalized at the wavelength with the highest absorbance in the range from 400 to 700 nm.

DLS measurements also revealed the temperature-dependent assembly of **C2-5-GNSs**. Two peaks (around 10 nm and 100 nm) were observed in the intensity distributions vs. hydrodynamic diameter of **C2-5-GNSs** at 25°C, corresponding to the dispersed GNSs and the assembly (Figure 3-7a). Hence, a portion of the **C2-5-GNSs** were assembled even below T_A . However, number distributions (Figure 3-7c) show that the number of assemblies was very small. Therefore, the hydrodynamic diameter of **C2-5-GNSs** upon heating, as calculated by cumulant analysis, showed a gradual increase from ca. 50°C, reaching around 600 nm at over 60°C, and the temperature range of these changes corresponded with that of the extinction peak shift (Figure 3-7b). STEM observations also supported this assembly (Figure 3-8). Additionally, re-shifts (shift back) of the plasmon peak and hydrodynamic diameter by sequential heating was observed over 65°C (Figure 3-6d and 3-7b). The re-shifts can be explained that large aggregates exhibiting a large plasmon peak shift were partially precipitated in a UV cuvette and did not participate in the UV-vis spectrum and light scattering, while smaller aggregates stayed in suspension.

In the case of micelles or liposomes, it is well known that the exposure of the hydrophobic part can induce fusion.^{36,37} This means that the exposure, to a degree, of the hydrophobic part is an important factor. Therefore, the reason why no assembly of **OH-5-GNSs** was observed is probably that hydrophobic part of the ligand at the alkyl tail was isolated on the inner side of the SAM with the HEG part when it was immobilized on the GNSs at high density. In fact, a clouding point was observed for the ligand molecules in aqueous solution as shown above.

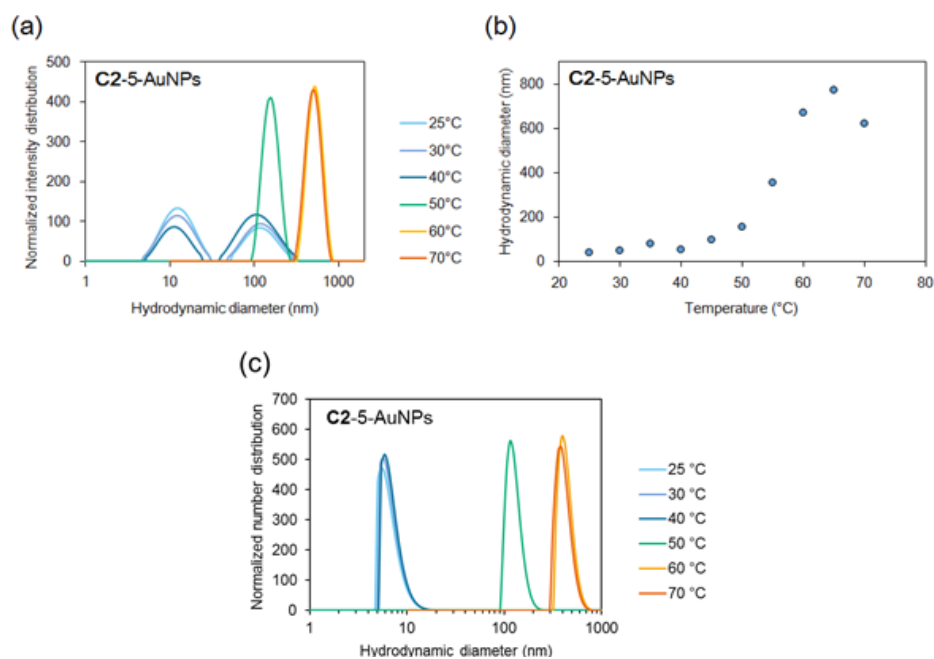


Figure 3-7. DLS analyses of C2-5-GNSs at different temperatures. (a) Intensity distribution vs. hydrodynamic diameter of C2-5-GNSs at different temperatures and (b) temperature-dependent change of the hydrodynamic diameter of C2-5-GNSs determined by the cumulant analysis. (c) Number distribution vs. hydrodynamic diameter of C2-5-GNSs at different temperatures.

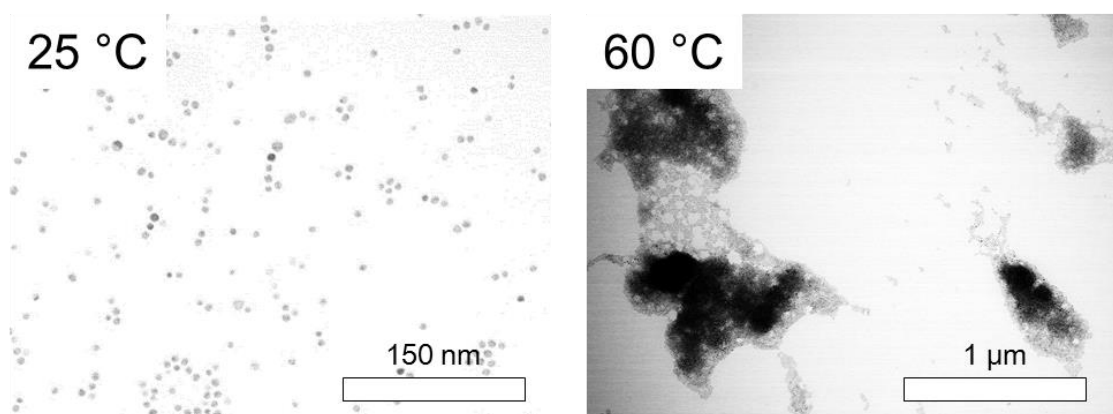


Figure 3-8. STEM images of C2-5-GNSs dried at 25 and 60°C.

- **The reversibility of thermoresponsive assembly**

To examine the reversibility of this assembly/disassembly process using **C2-5-GNSs**, the heating-cooling cycles were tested. Figure 3-9 shows the reversible changes of the maximum wavelength between 25 and 70°C. Figure 3-9a shows the temperature-dependent changes in the plasmon peak of **C2-5-GNSs**. This heating-cooling process can be repeated many times (Figure 3-9b). Further, little hysteresis was observed between the heating and cooling processes. In some previously reported cases using polymers (e.g., pNIPAM), obvious hysteresis was observed during the heating-cooling process due to the intermolecular hydrogen bonds.³⁸ The pNIPAM aggregations are induced by van der Waals interaction and hydrogen bonds between the polymers are then formed after aggregation. pNIPAM-coated nanoparticles also showed significant hysteresis.³⁹ On the other hand, it has been reported that polymers composed of ethylene glycol analogues exhibit a more uniform thermal profile.⁴⁰ Lequeux *et al.* reported that GNSs coated with poly(ethylene oxide-*st*-propylene oxide) exhibited slight hysteresis.²¹ Therefore, the reason why little hysteresis was observed for the **C2-5-GNSs** is that they did not form additional interparticle bonds, such as hydrogen bonds, after aggregation.

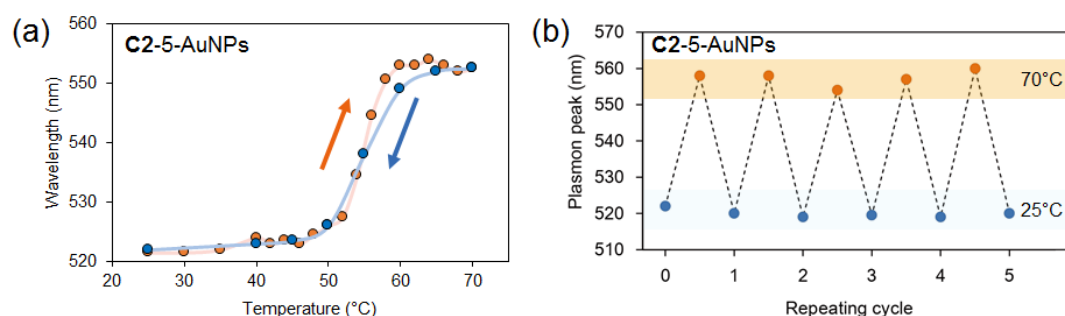


Figure 3-9. (a) Temperature-dependent changes in the plasmon peak of **C2-5-GNSs** (orange line: heating process; blue line: cooling process). (b) Reversible changes in the plasmon peak at 25 and 70°C.

- **The assembly temperature of 5-nm GNSs in NaCl solution**

It is well known that ionic concentration can affect the clouding point of nonionic surfactants or polymers.²⁶ In general, a higher ionic concentration renders a lower LCST for polymers by promoting dehydration. Therefore, I examined the effects of NaCl on T_A (Figure 3-10a). When the NaCl concentration was increased, the T_A of C2-5-GNSs fell: 56, 45, 38, and 28°C for 0, 0.5, 1, and 2 M NaCl solutions, respectively. This shift in T_A with changes in salt concentration was similar to the shift in clouding point for the C2 ligand in free solution, although the T_A themselves were different (Figure 3-10b). These results also support the notion that the thermoresponsive assembly of C2-5-GNSs is mainly driven by the dehydration of the HEG part.

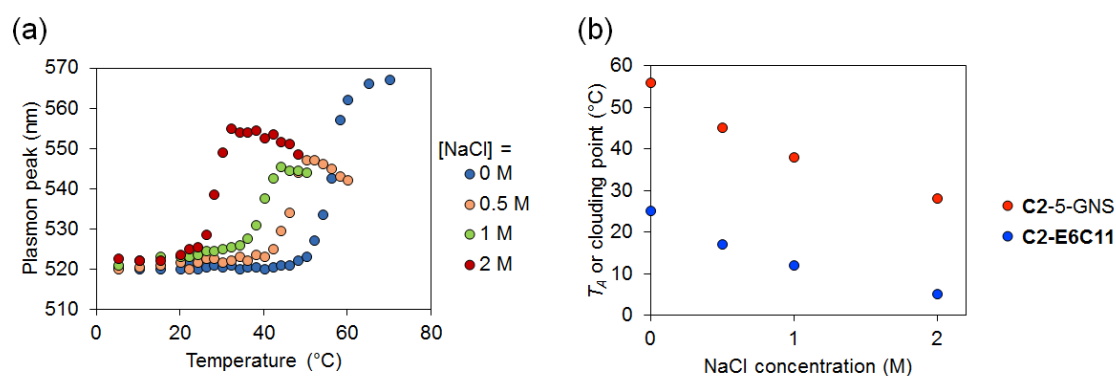


Figure 3-10. (a) Temperature-dependent plasmon peak shifts of C2-5-GNSs under various NaCl concentrations. [NaCl] = 0M (Blue), 0.5 M (Orange), 1 M (Green), 2 M (Red). (b) Assembly temperatures (T_A) of C2-5-AuNPs (red dots) and the clouding point of free C2-E6C11 ligand (blue dots) in water with various NaCl concentrations.

3-3-3. Effects of the Alkyl heads

It is already shown that the thermoresponsiveness of the **OH-E6C11** and **C2-E6C11** ligands clearly differed. Therefore, I then investigated the effects of the alkyl head group, which is exposed on the outermost surface of the GNSs. I then also fabricated **iC3-** and **C3-5-GNSs** additionally to examine the effects of the alkyl heads of ligand molecules on the assembly of GNSs. Normalized optical extinction spectra of **iC3-** and **C3-5-GNSs** were shown in Figure 3-11a and b. T_A was determined by plasmonic extinction peak shift (Figure 3-11c). The T_A of **C2-**, **iC3-**, and **C3-5-GNSs** were 56, 33, and 19°C, respectively. The clouding points of the ligand molecules in water and assembly temperatures of HEG-derivative-modified GNSs (5 nm) are summarized in Table 1. The T_A was also changed by the hydrophobicity of the head of the ligands. I consider that the increased hydrophobicity of alkyl head on GNS surface can induce a further decrease in the dehydration temperature. It is worth mentioning that even small changes in the alkyl head structure can cause large changes in the thermoresponsive assembly of GNSs. Further, I also observed that the T_{AS} of the GNSs were higher than the clouding points of ligand molecules in solution. This result indicates that the effect of the hydrophobic part of the undecanethiol tail was diminished by attachment on the surface of the GNSs due to its isolation and restricted mobility on the inner side of the SAM.

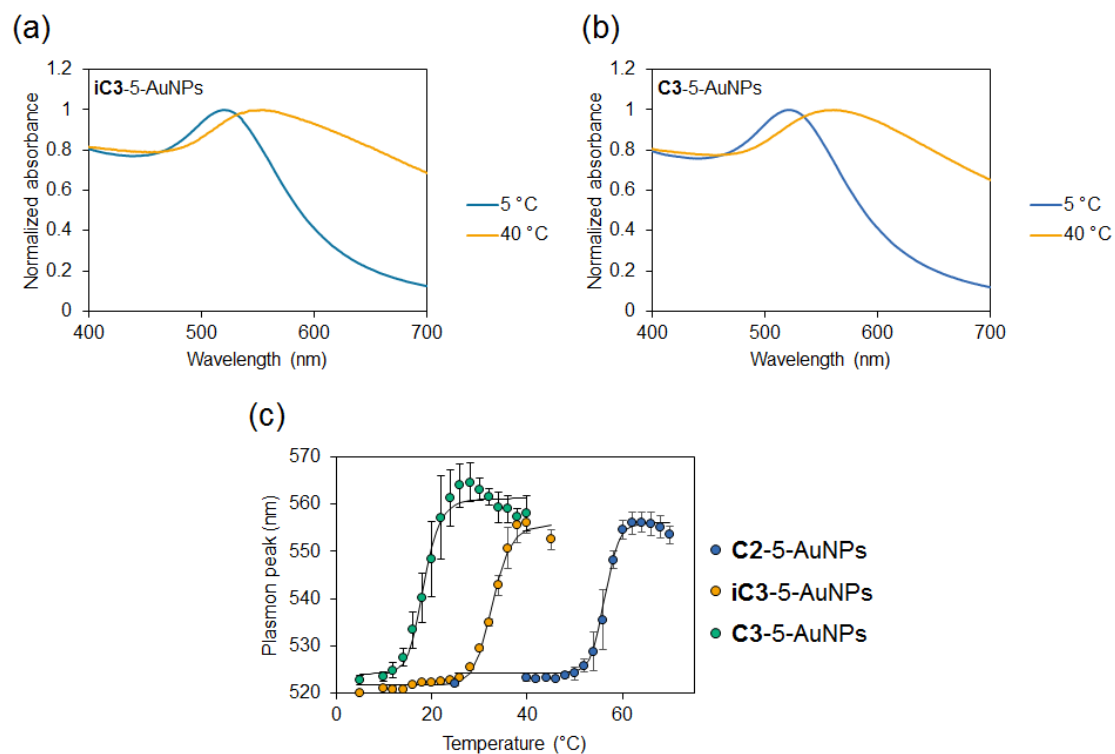


Figure 3-11. (a, b) Normalized optical absorption spectra of (a) iC3- and (b) C3-5-AuNPs at 5 °C (blue) and 40 °C (orange). Temperature-dependent plasmon peak shifts of C2- (blue), iC3- (orange), and C3-5-GNSs (green) between 5 and 70 °C.

3-3-4. Effects of GNS size

Nanoparticle size is one of the most important parameters that determine the interparticle interaction. However, for the thermoresponsive assembly of GNSs, the study of the effect of nanoparticle size on the T_A is still limited.²¹ Therefore, to investigate the effects of GNS size on thermoresponsive assembly in more detail, I synthesized 3.3-nm GNSs modified with the **C2-E6C11** ligand, referred to as **C2-3-GNSs**. The detailed analysis of **C2-3-AuNPs** is shown in Figure 3-12. 10-nm GNSs modified with **C2** ligand, referred to as **C2-10-GNSs**, were prepared via ligand exchange reaction, in the same way as the 5-nm GNSs. The extinction spectra of **C2-3-** and **C2-10-GNSs** are shown in Figure 3-13a and b. The normalized maximum wavelength as a function of temperature for **C2-3-**, **C2-5-**, and **C2-10-GNSs** is shown in Figure 3-13c. The assembly temperatures of **C2-3-**, **C2-5-**, and **C2-10-GNSs** were 67, 56, and 39°C, respectively. Although the same ligand was used, the assembly temperatures differed notably with nanoparticle size. It has been reported that higher concentration of nonionic surfactants (a surfactant weight fraction of 0.1-0.5) showed higher clouding points.⁴² The ligand densities on the surface of different sized GNSs were determined by ICP-AES. From the ratio of the Au to S atoms obtained by ICP-AES, the ligand densities of **C2-3-**, **C2-5-**, and **C2-10-GNSs** were found to be 7.5, 4.7, 6.1 ligands/nm² (in a weight fraction range of 0.25-0.5), respectively (Table 3-3). These calculated ligand densities were in good agreement with those in previous reports (3-7 ligands/nm²),^{41,42} and were relatively independent of GNS size. This result indicates that the local concentration of the ligand on larger GNS surface, which was estimated from the free volume (Figure 3-14), is higher than that on smaller one; in other words, GNSs with a higher ligand local concentration showed a lower T_A . Interestingly, this trend is inconsistent with the concentration dependency of the nonionic surfactant.³⁰

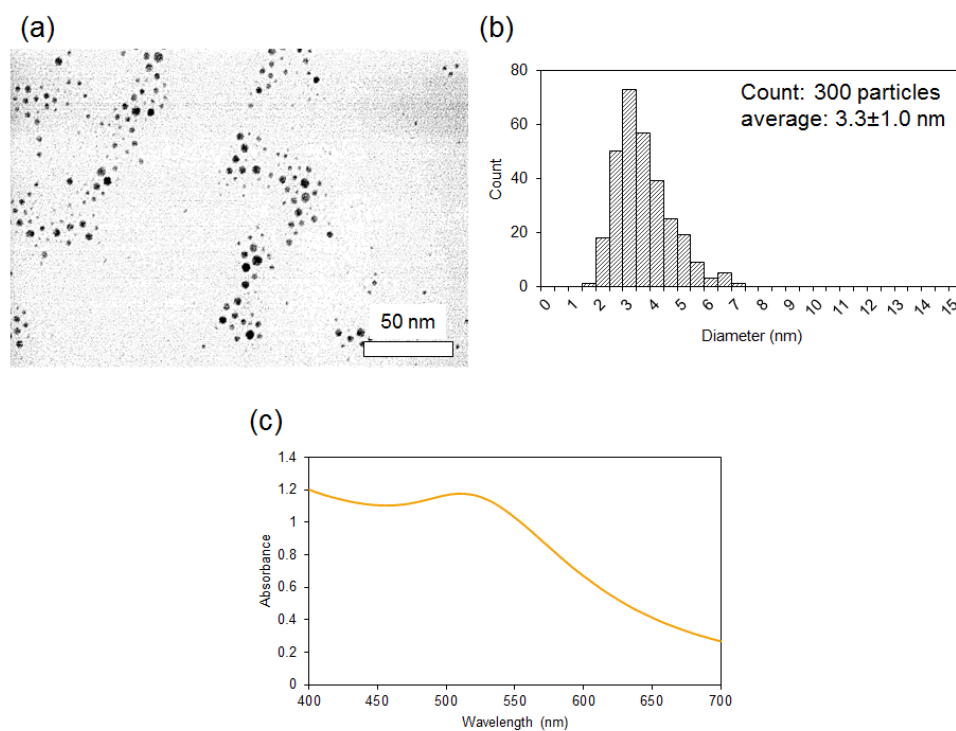


Figure 3-12. Characterization of C2-3-AuNPs using STEM and UV-Vis spectroscopy. (a) STEM image and (b) size distribution (300 counts). The size was 3.3 ± 1.0 nm. (c) Absorption spectrum of C2-3-AuNPs in water at 25 °C.

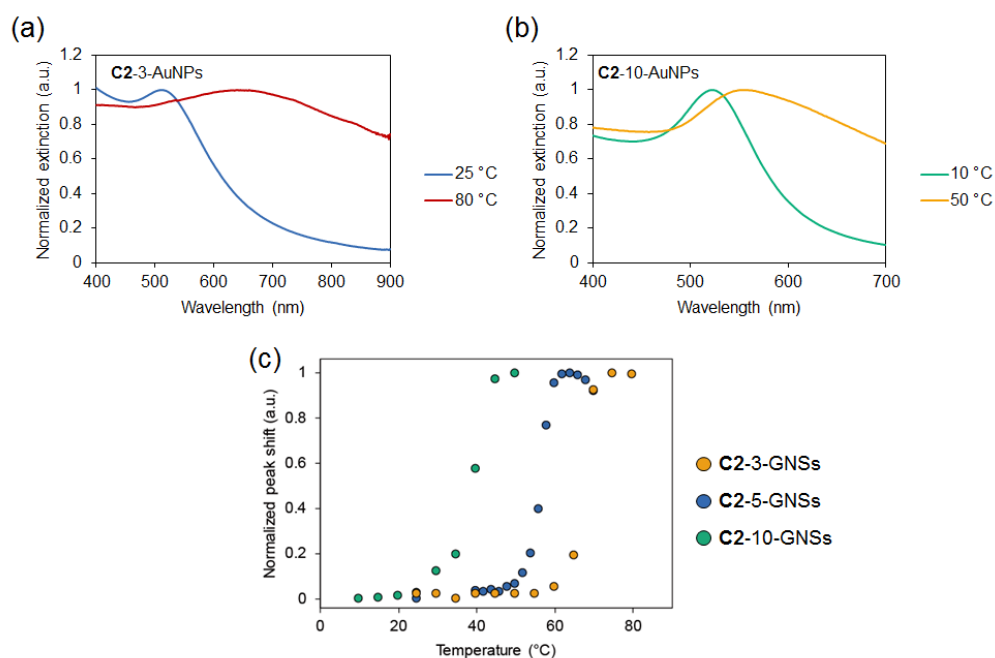
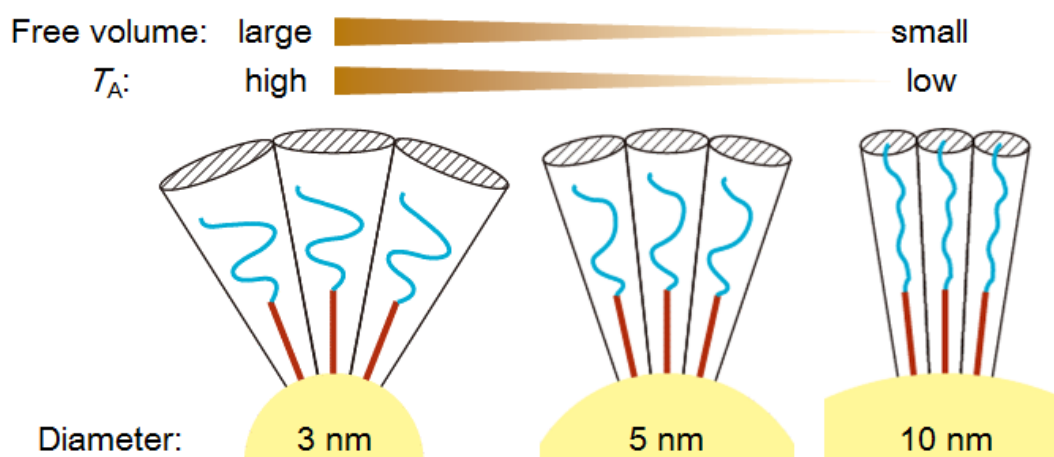


Figure 3-13. Temperature-dependent changes in the normalized peak shift of C2-3- (orange), C2-5- (blue), and C2-10-GNSs (green).

Table 3-3. Ligand densities on the GNS surface as determined by ICP-AES.

<i>Sample</i>	<i>Ligand density on GNS surface (Ligands/nm²)</i>
C2-3-GNSs	7.5 ± 0.27
C2-5-GNSs	4.7 ± 0.28
sC2-5-GNSs	4.8 ± 0.25
C2-10-GNSs	6.1 ± 0.81

**Figure 3-14.** Schematic illustration of the relationship between T_A and free volume for one surface ligand molecule on different sized GNSs.

When the particle size increases, the free volume (occupied volume) for a single **C2-E6C11** ligand becomes smaller (Figure 3-14).²¹ This means that HEG moieties on a larger GNS would be more structurally restricted due to the smaller free volume compared with those bound on smaller GNSs. Lequeux *et al.* reported that the smaller curvature induced a compression and a stretching of the polymer chains on the GNS surface.²¹ From my findings, I speculate that the effect of size on the T_A suggests that the release of hydrated waters bound to the HEG moiety depends on the structure of the HEG. When the HEG moiety was conformationally restricted (i.e., when the free volume was limited as on GNSs of a large size), hydrated waters are more easily detached compared to those bound to less conformationally restricted HEGs on smaller GNSs. In addition, the more densely packed alkyl-head moieties on larger GNSs might disturb the hydration network around the HEG moiety. The smaller free volume would induce a decrease of the hydration state, resulting in a lowering dehydration temperature and consequent T_A .

As another hypothesis, I need to consider van der Waals (vdW) attraction dependent on GNS diameter. That is, I can explain that assembly of larger GNSs with higher vdW attraction occurs with a small amount of dehydration if the dehydration occurs in a wide temperature range. The size of the effect of vdW attraction remains unclear. This point will be discussed again in Chapter 4.

3-3-5. Effect of alkyl tail length

I investigated the effect of the alkyl tail length on the thiol group side. In the previous sections, I mentioned that alkyl heads exposed on the outermost surface influenced the T_A and the effect of the hydrophobic part of the undecanethiol tail was diminished by attachment on the surface of the GNSs. Hence, I synthesized an ethyl-headed ligand with a shorter alkyl linker on the thiol group side (referred to as the **C2-E6C3** ligand, Scheme 3-1). Here, the GNSs coated with **C2-E6C3** were **sC2-GNSs**. I had expected that **sC2-5-GNSs** would have a similar T_A to **C2-5-GNSs**. Figure 10 shows the transmittance vs. temperature plots for the free **C2-E6C3** ligand and the temperature-dependent plasmon peak shift for **sC2-5-GNSs** in 5 mM NaCl solution. Interestingly, the **sC2-5-GNSs** provided a clear plasmon peak shift upon heating in 5 mM NaCl solution, rather than pure water. Even though the ligand itself does not show a clouding point in the range from 15 to 80°C (blue dots in Figure 3-15), their grafting on GNSs afforded assembly behavior. This means that the part of the ligand displayed on the outermost surface of the GNSs is important in determination of thermoresponsive behavior. While the **sC2-5-GNSs** assembled at 37°C (red dots in Figure 3-15), unexpectedly, this T_A was much smaller than that of the **C2-5-GNSs** (56°C). There are two possibilities, as with size, effect to explain the difference in the aggregation temperature between **sC2-5-GNSs** and **C2-5-GNSs**. The first possibility is the effect of the free volume, which is discussed in the previous section; Effects of GNS size. ICP measurement shows that the ligand densities of **C2-5-GNSs** and **sC2-5-GNSs** are almost the same (Table 3-3), so that the HEG portion of the **C2-E6C3** ligand on the surface has a smaller free volume than that of the **C2-E6C3** ligand (schematic illustration is shown in Figure 3-16). The second possibility is the change in vdW attraction between GNSs. The lower T_A for **sC2-5-GNS**

compared with C2-5-GNS can be explained by the shorter distance of the effective steric repulsion of the C2-E6C3 ligand, which cannot counterbalance the vdW attraction. Currently, I cannot conclude in detail the mechanism underlying the tail length effect; however, it is intriguing that the C2-E6C3 ligand which did not have a clouding point in a free state, induced thermoresponsive assembly on immobilization on the GNS surface.

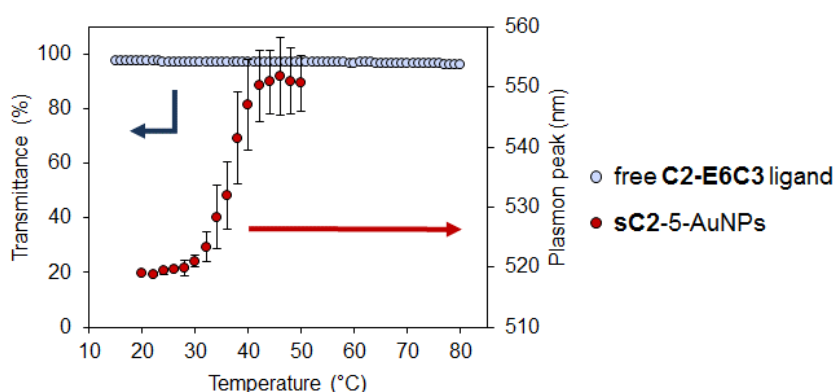


Figure 3-15. Transmittance vs. temperature for aqueous solutions of C2-E6C3 (blue dots) and temperature-dependent changes in the plasmon peak of sC2-5-GNSs (red dots). [C2-E6C3] = 10 mM, [sC2-5-GNSs] = 80 nM. Both experiments were performed in water containing 5 mM NaCl.

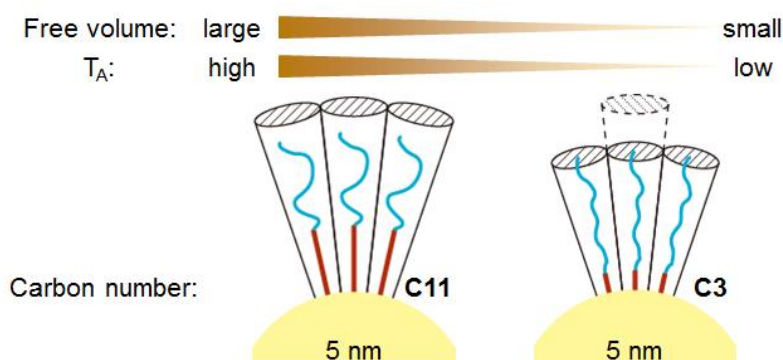


Figure 3-16. Schematic illustration of the relationship between T_A and free volume for one surface ligand molecule with different tail lengths.

3-4. Conclusion

I synthesized a series of alkyl-headed HEG-undecanethiol as surface ligands and prepared GNSs coated with a self-assembled monolayer of these ligands. GNSs coated with alkyl-headed HEG derivatives showed thermoresponsive behavior; i.e., assembly and disassembly in an aqueous solution in a response to temperature change. I found that alkyl heads, GNS size, and the length of alkyl tail influenced T_A . Slight changes in the alkyl-head structure (ethyl, iso-propyl, and propyl) caused large shifts in the T_A . The size of the GNSs was also critical to the T_A , suggesting that the degree of hydration of the HEG part depends on the free volume of the HEG parts, which is in turn determined by the curvature of the GNSs. These data demonstrated that thermal responsiveness of the HEG-based GNSs is very sensitive to both the hydrophobicity of the alkyl head and the diameter of the GNSs, indicates that the T_A is widely controllable by changes in the alkyl head and nanoparticle size. Additionally, the ligand with shorter alkyl tail length afforded thermoresponsive behavior on immobilization on the GNS surface, even though the free ligand itself did not have a clouding point. This SAM-based approach to the construction of thermoresponsive GNSs is both simple and versatile compared to the use of conventional thermoresponsive polymers. Therefore, this approach could provide new guidelines for the design of functional nanoparticles with stimuli-responsive properties.

3-5. References

- (1) Qian, Z.; Ginger, D. S. Reversibly Reconfigurable Colloidal Plasmonic Nanomaterials. *J. Am. Chem. Soc.* **2017**, *139*, 5266–5276.
- (2) Liu, Y.; Han, X.; He, L.; Yin, Y. Thermoresponsive Assembly of Charged Gold Nanoparticles and Their Reversible Tuning of Plasmon Coupling. *Angew. Chem. Int. Ed.* **2012**, *51*, 6373–6377.
- (3) Housni, A.; Zhao, Y. Gold Nanoparticles Functionalized with Block Copolymers Displaying Either LCST or UCST Thermosensitivity in Aqueous Solution. *Langmuir* **2010**, *26*, 12933–12939.
- (4) Tian, Z.; Yang, C.; Wang, W.; Yuan, Z. Shieldable Tumor Targeting Based on pH Responsive Self-Assembly / Disassembly of Gold Nanoparticles. *ACS Appl. Mater. Interfaces* **2014**, *6*, 17865–17876.
- (5) Song, J.; Zhou, J.; Duan, H. Self-Assembled Plasmonic Vesicles of SERS-Encoded Amphiphilic Gold Nanoparticles for Cancer Cell Targeting and Traceable Intracellular Drug Delivery. *J. Am. Chem. Soc.* **2012**, *134*, 13458–13469.
- (6) Orendorff, C. J.; Hankins, P. L.; Murphy, C. J. pH-Triggered Assembly of Gold Nanorods. *Langmuir* **2005**, *21*, 2022–2026.
- (7) Kundu, P. K.; Samanta, D.; Leizrowice, R.; Margulis, B.; Zhao, H.; Börner, M.; Udayabhaskararao, T.; Manna, D.; Klajn, R. Light-Controlled Self-Assembly of Non-Photoresponsive Nanoparticles. *Nat. Chem.* **2015**, *7*, 646–652.
- (8) Klajn, R.; Bishop, K. J. M.; Grzybowski, B. A. Light-Controlled Self-Assembly of Reversible and Irreversible Nanoparticle Suprastructures. *Proc. Natl. Acad. Sci. U. S. A.* **2007**, *104*, 10305–10309.
- (9) Holmes, A. M.; Song, Z.; Moghimi, H. R.; Roberts, M. S. Relative Penetration of Zinc Oxide and Zinc Ions into Human Skin after Application of Different Zinc Oxide Formulations. *ACS Nano* **2016**, *10*, 1810–1819.
- (10) Kim, Y.; Johnson, R. C.; Hupp, J. T. Gold Nanoparticle-Based Sensing of “Spectroscopically Silent” Heavy Metal Ions. *Nano Lett.* **2001**, *1*, 165–167.

- (11) Du, J.; Zhu, B.; Chen, X. Urine for Plasmonic Nanoparticle-Based Colorimetric Detection of Mercury Ion. *Small* **2013**, *9*, 4104–4111.
- (12) Liu, F.; Agarwal, S. Thermoresponsive Gold Nanoparticles with Positive UCST-Type Thermoresponsivity. *Macromol. Chem. Phys.* **2015**, *216*, 460–465.
- (13) Durand-Gasselin, C.; Koerin, R.; Rieger, J.; Lequeux, N.; Sanson, N. Colloidal Stability of Zwitterionic Polymer-Grafted Gold Nanoparticles in Water. *J. Colloid Interface Sci.* **2014**, *434*, 188–194.
- (14) Zhu, M. Q.; Wang, L. Q.; Exarhos, G. J.; Li, A. D. Q. Thermosensitive Gold Nanoparticles. *J. Am. Chem. Soc.* **2004**, *126*, 2656–2657.
- (15) Chakraborty, S.; Bishnoi, S. W.; Pérez-Luna, V. H. Gold Nanoparticles with poly(N -Isopropylacrylamide) Formed via Surface Initiated Atom Transfer Free Radical Polymerization Exhibit Unusually Slow Aggregation Kinetics. *J. Phys. Chem. C* **2010**, *114*, 5947–5955.
- (16) Yusa, S.; Fukuda, K.; Yamamoto, T.; Iwasaki, Y.; Watanabe, A.; Akiyoshi, K.; Morishima, Y. Salt Effect on the Heat-Induced Association Behavior of Gold Nanoparticles Coated with Poly(N -Isopropylacrylamide) Prepared via Reversible Addition–Fragmentation Chain Transfer (RAFT) Radical Polymerization. *Langmuir* **2007**, *23*, 12842–12848.
- (17) Shan, J.; Zhao, Y.; Granqvist, N.; Tenhu, H. Thermoresponsive Properties of N-Isopropylacrylamide Oligomer Brushes Grafted to Gold Nanoparticles: Effects of Molar Mass and Gold Core Size. *Macromolecules* **2009**, *42*, 2696–2701.
- (18) Beija, M.; Marty, J.-D.; Destarac, M. Thermoresponsive poly(N-Vinyl Caprolactam)-Coated Gold Nanoparticles: Sharp Reversible Response and Easy Tunability. *Chem. Commun.* **2011**, *47*, 2826.
- (19) Zábó, D.; Radnóczy, G. Z.; Deák, A. Preparation of Compact Nanoparticle Clusters from Polyethylene Glycol-Coated Gold Nanoparticles by Fine-Tuning Colloidal Interactions. *Langmuir* **2015**, *31*, 2662–2668.
- (20) Boyer, C.; Whittaker, M. R.; Luzon, M.; Davis, T. P. Design and Synthesis of Dual Thermoresponsive and Antifouling Hybrid Polymer/gold Nanoparticles. *Macromolecules* **2009**, *42*, 6917–6926.

- (21) Durand-Gasselín, C.; Capelot, M.; Sanson, N.; Lequeux, N. Tunable and Reversible Aggregation of Poly(ethylene Oxide-St-Propylene Oxide) Grafted Gold Nanoparticles. *Langmuir* **2010**, *26*, 12321–12329.
- (22) Huang, X.; El-Sayed, I. H.; Qian, W.; El-Sayed, M. A. Cancer Cell Imaging and Photothermal Therapy in the near-Infrared Region by Using Gold Nanorods. *J. Am. Chem. Soc.* **2006**, *128*, 2115–2120.
- (23) Li, X.; Takashima, M.; Yuba, E.; Harada, A.; Kono, K. PEGylated PAMAM Dendrimer-Doxorubicin Conjugate-Hybridized Gold Nanorod for Combined Photothermal-Chemotherapy. *Biomaterials* **2014**, *35*, 6576–6584.
- (24) Salmaso, S.; Caliceti, P.; Amendola, V.; Meneghetti, M.; Magnusson, J. P.; Pasparakis, G.; Alexander, C. Cell up-Take Control of Gold Nanoparticles Functionalized with a Thermoresponsive Polymer. *J. Mater. Chem.* **2009**, *19*, 1608.
- (25) Roy, D.; Brooks, W. L.; Sumerlin, B. S. New Directions in Thermoresponsive Polymers. *Chem. Soc. Rev.* **2013**, *42*, 7214–7243.
- (26) Kenkare, P. U.; Hall, C. K. Modeling of Phase Separation in PEG–salt Aqueous Two-Phase Systems. *AIChE J.* **1996**, *42*, 3508–3522.
- (27) Hey, M. J.; Stephen, M.; Davidson, G. Temperature on Poly(ethylene Oxide) Chains in Aqueous Solution. *J. Chem. Soc. Faraday Trans* **1995**, *91*, 3897–3900.
- (28) Malcolm G, R. J. The Thermodynamic Properties of Aqueous Solutions of Polyethylene Glycol, Polypropylene Glycol and Dioxane. *Trans. Faraday Soc.* **1957**, *53*, 921–931.
- (29) Kobayashi, K.; Yamada, S.; Nagaoka, K.; Kawaguchi, T.; Osa, M.; Yoshizaki, T. Characterization of Linear Poly(N-Isopropylacrylamide) and Cloud Points in Its Aqueous Solutions. *Polym. J.* **2009**, *41*, 416–424.
- (30) Inoue, T.; Ohmura, H.; Murata, D. Cloud Point Temperature of Polyoxyethylene-Type Nonionic Surfactants and Their Mixtures. *J. Colloid Interface Sci.* **2003**, *258*, 374–382.
- (31) Claesson, P. M.; Kjellander, R.; Stenius, P.; Christenson, H. K. Direct

- Measurement of Temperature-Dependent Interactions between Non-Ionic Surfactant Layers. *J. Chem. Soc. Faraday Trans. 1* **1986**, *82*, 2735–2746.
- (32) Love, J. C.; Estroff, L. A.; Kriebel, J. K.; Nuzzo, R. G.; Whitesides, G. M. Self-Assembled Monolayers of Thiolates on Metals as a Form of Nanotechnology. *Chem. Rev.* **2005**, *105*, 1103–1169.
- (33) Yamada, R.; Uosaki, K. In Situ Scanning Tunneling Microscopy Observation of the Self-Assembly Process of Alkanethiols on Gold(111) in Solution. *Langmuir* **1998**, *14*, 855–861.
- (34) Peptides, B. C.; Oh, E.; Delehanty, J. B.; Sapsford, K. E.; Susumu, K.; Goswami, R.; Blanco-canosa, J. B.; Dawson, P. E.; Granek, J.; Shoff, M.; Zhang, Q.; Goering, P. L.; Huston, A.; Medintz, I. L. Cellular Uptake and Fate of PEGylated Gold Nanoparticles Is Dependent on Particle Size. *ACS Nano* **2011**, *5*, 6434–6448.
- (35) Kanaras, A. G.; Kamounah, F. S.; Schaumburg, K.; Kiely, C. J.; Brust, M. Thioalkylated Tetraethylene Glycol: A New Ligand for Water Soluble Monolayer Protected Gold Clusters. *Chem. Commun.* **2002**, No. 20, 2294–2295.
- (36) Yada, S.; Suzuki, T.; Hashimoto, S.; Yoshimura, T. Adsorption and Aggregation Properties of Homogeneous Polyoxypropylene-Polyoxyethylene Alkyl Ether Type Nonionic Surfactants. *Langmuir* **2017**, *33*, 3794–3801.
- (37) Helm, C. A.; Israelachvili, J. N.; McGuiggan, P. Role of Hydrophobic Forces in Bilayer Adhesion and Fusion. *Biochemistry* **1992**, *31*, 1794–1805.
- (38) Wang, X.; Qiu, X.; Wu, C. Comparison of the Coil-to-Globule and the Globule-to-Coil Transitions of a Single Poly(N -Isopropylacrylamide) Homopolymer Chain in Water. *Macromolecules* **1998**, *31*, 2972–2976.
- (39) Kurzhals, S.; Zirbs, R.; Reimhult, E. Synthesis and Magneto-Thermal Actuation of Iron Oxide Core–PNIPAM Shell Nanoparticles. *ACS Appl. Mater. Interfaces* **2015**, *7*, 19342–19352.
- (40) Lutz, J. F.; Akdemir, Ö.; Hoth, A. Point by Point Comparison of Two Thermosensitive Polymers Exhibiting a Similar LCST: Is the Age of poly(NIPAM) Over? *J. Am. Chem. Soc.* **2006**, *128*, 13046–13047.

- (41) Torelli, M. D.; Putans, R. A.; Tan, Y.; Lohse, S. E.; Murphy, C. J.; Hamers, R. J. Quantitative Determination of Ligand Densities on Nanomaterials by X-Ray Photoelectron Spectroscopy. *ACS Appl. Mater. Interfaces* **2015**, 7, 1720–1725.
- (42) Hinterwirth, H.; Kappel, S.; Waitz, T.; Prohaska, T.; Lindner, W.; Lämmerhofer, M. Quantifying Thiol Ligand Density of Self-Assembled Monolayers on Gold Nanoparticles by Inductively Coupled Plasma-Mass Spectrometry. *ACS Nano* **2013**, 7, 1129–1136.

Chapter 4

*Two-step Assembly of Thermoresponsive Gold Nanorods
Coated with a Single Kind of Ligand*

4-1. Introduction

Self-assembly, as a typical bottom-up system, is a powerful technique for the fabrication of 1D, 2D, and 3D nanostructures.^{1,2} Recently, the fabrication of hierarchical structures has been one of the hottest subjects in material sciences due to their potential functionalities.³⁻⁷ To date, however, only a few hierarchical structures fabricated *via* multi-step assembly in solution, similar to the quaternary structures of proteins composed of several tertiary structures, have been reported.^{8,9} These hierarchical assemblies were made by varying the polarity of the solvent. However, the reversibility of the multi-step assembly process has not been exploited sufficiently. For the fabrication of sophisticated assemblies with dynamic structural changes, hierarchical structures composed of nanoparticles require controllable reversibility of assembly/disassembly in response to changes in the environment,¹⁰ such as temperature,¹¹⁻¹⁶ pH,¹⁷⁻¹⁹ and light.^{20,21}

The fabrication of sophisticated assembled structures has relied on site-specific modification using several kinds of ligand.²² In Chapter 2, Janus-like GNSs with hydrophobic and hydrophilic faces were synthesized. Furthermore, anisotropic-shaped nanoparticles with site-specific modification have been developed by other groups.²³⁻²⁵ Kumacheva *et al.* synthesized the GNRs coated with CTAB along their long face and with polystyrene at the edge, forming rings, chains, and capsules structures as assemblies depending on the solvent.^{26,27} Although complex surface modification could provide sophisticated structures, the intricate steps necessary for the surface modification impede the progress of the artificially programmed self-assembly of nanoparticles. Therefore, a simple approach is desired for the establishment of the guidelines for reversible multi-step assembly.

In Chapter 3, The GNSs covered with alkyl-headed hexa(ethylene glycol) (HEG)

derivatives (Figure 4-1a) showed reversible thermoresponsive assembly behavior driven by the dehydration of the HEG part. Additionally, I found that the assembly temperature decreased as the GNS diameter increased; that is, the free volume of a single ligand on the surface, which depended on the curvature affected the temperature at which dehydration occurred. Thus, it is expected that dehydration from ligand molecules on the nanoparticles with an anisotropic shape occurs at different temperatures depending on their position, even when a single kind of ligand used. Here, I focused on the curvature of nanoparticles to perform allow reversible multi-step assembly through a simple approach. In the case of proteins, information for folding is programmed to a primary structure as only chemical structures of 20 amino acids. Free volume of a ligand is information for self-assembly unique to nanoparticles.

In this Chapter 4, I show the reversible thermoresponsive two-step assembly of GNRs as a representative anisotropic nanoparticle. The GNRs have different curvatures between the side and edge portions; the ligands bound on the side (side-ligands) have smaller free volume than the ligands bound on the edge (edge-ligands) (Figure 4-1b). As the dehydration temperature decreased with the decrease in the free volume of a single ligand on the GNR surface, the GNRs covered with the HEG derivatives first formed side-by-side assembly first through the dehydration of the side-ligands upon heating, and subsequent structural change was induced by further dehydration of the edge-ligands (Figure 4-1c). This is a new approach to the fabrication of hierarchical structures based on a reversible two-step assembly process using GNRs through simple surface modification with a single kind of ligand.

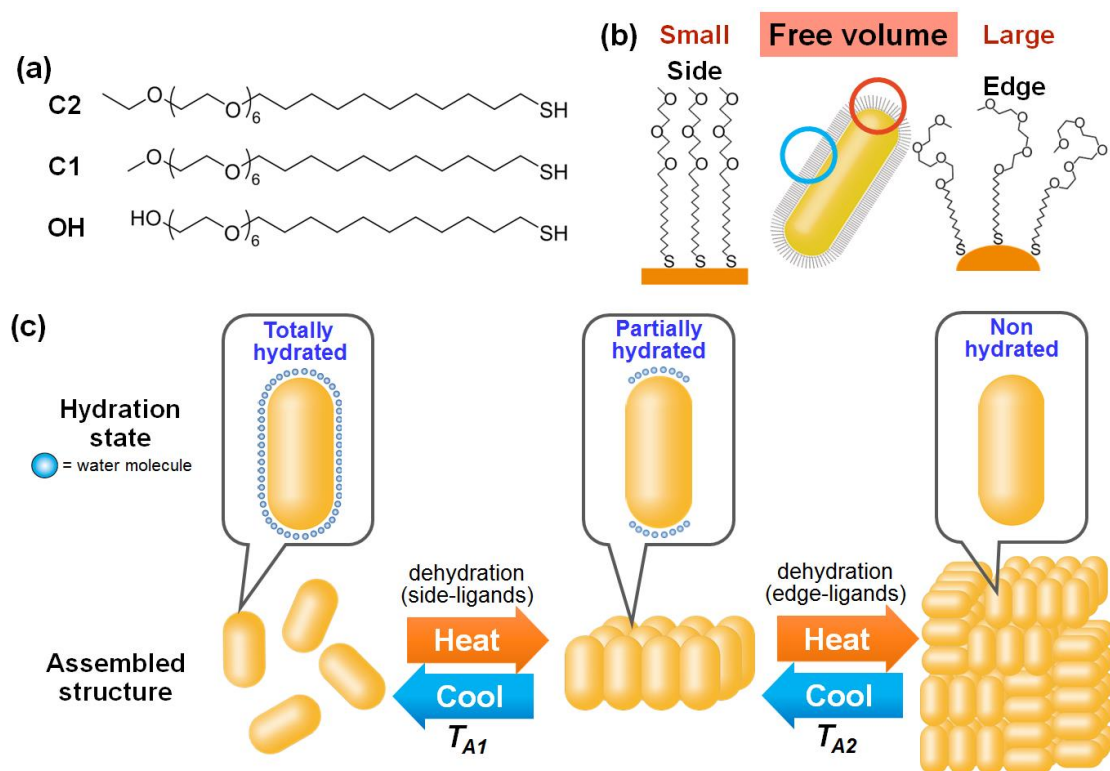


Figure 4-1. (a) Chemical structures of the HEG derivatives used in this study. (b) Schematic illustration of the ligands immobilized on the GNR surface. (c) Hydration states and assembled structures of GNRs upon heating. The temperature for the first and second assemblies is defined as T_{A1} and T_{A2} , respectively.

4-2. Experimental section

4-2-1. Materials

HAuCl₄·3H₂O was purchased from Acros Organics (USA). Hexadecyltrimethylammonium bromide (CTAB) (>98.0%), NaBH₄ (>95.0%), sodium 3-methylsalicylate, (>97.0%) were purchased from Tokyo Chemical Industry Co., Ltd. (Japan). 1.0 mol/L NaOH were purchased from Wako Pure Chemical Industries (Japan). Ultrapure water (18.2 MΩ cm⁻¹, Milli-Q, Millipore, USA) was used for all solution preparations and experiments. GNRs [33 x 14 nm, 33 x 8 nm, and 54 x 15 nm; hereafter referred to as GNRs(33x14), GNRs(33x8), and GNRs(54x15), respectively] were synthesized *via* a seed-mediated process according to previous reports.^{28,29}

4-2-2. The synthesis and characterization of GNRs coated with CTAB

• Synthesis of GNRs(33x14)²⁸

To prepare the seed solution, 0.36 g of CTAB was dissolved in 5 mL of water in a 50-mL plastic tube. Five mL of 0.5 mM HAuCl₄ was added to the CTAB solution. Then, 0.6 mL of fresh ice-cold 6 mM NaBH₄ aqueous solution was injected into the Au(III)–CTAB solution under vigorous stirring. The color of the solution immediately changed from pale yellow to brown. The stirring was stopped after 2 min. The seed solution was used in the growth step after incubation for 30 min at 30°C. For preparation of the growth solution, CTAB (0.18 g) and sodium 3-methylsalicylate (0.22 g) were dissolved in 50 mL of warm water (70°C) in a 200 mL Erlenmeyer flask. The compounds were completely dissolved by ultrasonic irradiation. The solution was cooled to 30°C, and then, 4 mM AgNO₃ solution was added. The mixture was kept undisturbed at 30°C for 15 min, after

which 50 mL of 1 mM HAuCl₄ solution was added. After 15 min of gentle stirring, 200 μL of ascorbic acid (64 mM) was added, and the solution was vigorously stirred for 30 sec. Finally, 0.16 mL of seed solution was injected into the solution. The resultant mixture was stirred for 30 seconds and left undisturbed at 30°C for 12 hours for GNR growth.

- **Synthesis of GNRs(33x8) and GNRs(54x15)**²⁹

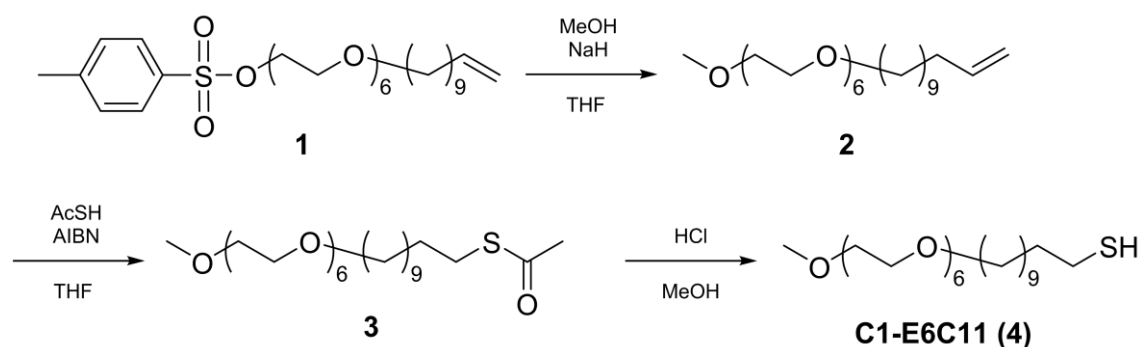
For the preparation of the seed solution, an aqueous 0.01 M HAuCl₄ solution (250 μL) was added to 0.1 M CTAB *aq.* (7.5 mL) in a 50-mL plastic tube. Freshly prepared 0.01 M ice-cold NaBH₄ *aq.* (600 μL) was added to the mixture at once and gently shaken. Then, the mixture was kept undisturbed at 30°C for 4 hours.

Then, for the seed-growth step for the synthesis of GNRs(33x8), 95 mL of 100 mM CTAB *aq.*, 4 mL of 10 mM HAuCl₄ *aq.*, 600 μL of 10 mM AgNO₃ *aq.*, and 650 μL of 100 mM ascorbic acid *aq.* were added in that order, one by one, to a 100-mL plastic tube. After the addition of the ascorbic acid *aq.*, the color of the solution changed from a dark yellow to colorless. Then, 2 mL of seed solution was added to the reaction mixture and mixed gently for 10 seconds. The solution was kept undisturbed at 30°C overnight and the color of the solution turned brown.

To synthesize GNRs(54x15), 76 mL of 100 mM CTAB *aq.*, 5 mL of 10 mM HAuCl₄ *aq.*, 700 μL of 10 mM AgNO₃ *aq.*, and 540 μL of 0.1 M ascorbic acid *aq.* were added in that order, one by one, to a 100-mL plastic tube. Then, 200 μL of seed solution was added to the reaction mixture and mixed for 10 seconds. The solution was kept undisturbed at 30°C overnight and the color of the solution turned brown. The reaction products were isolated by centrifugation at 7000 g for 20 min followed by removal of the supernatant (about 80 mL). Ultra pure water was added to the solution up to 10 mL.

- **Synthesis of C1-E6C11**

Scheme 4-1. Synthetic route to C1-E6C11.



2,5,8,11,14,17,20-heptaoxahentriacont-30-ene (2). Methanol (20 mL) was cooled on ice and added the 60% NaH in oil (0.43 g, 1.1×10^{-2} mol) under N_2 atmosphere. After H_2 gas generation, compound **1** (see Chapter 3) in MeOH (10 mL) was added dropwise. The reaction was allowed to warm to room temperature and stirred overnight. The solvent was removed by evaporation under a reduced pressure. The residue was dissolved in CHCl_3 and washed twice with sat. NaCl solution. The organic layer was dried over anhydrous Na_2SO_4 . The crude product was evaporated under vacuum and purified by flash chromatography on silica gel (2:8 $\text{CHCl}_3/\text{EtOAc}$ to EtOAc) to yield **2** as a clear syrup (0.49 g, 51%).

^1H NMR (400 MHz, CDCl_3): δ /ppm = 1.22-1.44 (m, 14H, alkyl chain), 1.50-1.62 (m, 4H, alkyl chain), 2.04 (q, 2H, $J = 7.8$ Hz, 7.3 Hz, $=\text{CH}-\text{CH}_2-\text{CH}_2$), 3.38 (s, 3H, $\text{CH}_3-\text{O}-$), 3.44 (t, 2H, $J = 6.9$ Hz, $-\text{O}-\text{CH}_2-$), 3.52-3.76 (m, 24H, $-\text{O}-\text{CH}_2-$), 4.89-5.03 (m, 2H, $-\text{CH}=\text{CH}_2$), 5.75-5.88 (m, 1H, $-\text{CH}=\text{CH}_2$)

S-2,5,8,11,14,17,20-heptaoxahentriacontan-31-yl ethanethioate (3). Compound **2** (0.35 g, 7.8×10^{-4} mol), AcSH (0.30 g, 3.9×10^{-3} mol), and 2,2'-azobisisobutyronitrile

(0.13 g, 7.8×10^{-4} mol) were dissolved in stabilizer free dry THF (20 mL). The mixture was refluxed for 4 hours. The solvent was removed, the residue was dissolved in CHCl_3 and washed twice with sat. NaCl solution. The organic layer was dried over anhydrous Na_2SO_4 . The crude product was concentrated *in vacuo* and purified by flash chromatography on silica gel (3:7 $\text{CHCl}_3/\text{EtOAc}$ to 1:9 $\text{CHCl}_3/\text{EtOAc}$) to yield **3** (0.26 g, 68 %) as a clear syrup.

^1H NMR (400 MHz, CDCl_3): δ /ppm = 1.18-1.40 (m, 14H, alkyl chain), 1.49-1.63 (m, 4H, alkyl chain), 2.32 (s, 3H, $\text{CH}_3\text{-C(=O)-}$), 2.85 (t, 2H, $J = 7.4$ Hz, $\text{-CH}_2\text{-S-}$), 3.45 (t, 4H, $J = 5.5$ Hz, $\text{-O-CH}_2\text{-}$), 3.38 (s, 3H, $\text{CH}_3\text{-O-}$), 3.44 (t, 2H, $J = 6.8$ Hz, $\text{-O-CH}_2\text{-}$), 3.51-3.71 (m, 24H, $\text{-O-CH}_2\text{-}$)

2,5,8,11,14,17,20-heptaohentriacontane-31-thiol (4, C1). Compound **3** (0.10 g, 1.9×10^{-4} mol) was dissolved in methanol (20 mL) and conc. HCl (175 μL) was added to the solution. The mixture was refluxed for 12 hours. The solvent was removed, the residue was dissolved in CHCl_3 and washed twice with sat. NaCl solution. The organic layer was dried over anhydrous Na_2SO_4 . The crude product was evaporated under vacuum and purified by flash chromatography on silica gel (2:8 $\text{CHCl}_3/\text{EtOAc}$) to yield **4** (78 mg, 85%) as a clear syrup.

^1H NMR (400 MHz, CDCl_3): δ /ppm = 1.19-1.43 (m, 15H, alkyl chain and -SH), 1.51-1.68 (m, 4H, alkyl chain), 2.52 (q, 2H, $J = 7.5$ Hz, $\text{-CH}_2\text{-SH}$), 3.38 (s, 3H, $\text{CH}_3\text{-O-}$), 3.44 (t, 2H, $J = 6.6$ Hz, $\text{-O-CH}_2\text{-}$), 3.52-3.70 (m, 24H, $\text{-O-CH}_2\text{-}$)

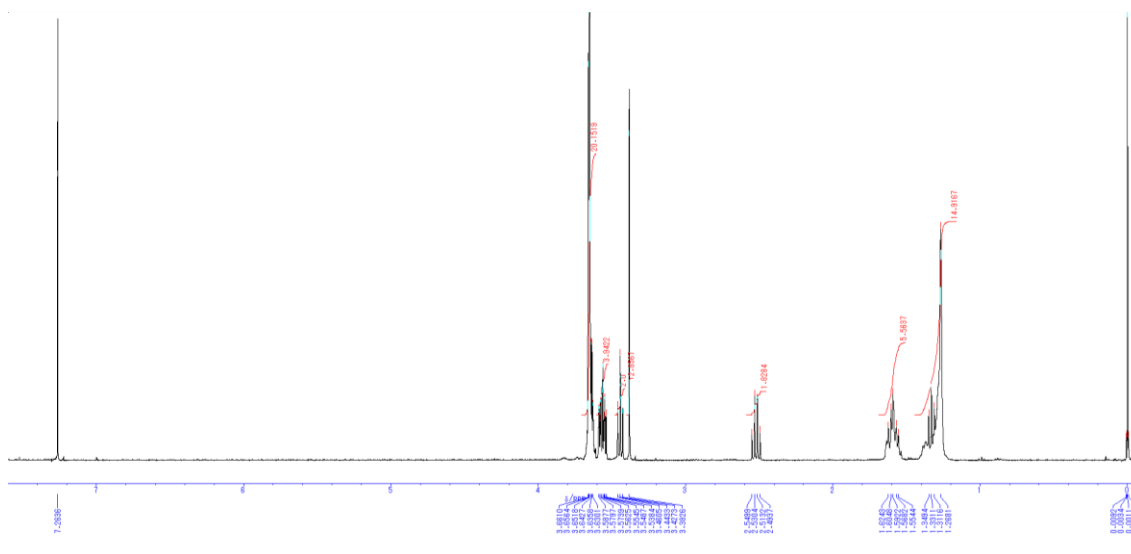


Figure 4-2. ^1H NMR spectrum of C1-E6C11

4-2-3. Surface modification of GNRs

The as-prepared CTAB-protected GNRs dispersion (500 μL) was purified by centrifugation [GNRs(33x14): 7,000 g for 20 min; GNRs(33x8): 12,000 g for 40 min; GNRs(54x15): 6,000 g for 10 min] and the supernatant removed (480 μL). Pure water (67.5 μL) and 40 mM ligand aqueous solution (12.5 μL) were added to the concentrated GNR solution to a final volume of 100 μL , and a final ligand concentration of 5 mM. The reaction solution was shaken using a Cute Mixer CM-1000 (Tokyo Rikakikai Co, LTD) at 1,500 rpm for 1 hour followed by the addition of ethanol (400 μL). The reaction mixture was then shaken at 1,500 rpm for 11 hours. The ligand-exchanged GNRs were washed by 3 cycles of centrifugation, removal of the supernatant (about 480 μL) to remove the free thiol ligands, and the addition of ethanol up to 500 μL . The GNRs were then washed twice using 1 mM NaOH aq. Finally, the GNRs were dispersed in 1 mM

NaOH. The concentrations of the GNRs (33 x 14 nm, 33 x 8 nm, and 54 x 15 nm) were 0.3, 0.1, and 0.1 nM, respectively.

- **Preparation of C2-GNSs**

Citrate-protected GNPs in aqueous solution (15 or 30 nm in diameter) were purchased from BBI Solutions (UK). The original concentration of each GNP, the centrifugation conditions, the number of surface Au atoms, and the final concentration of thiolate ligands are summarized in Table 4-1. The GNPs were concentrated 50-fold by centrifugation. The concentrated citrate-protected GNPs (20 μ L) were added to a MeOH solution of the **C2-E6C11** ligand (80 μ L) (Final concentrations of the **C2-E6C11** ligand are shown in Table S1). In this exchange reaction, the total ligand concentration was adjusted to 10 equiv. After incubation for 12 hours at room temperature, the ligand-exchanged GNSs were washed by 3 cycles of centrifugation, the removal of the supernatant (about 480 μ L) to remove the free thiol ligands, and the addition of ethanol up to 500 μ L. Then, the GNSs were washed twice using 1 mM NaOH aq. Finally, the GNRs were dispersed in 1 mM NaOH. The prepared 15-nm and 30-nm GNSs with **C2-E6C11** ligand were referred to as **C2-15-GNSs** and **C2-30-GNSs**. The concentrations of the 15-nm and 30-nm GNSs were 0.8 and 0.1 nM, respectively.

Table 4-1. The original concentration, the number of surface Au atoms, and the final concentration of the **C2** ligands, and the centrifugation condition.

<i>Size</i>	<i>Original concentration</i>	<i>Number of surface Au atoms</i>	<i>Final concentration of the C2-E6C11 ligands</i>	<i>Centrifugation</i>
15 nm	2.3 nM	9585	2.0 mM	10,000 g for 20 min
30 nm	0.33 nM	38959	1.3 mM	8,000 g for 15 min

4-2-4. Characterization

- **UV-vis-NIR spectroscopy**

The UV-vis spectra of the GNRs were measured using a V-770 UV-Visible/NIR Spectrophotometer with PAC-743R Automatic 6 position Peltier cell changer (JASCO, Japan). The heating and cooling rate was 0.5°C/min for the temperature-change measurements of the GNR spectra.

- **Dynamic light scattering and zeta-potential**

The hydrodynamic diameter of the GNRs or their assemblies was measured using a Zeta-potential & Particle Size Analyzer ELSZ-2000S (Otsuka Electronics Co., Ltd., Japan). The emission wavelength for the measurement was 633 nm. Prior to measurement, the temperature was kept constant for 10 min. Cumulant analysis was applied to determine the hydrodynamic diameter. The zeta-potential of the GNRs was measured using a Delsa Nano HC system (Beckman Coulter, Inc., USA).

- **Scanning transmission electron microscopy observation**

Scanning transmission electron microscopic (STEM) images were obtained using a STEM HD-2000 system (Hitachi High-Tech Manufacturing & Service Co., Ltd., Japan) with 200 kV acceleration voltage. STEM samples were prepared by adding a drop of the GNR solution on to the collodion membrane attachment mesh (Nisshin EM, Japan) and dried in a desiccator overnight. For the observation of assembled structures, the solvent was evaporated at an appropriate temperature in a thermostatic oven.

- **Inductively Coupled Plasma Atomic Emission Spectroscopy (ICP-AES)**

After purification to remove the residual thiol ligands, the solvent was removed using a centrifugal evaporator. Aqua regia (2 mL) was added to the dried C2-GNRs(33x14) and then diluted with MilliQ water up to 10 mL, to provide a sample for the measurement of S atom concentration. However, the concentration of the Au atom constituting the C2-GNRs(33x14) exceeds the upper limit of detection in order to detect the S atom of the ligand. Therefore, 100 μ L of the sample for S atom detection was diluted with MilliQ water up to 10 mL to measure the concentration of Au atom. All ICP-AES measurements were repeated independently three times. The concentrations of Au and S atoms in the original solution as determined by ICP-AES were 40100 ± 800 ppb and 220 ± 25 ppb, respectively.

- **Calculation of the ligand density on the GNR(33x14) from the Au and S atoms concentration**

The concentrations of Au and S atoms (C_{Au} and C_S) were determined by ICP-AES. Then,

the concentration of GNRs (C_{GNR}) was calculated.

$$C_{NP} = C_A / (V_{GNR} / V_{Au}) \quad (1)$$

V_{Au} represents the volume of a gold atom ($= 0.017 \text{ nm}^3$). V_{GNR} is the volume of a GNR, which is calculated using eq (2).

$$V_{GNR} = \frac{4\pi r^3}{3} + \pi r^2(l - 2r) \quad (2)$$

The r and l are the diameter and length of the GNR(33x14), respectively. The molecular number per nanoparticle (N_m) is:

$$N_m = C_S / C_{NP} \quad (3)$$

Then, the ligand density (D) can be obtained by dividing the N_m by the surface area (SA_{GNR}):

$$D = N_m / SA_{GNR} \quad (4)$$

Here, SA_{GNR} is calculated using eq (5)

$$SA_{GNR} = 4\pi r^2 + 2\pi r(l - 2r) \quad (5).$$

The free volume of the ligand (V_F) was determined by dividing the volume of the shell of the ligand (V_S) by N_m . The thickness of the shell was assumed to be the length of the ligand molecule ($L_m = 3.9 \text{ nm}$).

$$V_F = V_S / N_m \quad (6)$$

4-3. Results and discussion

4-3-1. Preparation of the thermoresponsive GNRs coated with thiolate ligands

The size of the prepared GNRs coated with CTAB was 33 nm in length and 14 nm in diameter as determined by STEM observation (Figure 4-3a and 4-4a, b). Thus, they are referred to as CTAB-GNRs(33x14). The transverse and longitudinal localized surface plasmon resonance (T-LSPR and L-LSPR) peaks were 517 and 653 nm, respectively (Figure 4-3b). These plasmon peaks were reasonable in terms of aspect ratio.²⁸ The zeta-potential was 46 ± 3.3 mV. The GNRs(33x14) modified with the **C2-E6C11** ligand, referred to as **C2-GNRs(33x14)**, were prepared *via* a ligand exchange reaction and dispersed in 1 mM NaOH aqueous solution. The zeta-potential value was changed from strongly positive for original CTAB-GNRs(33x14) to slightly negative (-14 ± 1.3 mV). The surface ligand density of **C2-GNRs(33x14)** was determined by ICP-AES. From the ratio of the Au to S atoms obtained by ICP-AES, the ligand density of the **C2-GNRs(33x14)** was found to be 6.0 ligands/nm². This density is considered reasonable when compared to the previously reported values on a GNS (4-8 ligands/nm²).³⁰⁻³²

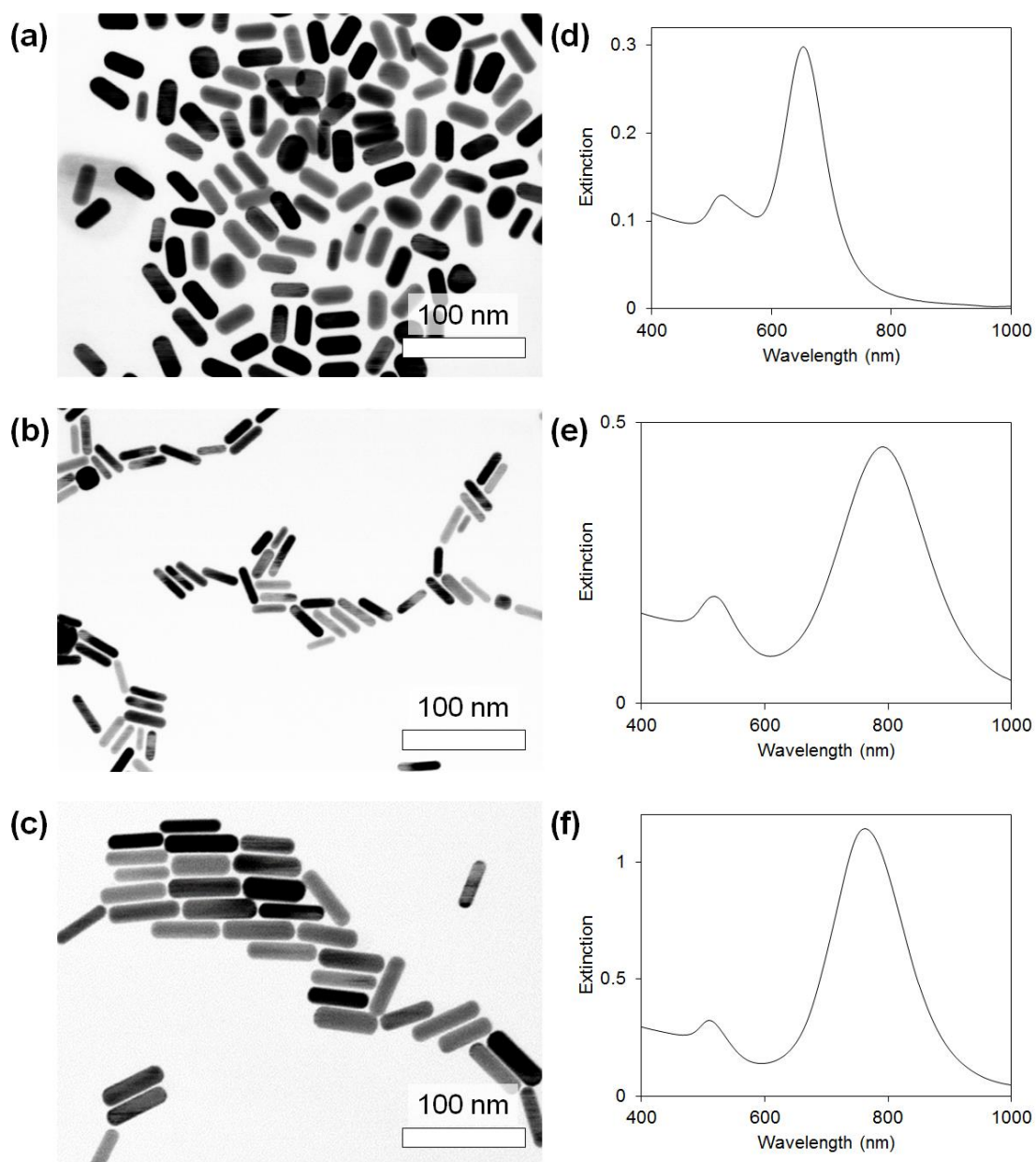


Figure 4-3. (a-c) STEM images of (a) CTAB-GNRs(33x14), (b) CTAB-GNRs(33x8), and (c) CTAB-GNRs(54x15). (d-f) Extinction spectra of (d) CTAB-GNRs(33x14), (e) CTAB-GNRs(33x8), and (f) CTAB-GNRs(54x15).

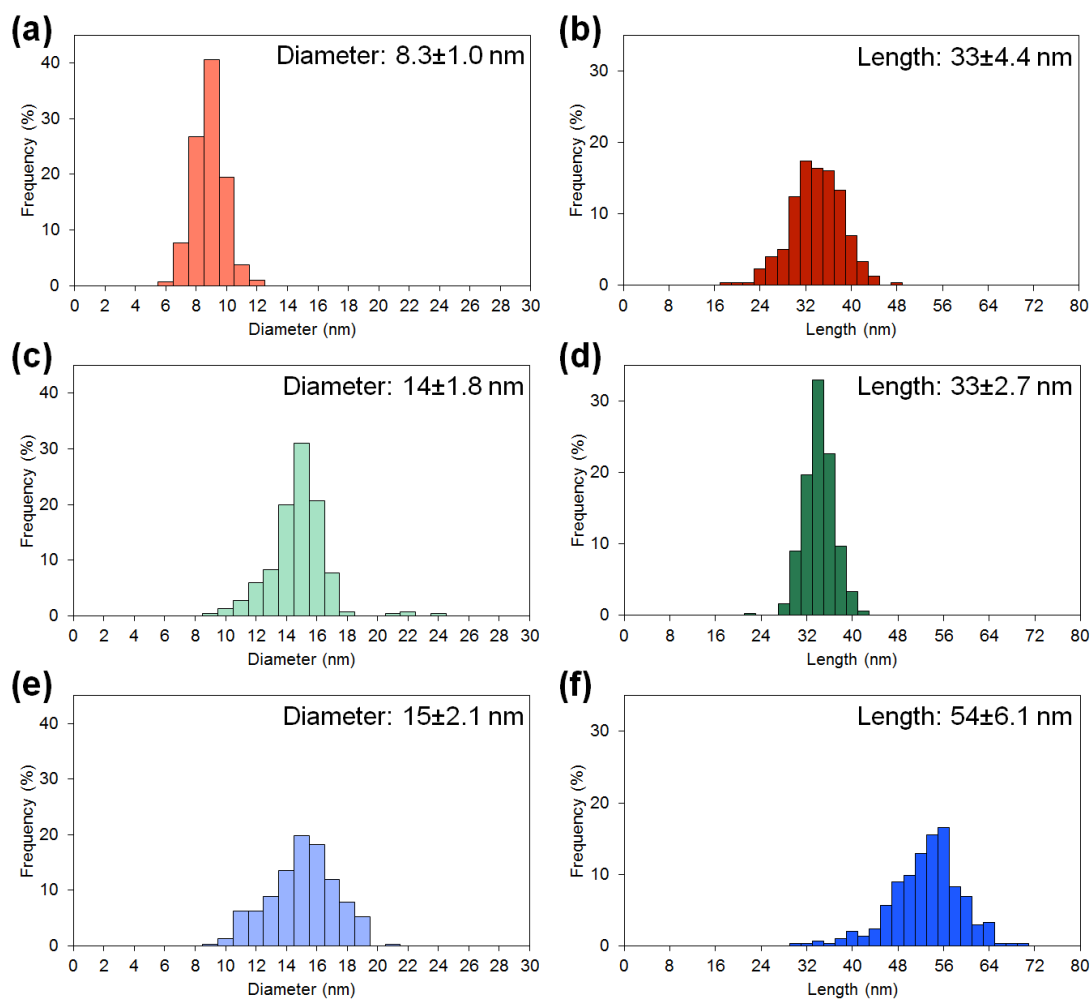


Figure 4-4. The histograms of the diameter and length of (a, b) GNRs(33x8), (c, d) GNRs(33x14), and (e, f) GNRs(54x15). The size was calculated as the average of over 300 particles based on STEM images.

4-3-2. Two-step assembly upon heating

First, I observed color changes in the **C2**-GNR dispersion upon heating. The dispersion appeared blue, magenta, and purple at 10, 30, and 60°C, respectively (Figure 4-5a). I note that the shape of GNRs(33x14) modified with thiolate ligands was unchanged on heating at 60°C for 1 hour, while heating at 60°C induced shape deformation of GNRs coated with CTAB. I synthesized GNRs(33x14) modified with thioalkylated hexa(ethylene glycol) with a hydroxy group (HS-(CH₂)_x-(OCH₂CH₂)₆-OH, x = 11, **OH-E6C11**) shown in Figure 4-1a. In Chapter 3, I have mentioned that the **OH-E6C11** ligands did not afford the thermoresponsive assembly of GNSs. Therefore, the **OH**-GNRs(33x14) do not show thermoresponsive assembly. To investigate the thermal stability of the shape, the CTAB- and **OH**-GNRs(33x14) were heated. The L-LSPR of CTAB-GNRs(33x14) was shifted to a shorter wavelength by heating at 60°C for 1 hour, indicating their deformation (Figure 4-6a).^{33,34} In contrast, the spectra of the **OH**-GNRs(33x14) barely changed (Figure 4-6b). Hence, the modification of the GNR surface with thiol ligands could improve the thermal stability of GNRs. However, heating to 80°C induced shape deformation of the **OH**-GNRs(33x14). Thiol ligands densely absorbed on the GNR surface were thought to suppress the motility/diffusion of surface Au atoms on the GNRs better than CTAB, probably because CTAB is bound to the surface through weaker electrostatic interactions between the cationic head group (quaternary ammonium) and anionic sites on the gold surface rather than by gold-sulfur bonds.^{33,34} Therefore, these color changes indicate the formation of GNR assemblies, but not the deformation of GNRs.

The extinction spectra of the **C2**-GNRs(33x14) were measured between 10 and 60°C at every 5°C (Figure 4-7a). Figure 4-5b shows the extinction spectra at 10, 30, and 60°C. From 10 to 25°C, the L-LSPR peaks stayed around 651 nm (Figure 4-5c), which is

in close agreement with the wavelength of the dispersed CTAB-GNRs(33x14), supporting the notion that the C2-GNRs(33x14) were dispersed below 25°C. DLS measurement also indicated the dispersed state of C2-GNRs(33x14) at below 25°C (Figure 4-7d). From 25 to 30°C, the L-LSPR was shifted to a shorter wavelength and merged with the T-LSPR. It has been reported that the blue shift in the L-LSPR and the concurrent red shift in T-LSPR occur on the formation of side-by-side assemblies.³⁵⁻³⁹ Therefore, the observed spectrum at 30°C indicates the formation of a side-by-side assembly. The extinction peaks plotted against temperature upon heating also clearly show that side-by-side assembly occurred between 25 and 30°C (Figure 4-5c). The hydrodynamic diameter of the assemblies measured by DLS was ~100 nm at 30°C, which is larger than that of the dispersed state at 25°C (Figure 4-7d). By further heating, from 35 to 60°C, the extinction peak shifted to a longer wavelength and the spectra became broader than that at 30°C. The plot of extinction peak vs. temperature shows that the peak gradually shifted up to 60°C (Figure 4-5c). As the hydrodynamic diameter measured by DLS was increased from 100 nm to 500 nm upon heating, the gradual shift of the extinction peak occurring within the range from 30 to 60°C was correlated with the increase in size (Figure 4-5c, d). This subsequent structural change in assembly suggests the occurrence of two-step assembly.

The C2-GNRs(33x14) dispersion was dried at 30 or 60°C on the TEM grid for STEM observation. Even after the drying process, side-by-side assemblies, which were aligned perpendicular to the grid, were observed as expected from the spectrum around 30°C (Figure 4-5e).³⁸ On the other hand, the assembly structures at 60°C looked like a random aggregation at first glance (Figure 4-5f). However, detailed observation revealed that the assembly at 60°C was composed of units of side-by-side assembly (enlarged view in Figure 4-5f). I refer to this a large assembly with a hierarchical structure as to an

“assembled-assembly” to distinguish it from a random aggregation. Importantly, side-by-side assemblies and assembled-assemblies were observed at different temperatures (30 and 60°C, respectively), suggesting the sequential, two-step assembly of GNRs in solution upon heating.

The extinction spectra measured every 1°C between 25 and 30°C were shown in Figure 4-7b. Side-by-side assembly leads the shift of L-LSPR to shorter wavelength and T-LSPR to longer wavelength. However, L-LSPR hardly shifted to shorter wavelength, but the shift of T-LSPR occurred. This suggests that dispersed GNRs and side-by-side-assembly are co-existed between 25 and 30°C, which implies that the dehydration occurred quickly. The observation of a peak derived from scattering due to rotational diffusion (1-1.5 nm) by DLS supports co-existence of dispersed and assembled states.

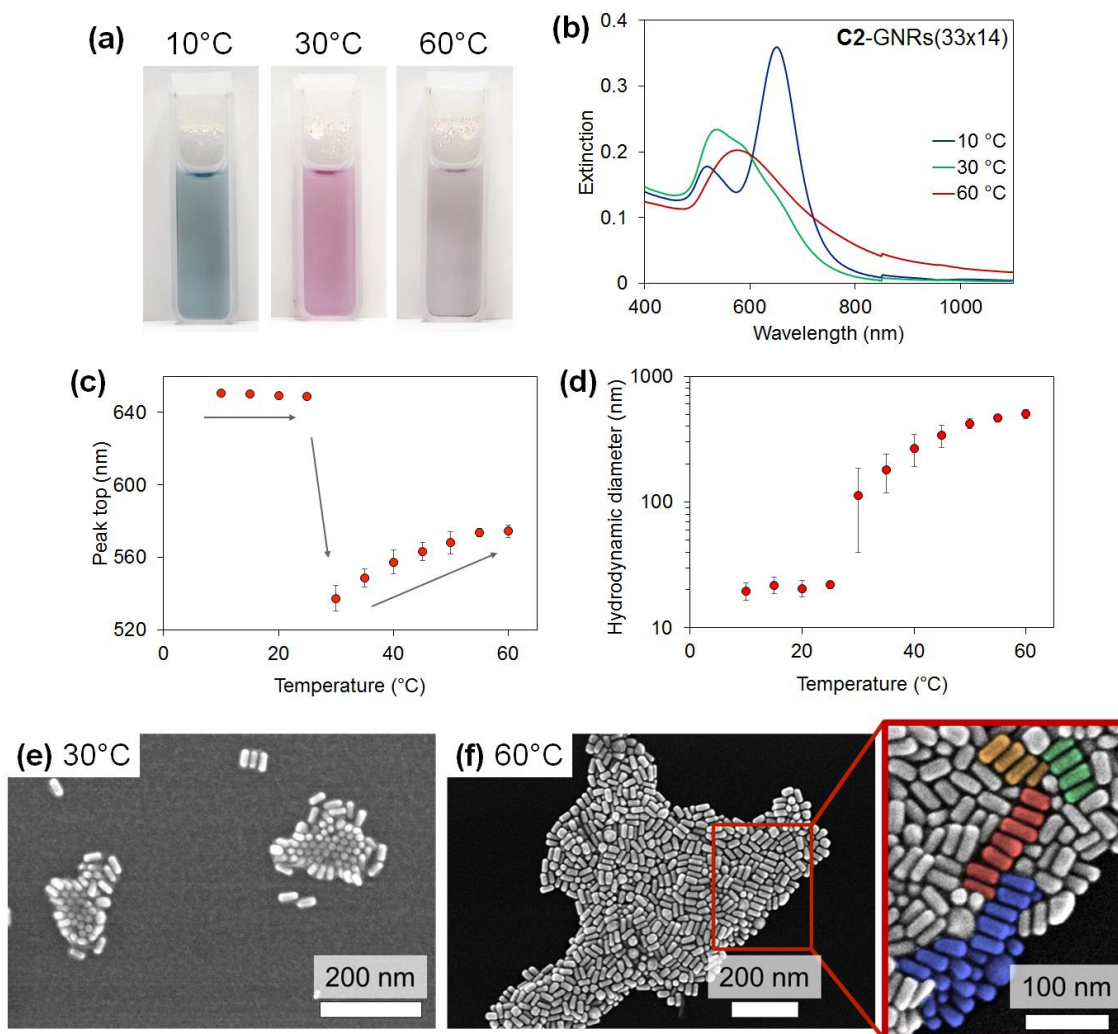


Figure 4-5. (a) Photographs of a C2-GNRs(33x14) dispersion in a glass cuvette (40 x 10 x 10 mm) at 10, 30, and 60°C. (b) Extinction spectra of the C2-GNRs(33x14) at 10, 30, and 60°C. (c, d) Temperature-dependent changes in (c) the extinction peak and (d) the hydrodynamic diameter as determined by cumulant analysis on DLS between 10 and 60°C. Error bars represent SD ($n = 3$). When there were multiple peaks, the peak top with the larger extinction was plotted. (e, f) STEM images of C2-GNRs(33x14) dried at (e) 30 and (f) 60°C. Note that some units of the side-by-side assembly were discolored in the enlarged image.

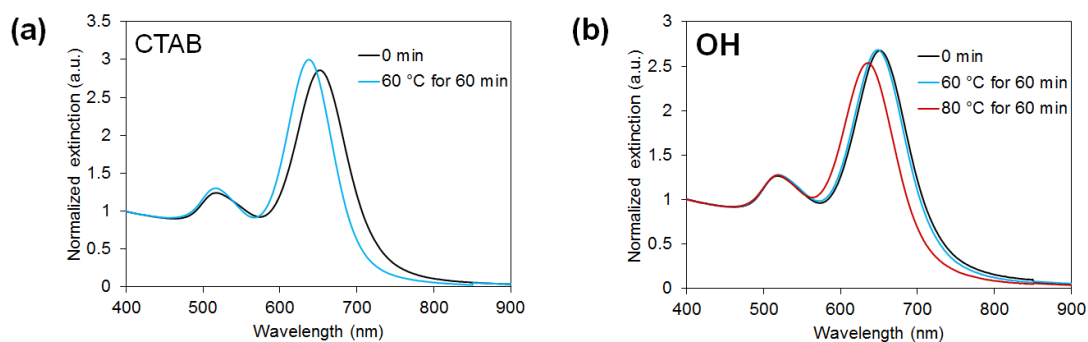


Figure 4-6. (a, b) Normalized extinction spectra of (a) CTAB-, (b) OH-GNRs(33x14) after heating for 1 hour. Black line shows the original spectra of each sample before heating. The dispersions of each GNR were incubated at 60°C (blue line) and 80°C (red line) for 1 hour. These spectra were normalized at 400 nm.

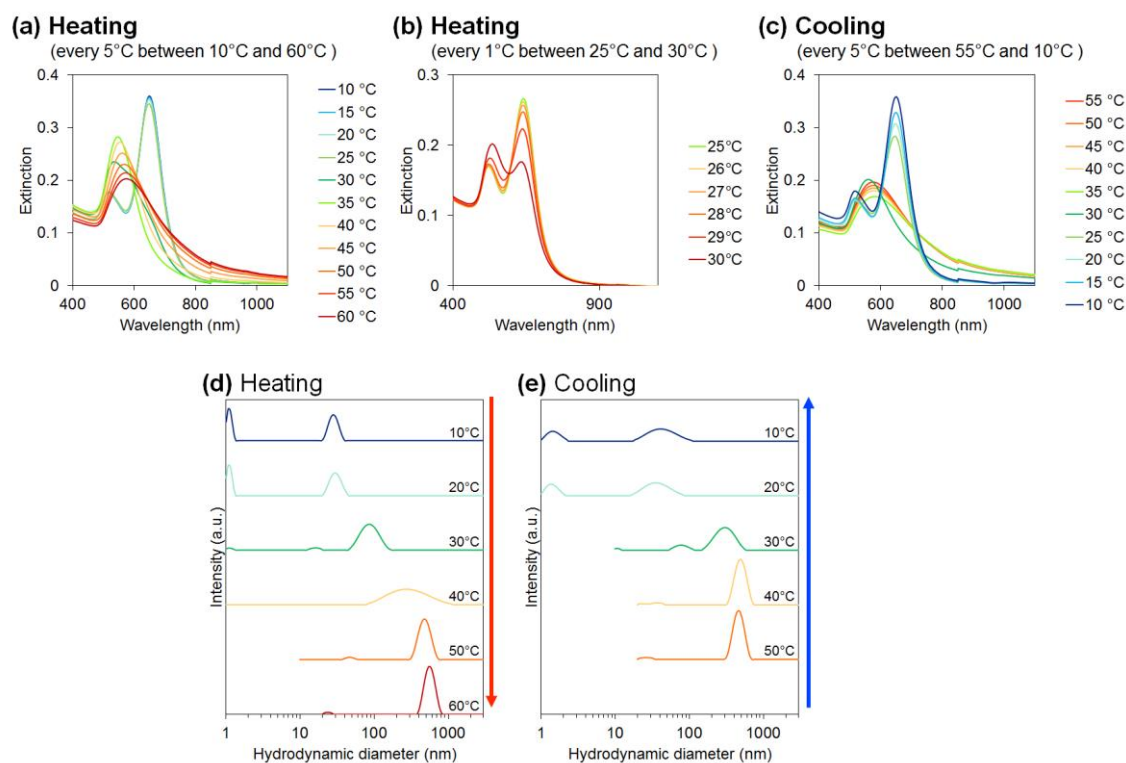


Figure 4-7. (a, b, c) Extinction spectra of the C2-GNRs(33x14) at different temperatures upon heating measured (a) every 5°C and (b) every 1°C, and (c) cooling. (d, e) Intensity distribution of the hydrodynamic diameter of C2-GNRs(33x14) at different temperatures (d) upon heating and (e) cooling.

4-3-3. Reversibility of the two-step assembly on thermal cycling

To confirm the reversibility of the two-step assembly, I investigated the cooling process. After the temperature reached at 60°C by heating, the solution was cooled. The broad spectra indicating the formation of an assembled-assembly structure were observed within the range from 55 to 35°C (Figure 4-7c). Surprisingly, the peak showed no shift to a shorter wavelength upon cooling (Figure 4-8a), and the hydrodynamic diameter also remained around 500 nm in this temperature range (Figure 4-8b). The clear hysteresis between the heating and cooling processes for **C2-GNRs(33x14)** was not observed for 5-nm GNS coated with **C2-E6C11** ligands (Chapter 2). Then, intriguingly, the extinction peak was shifted to a shorter wavelength at 30°C (Figure 4-8a and the green line in the extinction spectra shown in Figure 4-7c), indicating that side-by-side assemblies were regenerated by cooling. This suggests that the edge-ligands were hydrated again by cooling though while the side-ligands remained in a dehydrated state. On further cooling, two peaks appeared, corresponding to the peaks for the original dispersed **C2-GNRs(33x14)**. Although a part of dispersed GNRs was precipitated when large assemblies were formed, they were re-dispersed by gentle stirring. The spectrum at 10°C after cooling with gentle stirring was consistent with that before heating. Figure 4-8c show the gradient cooling process of the **C2-GNRs** dispersion in the glass cuvette on ice. The three different colors (purple, magenta, and blue) were observed in the cuvette. Additionally, this reversible thermoresponsive two-step assembly was repeatable over several times (Figure 4-8d).

I note that the extinction peak shifts during the cooling process show the two-step structural change more clearly than does the heating process; an initial shift to a shorter wavelength and a subsequent shift to longer wavelength. These two different peak

shifts correspond to the re-formation of the side-by-side assembly and the disassembly of the side-by-side assembly into dispersed C2-GNRs(33x14), respectively. Thus, I determined the temperature ranges of assembly temperatures, T_{A1} and T_{A2} , from the cooling process. The T_{A1} and T_{A2} of C2-GNRs(33x14) were 25-30°C and 30-35°C, respectively.

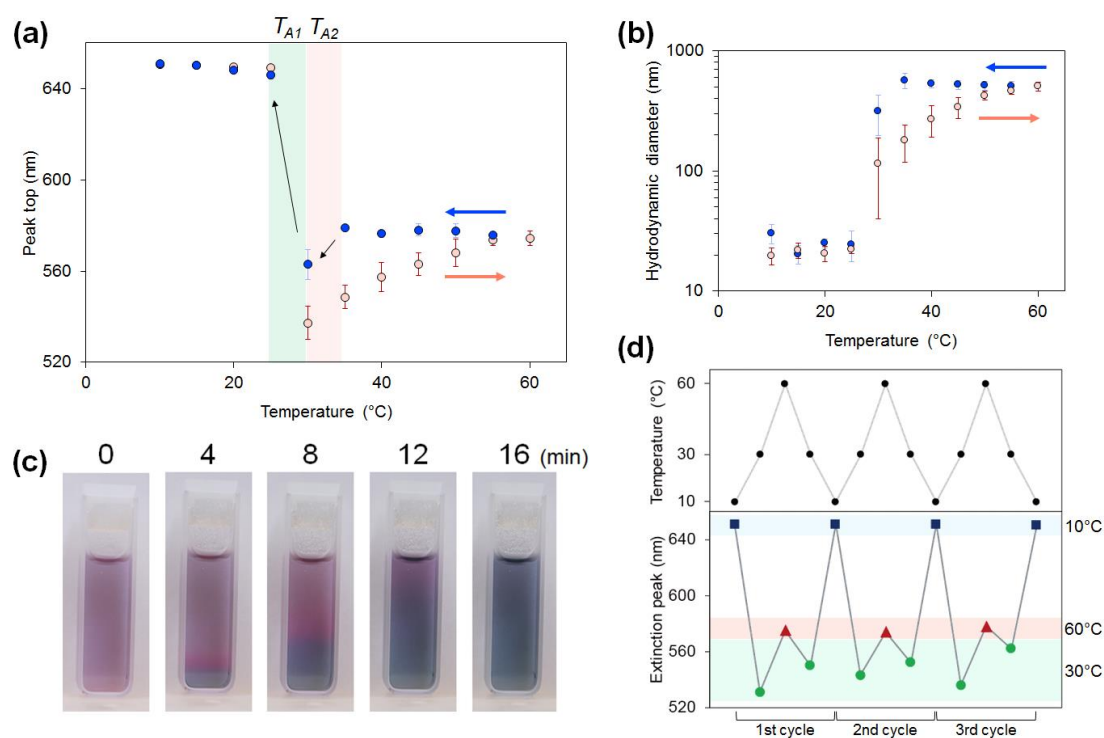


Figure 4-8. (a, b) Temperature-dependent changes in (a) the extinction peak and (b) the hydrodynamic diameter determined by cumulant analysis on DLS between 10 and 60°C (red dots: heating process; blue dots: cooling process). Error bars represent SD ($n = 3$). (c) Photographs of C2-GNRs(33x14) dispersion in a glass cuvette (40 x 10 x 10 mm) on ice. (d) Reversible changes in the extinction peak are observed at 10, 30 and 60°C.

4-3-4. Examination of assembly mechanism by time course experiments

As mentioned above, hysteresis observed between 35-60°C. This suggests that the size growth of the assembled-assembly includes a time-dependent factor; therefore, incubation time should be taken into consideration. To clarify the assembly mechanism, I investigated the effect of incubation time on the thermoresponsive assembly of C2-GNRs(33x14). The temperature of the solution was maintained at 30 or 40°C, and the time course of the extinction spectra and hydrodynamic diameter were monitored. The extinction spectra at 30°C, which indicate the formation of a side-by-side assembly, remained unchanged for three hours (Figure 4-9a). The time-course plots of the extinction peak at each temperature show that the peak at 30°C remained at around 555 nm (blue dots in Figure 4-9c). The hydrodynamic diameter at 30°C was also independent on time and was around 100 nm, which is in close agreement with the value measured upon heating (Figure 4-5d and blue circles in Figure 4-9d). The side-by-side assembly was observed as a steady state at a temperature between T_{A1} and T_{A2} , supporting the notion that the edge-ligands remained in a hydrated state. Meanwhile, the extinction spectra at 40°C; i.e., over the T_{A2} , became broader after incubation for 3 hours (Figure 4-9b), and the peak gradually shifted from 555 to 590 nm within 2 hours (red dots in Figure 4-9c). The hydrodynamic diameter at 40°C also increased from 250 to 550 nm (red circles in Figure 4-9d), indicating the time-dependent growth of the assembled-assembly. Moreover, the size of the assembled-assembly incubated at 40°C for 3 hours (550 nm) is consistent with the size when temperature reached at 60°C upon heating. The eventual size at 40 and 60°C was similar regardless of the temperature, indicating that the dehydration state at 40°C is same as that at 60°C.

The assembly mechanism revealed by the time course study is as follows (Figure 4-9e). When the solution temperature reached T_{A1} by heating, the side-by-side assembly was formed as a steady state (or an equilibrium state) by the dehydration of the side-ligands to reduce the surface area where the dehydration occurred. By further heating, when the temperature reached T_{A2} , the side-by-side assembled structures were reconfigured to an assembled-assembly through time-dependent growth as the edge-ligands were also dehydrated. On cooling, the assembled-assembly structures remained without any disassembly above T_{A2} as the dehydration state was unchanged. When the temperature reached T_{A2} , the re-formation of side-by-side assembly occurred, indicating that the edge-ligands were re-hydrated. Therefore, the results described above showed that two assembly temperatures exist and that the two-step assembly was induced by stepwise dehydration.

Generally, dehydration is known as a phenomenon that occurs cooperatively in a narrow temperature range. One-step dehydration occurs was also considered as another possibility (Figure 4-10). If all ligands on the GNR surface regardless of their location are dehydrated at T_{A1} , side-by-side assembly might be observed transiently. However, there is no reason for the structure to remain in a steady state. The subsequent structural change in assembly is expected to with the passage of time. In fact, the time course study showed the side-by-side assembly remained in a steady state at 30°C. Therefore, the existence of a stepwise dehydration process was supported by the results of the time course study.

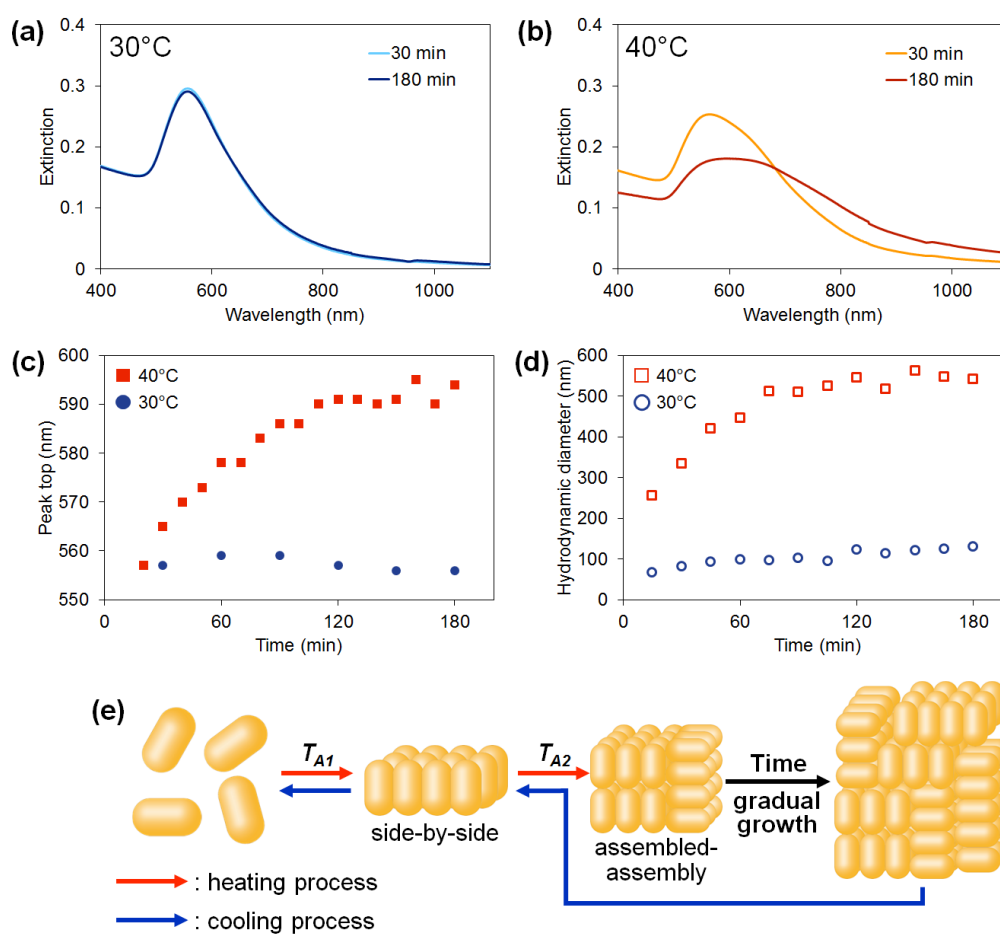


Figure 4-9. (a, b) Extinction spectra of a C2-GNRs(33x14) dispersion maintained at (a) 30 and (b) 40°C for 30 and 180 min. (c, d) Time-dependent changes in (c) the extinction peak and (d) the hydrodynamic diameter between 0 and 180 min (blue dots: 30°C; red square: 40°C). (e) Schematic illustration of the two-step thermoresponsive GNR assembly process.

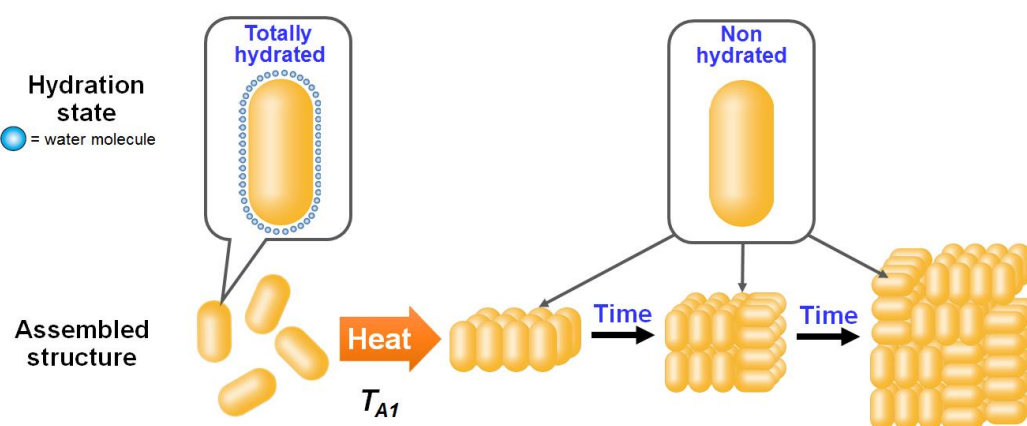


Figure 4-10. Another possible mechanism for the assembly process: one-step dehydration.

4-3-5. Factors determining assembly temperature

- **Effects of GNR length and diameter**

I showed the two-step thermoresponsive assembly caused by the dehydration of the edge- and side-ligands at different temperatures. Here, I describe the factors determining the two assembly temperatures. In Chapter 3, I have reported that the assembly temperature of GNSs was dependent on the nanoparticle curvature and the hydrophobicity of the alkyl head on the ligand. However, I could not eliminate the contribution of van der Waals interactions to the assembly temperature as the size of the GNSs increased with decreases in the curvature. In the case of GNRs, the curvature varies with diameter, but is independent of length. Therefore, the effect of van der Waals interaction could be clarified by a comparison of different shaped GNRs. To compare the assembly temperatures of the **C2**-GNRs, I synthesized GNRs of 33 nm x 8.3 nm and 54 nm x 15 nm in size covered with **C2-E6C11** ligands [referred to as **C2**-GNRs(33x8) and **C2**-GNRs(54x15), respectively] (Figure 4-3, 4-4 and 4-11). The **C2**-GNRs(33x8) have the same length but smaller diameter, and **C2**-GNRs(54x15) have a greater length with a similar diameter to the **C2**-GNRs(33x14).

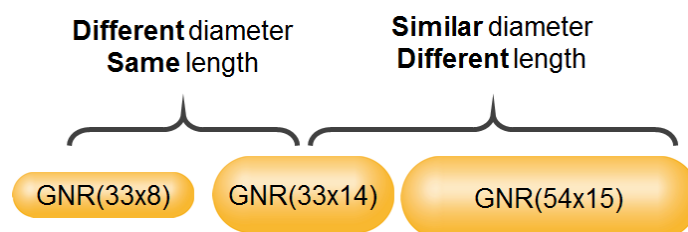


Figure 4-11. Schematic illustration of GNRs(33x8), GNRs(33x14), and GNRs(54x15).

Similar assembly behavior was observed for the C2-GNRs(33x8) and C2-GNRs(54x15) (Figure 4-12 and 4-13). The temperature range of T_{A1} and T_{A2} for C2-GNRs(33x8) were determined from the cooling process. Shifts to a shorter wavelength of the peak, indicating the formation of the side-by-side assembly, occurred from 50 to 40°C (Figure 4-14a, b). The re-dispersion by cooling took place from 40 to 35°C. Hence, the T_{A1} and T_{A2} of the C2-GNRs(33x8) were around 35-40°C and 40-50°C, respectively, which were higher than those of the C2-GNRs(33x14) (Table 4-2). Therefore, this result shows that larger free volume induced higher assembly temperatures for the GNRs as with the GNSs. On the other hand, the T_{A1} and T_{A2} of C2-GNRs(54x15) determined from the cooling process were around 25-30°C and 30-35°C, which were similar with those of the C2-GNRs(33x14) (Figure 4-14c, d). The T_{A1} and T_{A2} values for C2-GNRs of various sizes are summarized in Table 4-2. These results clearly showed that the assembly temperatures were independent of length while van der Waals interactions varied depending on length. Therefore, the curvature of the GNRs, but not van der Waals interaction between GNRs themselves, is a dominant factor in determining the assembly temperatures.

Table 4-2. Effects of GNR size effects on T_{A1} and T_{A2} of the C2-GNRs

<i>Sample</i>	<i>Length (nm)</i>	<i>Dimeter (nm)</i>	T_{A1} (°C)	T_{A2} (°C)
C2-GNRs(33x8)	33	8	35-40	40-50
C2-GNRs(33x14)	33	14	25-30	30-35
C2-GNRs(54x15)	54	15	25-30	30-35

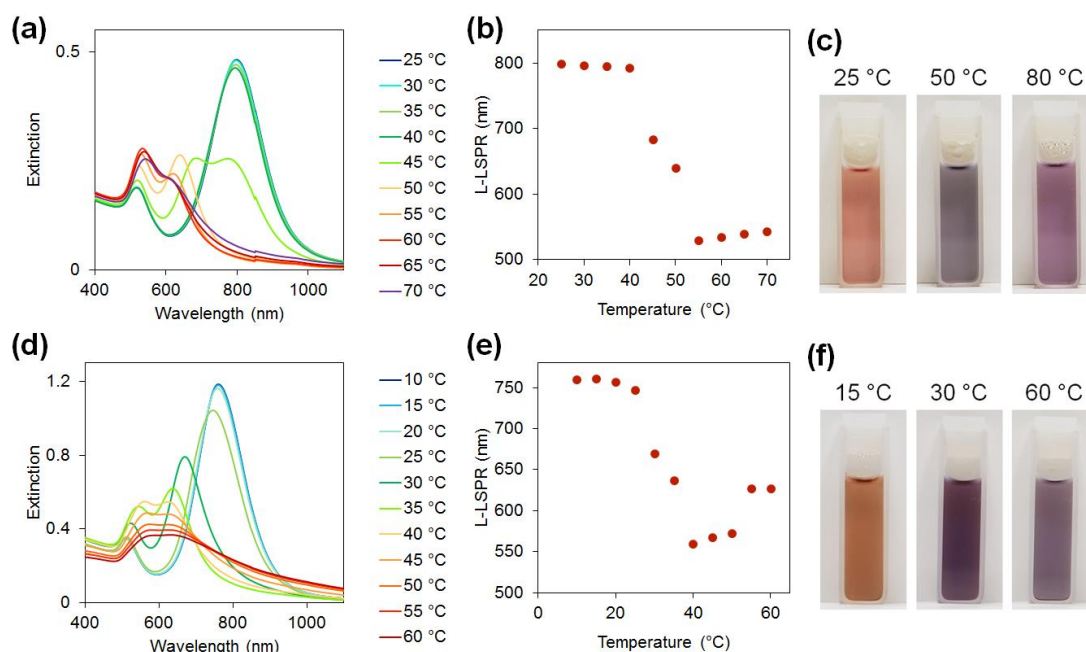


Figure 4-12. (a-c) C2-GNRs(33x8) and (d-f) C2-GNRs(54x15). (a, d) Extinction spectra at different temperatures upon heating. (b, e) The plot of temperature-dependent changes in extinction peak upon heating. (c, f) Photographs of (c) C2-GNRs(33x8) and (f) C2-GNRs(54x15) in a glass cuvette (40 x 10 x 10 mm) at different temperatures.

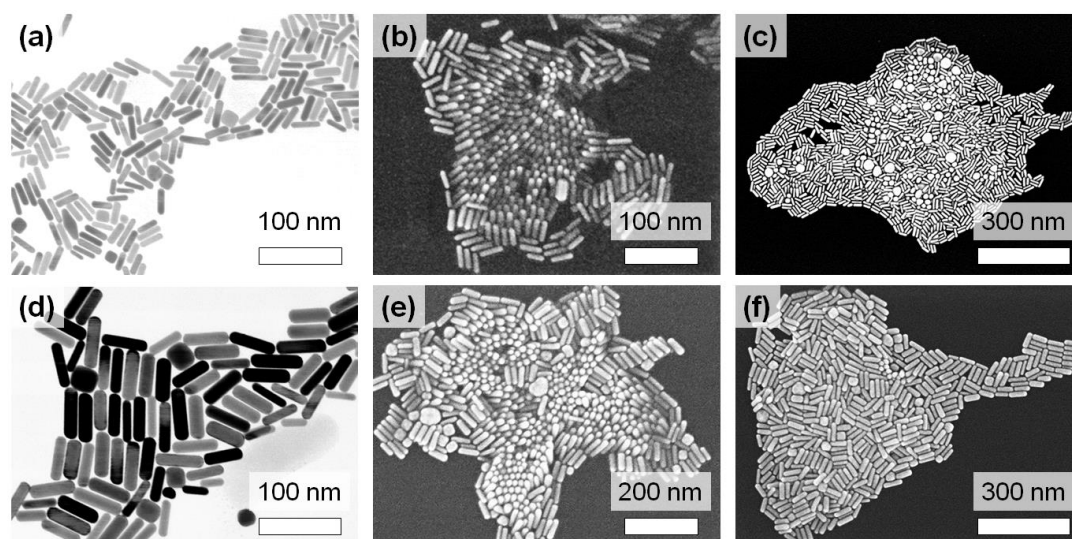


Figure 4-13. STEM images of (a-c) C2-GNRs(33x8) and (d-f) C2-GNRs(54x15) at different temperatures. The samples were dried for stem observation at (a) 25 °C, (b) 45 °C, (c) 70 °C, (d) 10 °C, (e) 30 °C, and (f) 60 °C

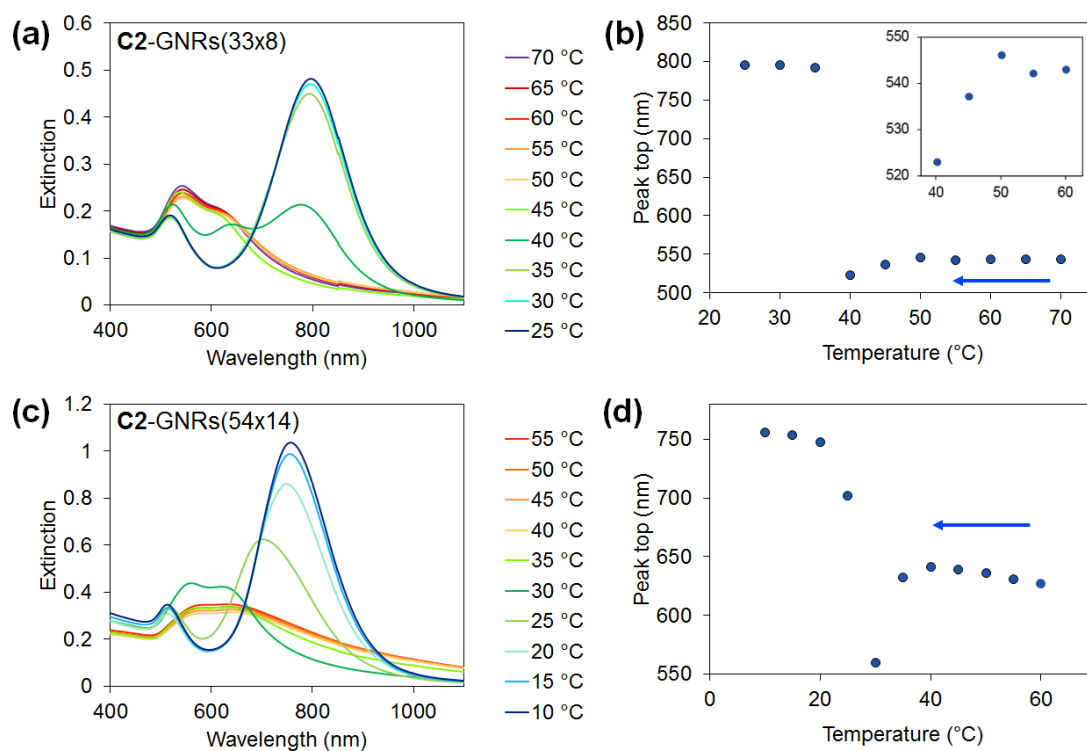


Figure 4-14. (a, b) Extinction spectra and temperature-dependent changes in extinction peak upon cooling of C2-GNRs(33x8). (c, d) Extinction spectra and temperature-dependent changes in extinction peak upon cooling of C2-GNRs(54x15) at different temperatures.

- **Comparison of the C2-GNRs and C2-GNSs**

Here, the T_{A1} and T_{A2} of GNRs were compared with that of GNSs. The T_A for GNSs was also dependent on the curvature corresponding to the free volume of the bound ligand. Assuming that the ligand density is independent of its location on the GNRs, the free volumes of the side- and edge-ligands were calculated. The free volume per single ligand for the side- and edge-ligands were calculated as 0.83 nm^3 and 1.1 nm^3 , which are similar to those for the ligands grafted on 30-nm and 15-nm GNSs (Table 4-3). The T_A for 30-nm and 15-nm GNSs coated with the **C2-E6C11** ligand (referred to as **C2-30-** and **C2-15-GNSs**) were 32 and 48°C, respectively (Figure 4-15). The observed T_{A1} from the results for **C2-GNRs** (25-30°C) was similar to the T_A of the **C2-30-GNSs**. In contrast, the T_{A2} determined from the measurements (30-35°C) was considerably lower than the T_A for **C2-15-GNSs** (48°C). This can be attributed to the cooperativity of dehydration. Side-ligand dehydration is thought to induce subsequent dehydration from the adjacent edge-ligands at a lower temperature. Additionally, as this calculation was based on the assumption that the shape of the edge portion was hemi-spherical and the crystal lattice on the GNR would not affect the ligand density, some minor doubts remain regarding these points. However, the results obtained using GNR and GNS of various sizes (in particular, the similarity between the T_{A1} for GNRs and the T_A for the corresponding GNS) strongly support the notion that the free volume of the ligand is the dominant factor in determining the assembly temperatures.

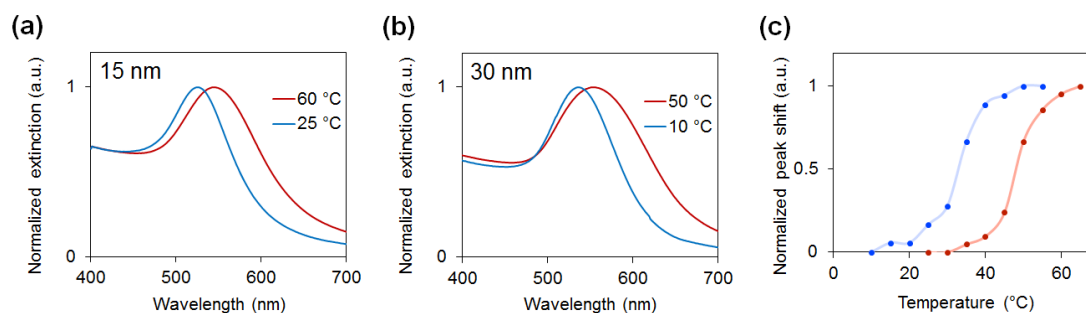


Figure 4-15. (a, b) Normalized optical extinction spectra of (a) C2-15-GNSs and (b) C2-30-GNSs at the temperatures shown in the plots. (c) The plot of temperature-dependent changes in extinction peak between (red dots: C2-15-GNSs; blue dots: C2-30-GNSs).

Table 4-3. The free volume of C2-15-GNSs, C2-30-GNS, edge-ligand, and side ligand on C2-GNRs(33x14). The free volumes were calculated assuming that the ligand density was 6.0 ligands/nm².

<i>Samples</i>	<i>Free volume (nm³)</i>
C2-15-GNSs	1.0
C2-30-GNSs	0.83
C2-GNRs(33x14) Edge-ligand	1.1
C2-GNRs(33x14) Side-ligand	0.83

- **Effect of the alkyl head**

Finally, I also confirmed the effect of the hydrophobicity of the alkyl head on assembly temperatures. The **C1-E6C11** ligand, which has a less hydrophobic alkyl head, was used (Figure 4-1a). The assembly temperatures for GNRs(33x14) coated with **C1-E6C11** ligand was 60-65°C (T_{A1}) and 65-70°C (T_{A2}) (Figure 4-16). Both were higher than the respective values for **C2-GNRs(33x14)**. This trend was similar to the results for GNSs in Chapter 2. Thus, the hydrophobicity of the head is also a dominant factor, indicating the assembly temperatures are tunable by adjusting the GNR diameter and the alkyl head.

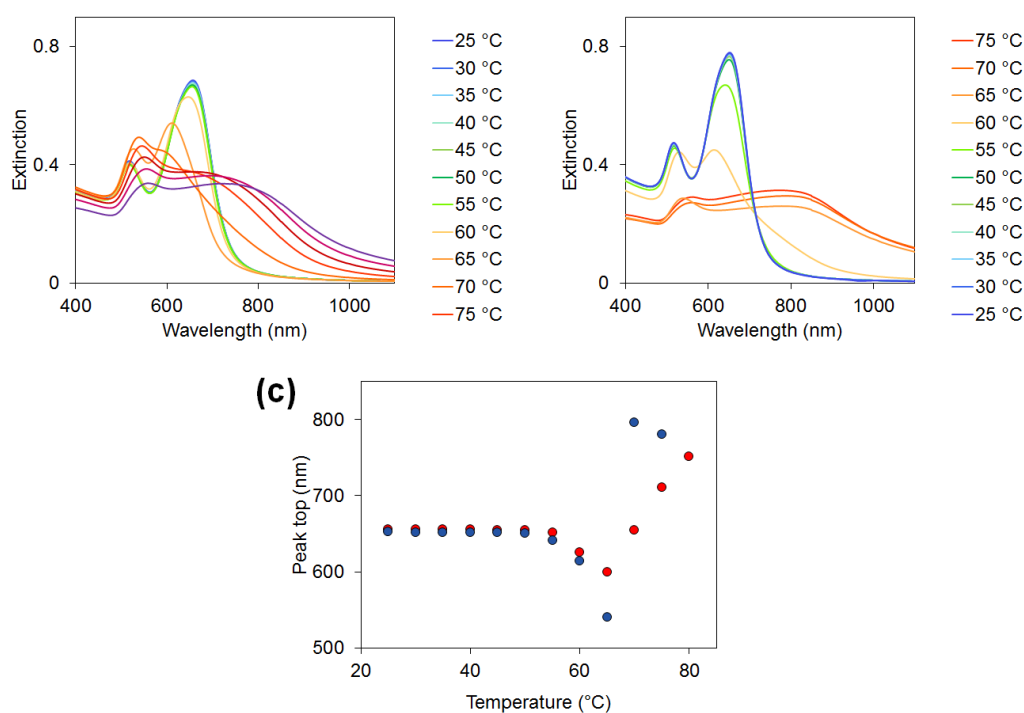


Figure 4-16. (a, b) Extinction spectra of **C1-GNRs(33x14)** at different temperatures upon (a) heating and (b) cooling. (c) The plot of temperature-dependent changes in extinction peak between 25 and 80°C (red dots: heating process; blue dots: cooling process).

4-4. Conclusion

I showed the thermoresponsive two-step assembly of GNRs modified with alkyl-headed hexa(ethylene glycol) derivatives. When the GNRs were assembled on heating, they first formed side-by-side assemblies. Subsequently, assembled-assemblies were formed in a temperature dependent manner *via* a two-step assembly process. On cooling, the assembled-assemblies were disassembled into side-by-side assemblies, and then re-dispersed. This two-step assembly was reversible and repeatable. The time course study supported the notion that this two-step assembly was induced by stepwise dehydration. The assembly temperature was dependent on the diameter of the GNR, but was independent of length, as the curvature of GNRs does not change when the length is varied. This result indicates that the assembly temperatures are primarily depended on the curvature. Additionally, the assembly temperatures were also dependent on the hydrophobicity of the alkyl head of the ligand.

Previous reports on stimulus responsive nanoparticles were mainly focused on the control of assembly and disassembly state. Here, I achieved the fabrication of a hierarchical structure *via* the reversible two-step assembly of GNRs coated with a single kind of ligand. My approach focusing on differences in curvature allows it to be applied to other anisotropic nanoparticles, such as nanocubes and nanoplates, which could provide new guidelines for the construction of hierarchical structures.

4-5. References

- (1) Grzybowski, B. A.; Wilmer, C. E.; Kim, J.; Browne, K. P.; Bishop, K. J. M. Self-Assembly: From Crystals to Cells. *Soft Matter* **2009**, *5*, 1110.
- (2) Whitesides, G. M.; Grzybowski, B. Self-Assembly at All Scales. *Science* **2002**, *295*, 2418–2421.
- (3) Qiu, H.; Hudson, Z. M.; Winnik, M. A.; Manners, I. Multidimensional Hierarchical Self-Assembly of Amphiphilic Cylindrical Block Copolymers. *Science* **2015**, *347*, 1329–1332.
- (4) Yeom, B.; Sain, T.; Lacevic, N.; Bukharina, D.; Cha, S.-H.; Waas, A. M.; Arruda, E. M.; Kotov, N. A. Abiotic Tooth Enamel. *Nature* **2017**, *543*, 95–98.
- (5) Tsang, B.; Yu, C.; Granick, S. Polymers Zippered-up by Electric Charge Reveal Themselves. *ACS Nano* **2014**, *8*, 11030–11034.
- (6) Studart, A. R. Towards High-Performance Bioinspired Composites. *Adv. Mater.* **2012**, *24*, 5024–5044.
- (7) Zhou, Y.; Marson, R. L.; Van Anders, G.; Zhu, J.; Ma, G.; Ercius, P.; Sun, K.; Yeom, B.; Glotzer, S. C.; Kotov, N. A. Biomimetic Hierarchical Assembly of Helical Supraparticles from Chiral Nanoparticles. *ACS Nano* **2016**, *10*, 3248–3256.
- (8) Miszta, K.; de Graaf, J.; Bertoni, G.; Dorfs, D.; Brescia, R.; Marras, S.; Ceseracciu, L.; Cingolani, R.; van Roij, R.; Dijkstra, M.; Manna, L. Hierarchical Self-Assembly of Suspended Branched Colloidal Nanocrystals into Superlattice Structures. *Nat. Mater.* **2011**, *10*, 872–876.
- (9) Liu, Y.; He, J.; Yang, K.; Yi, C.; Liu, Y.; Nie, L.; Khashab, N. M.; Chen, X.; Nie, Z. Folding Up of Gold Nanoparticle Strings into Plasmonic Vesicles for Enhanced Photoacoustic Imaging. *Angew. Chem. Int. Ed.* **2015**, *54*, 15809–15812.
- (10) Qian, Z.; Ginger, D. S. Reversibly Reconfigurable Colloidal Plasmonic Nanomaterials. *J. Am. Chem. Soc.* **2017**, *139*, 5266–5276.
- (11) Zhu, M. Q.; Wang, L. Q.; Exarhos, G. J.; Li, A. D. Q. Thermosensitive Gold Nanoparticles. *J. Am. Chem. Soc.* **2004**, *126*, 2656–2657.

- (12) Liu, F.; Agarwal, S. Thermoresponsive Gold Nanoparticles with Positive UCST-Type Thermoresponsivity. *Macromol. Chem. Phys.* **2015**, *216*, 460–465.
- (13) Lin, Y.; Xia, X.; Wang, M.; Wang, Q.; An, B.; Tao, H.; Xu, Q.; Omenetto, F.; Kaplan, D. L. Genetically Programmable Thermoresponsive Plasmonic Gold/silk-Elastin Protein Core/shell Nanoparticles. *Langmuir* **2014**, *30*, 4406–4414.
- (14) Jones, S. T.; Walsh-Korb, Z.; Barrow, S. J.; Henderson, S. L.; Del Barrio, J.; Scherman, O. A. The Importance of Excess Poly(N-Isopropylacrylamide) for the Aggregation of Poly(N-Isopropylacrylamide)-Coated Gold Nanoparticles. *ACS Nano* **2016**, *10*, 3158–3165.
- (15) Liu, Y.; Han, X.; He, L.; Yin, Y. Thermoresponsive Assembly of Charged Gold Nanoparticles and Their Reversible Tuning of Plasmon Coupling. *Angew. Chem. Int. Ed.* **2012**, *51*, 6373–6377.
- (16) Kurzhals, S.; Zirbs, R.; Reimhult, E. Synthesis and Magneto-Thermal Actuation of Iron Oxide Core–PNIPAM Shell Nanoparticles. *ACS Appl. Mater. Interfaces* **2015**, *7*, 19342–19352.
- (17) Torii, Y.; Sugimura, N.; Mitomo, H.; Niikura, K.; Ijiro, K. pH-Responsive Coassembly of Oligo(ethylene Glycol)-Coated Gold Nanoparticles with External Anionic Polymers via Hydrogen Bonding. *Langmuir* **2017**, *33*, 5537–5544.
- (18) Orendorff, C. J.; Hankins, P. L.; Murphy, C. J. pH-Triggered Assembly of Gold Nanorods. *Langmuir* **2005**, *21*, 2022–2026.
- (19) Tian, Z.; Yang, C.; Wang, W.; Yuan, Z. Shieldable Tumor Targeting Based on pH Responsive Self-Assembly / Disassembly of Gold Nanoparticles. *ACS Appl. Mater. Interfaces* **2014**, *6*, 17865–17876.
- (20) Klajn, R.; Bishop, K. J. M.; Grzybowski, B. A. Light-Controlled Self-Assembly of Reversible and Irreversible Nanoparticle Suprastructures. *Proc. Natl. Acad. Sci. U. S. A.* **2007**, *104*, 10305–10309.
- (21) Kundu, P. K.; Samanta, D.; Leizrowice, R.; Margulis, B.; Zhao, H.; Börner, M.; Udayabhaskararao, T.; Manna, D.; Klajn, R. Light-Controlled Self-Assembly of Non-Photoresponsive Nanoparticles. *Nat. Chem.* **2015**, *7*, 646–652.
- (22) Glotzer, S. C.; Solomon, M. J. Anisotropy of Building Blocks and Their

- Assembly into Complex Structures. *Nat. Mater.* **2007**, *6*, 557–562.
- (23) Caswell, K. K.; Wilson, J. N.; Bunz, U. H. F.; Murphy, C. J. Preferential End-to-End Assembly of Gold Nanorods by Biotin-Streptavidin Connectors. *J. Am. Chem. Soc.* **2003**, *125*, 13914–13915.
- (24) Mochizuki, C.; Shinmori, H. Light-Triggered Assembly of Gold Nanorods Based on Photoisomerization of Spiropyrans. *Chem. Lett.* **2017**, *46*, 469–472.
- (25) Indrasekara, A. S. D. S.; Wadams, R. C.; Fabris, L. Ligand Exchange on Gold Nanorods: Going back to the Future. *Part. Part. Syst. Charact.* **2014**, *31*, 819–838.
- (26) Nie, Z.; Fava, D.; Kumacheva, E.; Zou, S.; Walker, G. C.; Rubinstein, M. Self-Assembly of Metal-Polymer Analogues of Amphiphilic Triblock Copolymers. *Nat. Mater.* **2007**, *6*, 609–614.
- (27) Nie, Z.; Fava, D.; Rubinstein, M.; Kumacheva, E. “Supramolecular” Assembly of Gold Nanorods End-Terminated with Polymer “Pom-Poms”: Effect of Pom-Pom Structure on the Association Modes. *J. Am. Chem. Soc.* **2008**, *130*, 3683–3689.
- (28) Ye, X.; Jin, L.; Caglayan, H.; Chen, J.; Xing, G.; Zheng, C.; Doan-Nguyen, V.; Kang, Y.; Engheta, N.; Kagan, C. R.; Murray, C. B. Improved Size-Tunable Synthesis of Monodisperse Gold Nanorods through the Use of Aromatic Additives. *ACS Nano* **2012**, *6*, 2804–2817.
- (29) Sau, T. K.; Murphy, C. J.; Commun, M. L. H. C.; Commun, A. C. Seeded High Yield Synthesis of Short Au Nanorods in Aqueous Solution. *Langmuir* **2004**, *11*, 6414–6420.
- (30) Hinterwirth, H.; Kappel, S.; Waitz, T.; Prohaska, T.; Lindner, W.; Lämmerhofer, M. Quantifying Thiol Ligand Density of Self-Assembled Monolayers on Gold Nanoparticles by Inductively Coupled Plasma-Mass Spectrometry. *ACS Nano* **2013**, *7*, 1129–1136.
- (31) Elzey, S.; Tsai, D. H.; Rabb, S. A.; Yu, L. L.; Winchester, M. R.; Hackley, V. A. Quantification of Ligand Packing Density on Gold Nanoparticles Using ICP-OES. *Anal. Bioanal. Chem.* **2012**, *403*, 145–149.
- (32) Torelli, M. D.; Putans, R. A.; Tan, Y.; Lohse, S. E.; Murphy, C. J.; Hamers, R. J. Quantitative Determination of Ligand Densities on Nanomaterials by X-Ray

- Photoelectron Spectroscopy. *ACS Appl. Mater. Interfaces* **2015**, *7*, 1720–1725.
- (33) Huang, J.; Mao, P.; Ma, P.; Pu, Y.; Chen, C.; Xia, Z. The Thermal Stability Mechanism of Gold Nanorods in Aqueous Solution. *Optik* **2016**, *127*, 10343–10347.
- (34) Zou, R.; Zhang, Q.; Zhao, Q.; Peng, F.; Wang, H.; Yu, H.; Yang, J. Thermal Stability of Gold Nanorods in an Aqueous Solution. *Colloid. Surface. A* **2010**, *372*, 177–181.
- (35) Park, H. S.; Agarwal, A.; Kotov, N. A.; Lavrentovich, O. D. Controllable Side-by-Side and End-to-End Assembly of Au Nanorods by Lyotropic Chromonic Materials. *Langmuir* **2008**, *24*, 13833–13837.
- (36) Fava, D.; Nie, Z.; Winnik, M. A.; Kumacheva, E. Evolution of Self-Assembled Structures of Polymer-Terminated Gold Nanorods in Selective Solvents. *Adv. Mater.* **2008**, *20*, 4318–4322.
- (37) Sreeprasad, T. S.; Pradeep, T. Reversible Assembly and Disassembly of Gold Nanorods Induced by EDTA and Its Application in SERS Tuning. *Langmuir* **2011**, *27*, 3381–3390.
- (38) Petukhova, A.; Greener, J.; Liu, K.; Nykypanchuk, D.; Nicolay, R.; Matyjaszewski, K.; Kumacheva, E. Standing Arrays of Gold Nanorods End-Tethered with Polymer Ligands. *Small* **2012**, *8*, 731–737.
- (39) Xie, Y.; Guo, S.; Ji, Y.; Guo, C.; Liu, X.; Chen, Z.; Wu, X.; Liu, Q. Self-Assembly of Gold Nanorods into Symmetric Superlattices Directed by OH-Terminated Hexa(ethylene Glycol) Alkanethiol. *Langmuir* **2011**, *27*, 11394–11400.

Chapter 5

Conclusion

In this thesis, I focused on the surface chemistry of nanoparticles and investigated their self-assembly. In this chapter, I summarize the thesis and afforded the significance and prospects.

In chapter 2, I fabricated Janus-like GNPs with hydrophobic/hydrophilic faces using phase separation of two surface ligands induced by hydrophobic interaction, and investigated their self-assembly behavior. Janus-like GNSs were successfully synthesized by a two-step addition of two ligands with alkyl chains of different lengths. The assemblies of Janus-like GNSs with hydrophilic/hydrophobic faces were more stably dispersed in water than were Domain GNSs, which are easily precipitated. This result showed that the degree of phase segregation of the two kinds of ligand molecule on the nanoparticle surface is important for controlling the assembled structure.

In chapter 3, I presented the thermoresponsive assembly of GNSs coated with a self-assembled monolayer of hexa(ethylene glycol) (HEG) ligands terminated with alkyl heads. I found that the assembly temperature can be easily tuned by changing the structure of the hydrophobic alkyl head. I also found that the assembly temperature decreased as the GNS diameter increased; that is, the free volume of a single ligand on the surface, which depended on the curvature, affected the temperature at which dehydration occurred. The assembly temperature at which the dehydration of HEG derivatives at the nanoparticle surface occurred depends not only on the chemical composition of the molecule but also on the free volume. This finding provides an important guideline for designing the surface for dynamic self-assembly.

In chapter 4, I showed that GNRs simply modified with a single kind of surface ligands performed a thermoresponsive two-step assembly driven by dehydration, providing hierarchical structures. On heating, they first formed side-by-side assembly

and then formed “assembled-assembly”, which was composed of the units of the side-by-side assembly. Importantly, the temperature at which dehydration of the ligand occurred was curvature-dependent; the dehydration occurred from the side-part first, and then from the edge-part subsequently upon heating. Because hierarchical structures as a higher order structure, which is generally constructed by sequential self-organization, could lead to higher functions in nature, controlled self-assemblies of metal nanoparticles have been attracting a great deal of attention. Up to now, complex surface modifications or shape controls of metal nanoparticles have been applied for the formation of those assemblies. In the approach focusing on differences in curvature on the anisotropic nanoparticles, the simple surface modification enables anisotropic nanoparticles to perform multi-step assembly for constructing hierarchical structures.

In this thesis, I showed the the rational surface design of for nanoparticle assembly. The concepts for the nanoparticle assemblies were inspired from protein folding. Living organisms dynamically control the transport and storage of energy, adjustment of catalytic activity, and signal transduction. They are mainly constructed with organic molecules. By using inorganic materials, including metal nanoparticles, in addition to organic molecules, it is possible to construct a system that exceeds biomaterials. Here, I reported the control of assembled structures and dynamic assembly system. The surface chemistry has made a large contribution to self-assembly, and still remains their importance. In future, the more sophisticated self-assembly into elaborate assembled stuctures, including hierarchical structures, will be achieved by excellent surface design. I believe that these studies have great contributions to the development of self-assembly.

Acknowledgement

These studies presented in this thesis have been performed under the guide of Prof. Kuniharu Ijiro. I would like to express my sincerest gratitude for his invaluable guidance and continuous encouragement throughout these studies.

I am deeply grateful to Prof. Kazuki Sada (Faculty of Science, Hokkaido University), Prof. Kei Murakoshi (Faculty of Science, Hokkaido University), Prof. Masako Kato (Faculty of Science, Hokkaido University), and Prof. Toshifumi Satoh (Faculty of Science, Hokkaido University) for valuable guidance and suggestion to summarize this thesis.

I gratefully appreciate to Prof. Kenichi Niikura (Nippon Institute of Technology), Associate Prof. Yasutaka Matsuo, Associate Prof. Hideyuki Mitomo (Research Institute for Electronic Science, Hokkaido University) for their kind and valuable guidance.

I wish to thank Dr. Shota Sekiguchi, Dr. Guoqing Wang, Dr. Jinjian Wei, Dr. Katsuyuki Nambara, Dr. Takashi Nishio, Mr. Naoki Iyo, Mr. Tatsuya Matsunaga, Mr. Naotoshi Sugimura, Mr. Yasunobu Suzuki, Mr. Kenta Horie, Mr. Taiyu Tazaki, Mr. Satoshi Nakamura, Mr. Satoshi Emoto, Mr. Shigeaki Suzuki, Mr. Yu Torii, Ms. Mizuki Nihei, Mr. Satoru Hamajima, Mr. Daichi Kato, Mr. Tatsuya Kato, Mr. Tsutomu Kiyosawa, Mr. Yu Sekizawa, Mr. Yier Shi, Mr. Xiong Kun, Dr. Kenya Kobayashi, Dr. Naoki Fujitani, Ms. Chie Takeuchi, Ms. Aki Okuhara, Ms. Yasuyo Kanaya, Ms. Motoko Oomori, Ms. Shuko Takahara, and Ms. Ayane Yamamoto for their hospital support during my laboratory life in Molecular Device Laboratory.

I would like to express the deepest appreciation to Prof. Koichiro Ishimori, Ms. Chiharu Kura, Mr. Ryoto Kojima, Mr. Yosuke Sumiya, Mr. Riku Takahashi, Mr. Yu Toguchi, Mr. Fumihiko Nakamura, Mr. Akio Nitta, Mr. Kei Yanagisawa, and all the other members of Ambitious Leader's Program Fostering Future Leaders to Open New Frontiers in Material Science for their warm encouragement and assistance.

I owe a very important debt to Prof. Yoshinori Nishino, Assistant Prof. Takashi Kimura, Assistant Prof. Akihiro Suzuki, Ms. Ryoko Yamazaki, all the other members in Prof. Nishino's laboratory (Research Institute for Electronic Science, Hokkaido University), Associated Prof. Yasumasa Joti (Japan Synchrotron Radiation Research Institute/SPring-8), and Associated Prof. Yoshitaka Bessho (Institute of Physics, Academia Sinica) for the PCXSS measurement.

This study was supported in part by Research Fellowship of the Japan Society for the Promotion of Science for Young Scientists and The Ministry of Education, Culture, Sports, Science and Technology through Program for Leading Graduate Schools (Hokkaido University "Ambitious Leader's Program").

Finally, I would like to express my special thanks to my family and friends for their hearty encouragement and assistance.

Ryo Iida